Simulation and Modeling of Microfluidic Systems

Vom Fachbereich für Physik, Elektrotechnik und Informationstechnik

der Universität Bremen

zur Erlangung des akademischen Grades

Doktor-Ingenieur (Dr.-Ing.)

genehmigte Dissertation

Von

M.Sc. Alireza Akbarinia

Referent: Professor Dr.-Ing. Rainer Laur

Korreferent: Prof. Dr. Angelika Bunse-Gerstner

Eingereicht am: 02. Juli 2012

Tag des Promotionskolloquiums: 26. März 2013

This thesis is dedicated to my dearest spouse, Farzaneh, for her love, sacrifice, patience, and to our dear sons Amirhossein and Sam.

This thesis is also dedicated to my parents, Abbas and Toba for their love and unconditional support.

Acknowledgments

I wish to express my sincere gratitude to everyone who has helped me during my PhD program. First and foremost, I would like to express my deepest sense of gratitude to my supervisor Prof. Dr.-Ing Rainer Laur, for giving me the opportunity to pursue my PhD studies at the Institut für Theoretische Elektrotechnik und Mikroelektronik (ITEM), at Universität Bremen, for his continued encouragement , support and guidance throughout this work, and for his help with this manuscript.

Especially, I would like to thank Prof. Dr. Angelika Bunse-Gerstner, for her helpful directions and advisers. Special thanks to Scientific Computing in Engineering group at Zentrum für Technomathematik, for the financial support and weekly scientific discussions.

My work would not have been possible without the excellent support staff and facilities available at the institute. I am grateful to all my colleagues at the institute for making it such a pleasant and interesting place to work in.

I am deeply thankful to my parents, Abbas and Toba for their love and unconditional support.

Finally, my great gratitude goes to my dearest, Farzaneh, for her love, sacrifice, patience and understanding; and to our lovely sons Amirhossein and Sam for their never-ending source of inspiration.

Bremen, July 2012

Alireza Akbarinia

Abstract

In the present dissertation, fluid flow and heat transfer in microfluidic systems is investigated numerically. Fluid flow in most applications of microfluidic systems is in the slip flow regime, which is characterized by the slip flow and the jump temperature at the wall. Flow in microfluidic devices shows significant slip since the characteristic length is in the order of the mean free path of the fluid or gas molecules. The slip velocity and the jump temperature at the wall is the most important feature in the micro- or nano scale that differs from conventional internal flow.

The slip flow and heat transfer in microchannels are simulated. Microfluidic systems are separated into straight and curved microchannels. A good understanding of fluid flow in microfluidic systems can be obtained when the results of straight and curved channels are considered together.

Effects of rarefaction on forced convection heat transfer of laminar, steady and incompressible slip flow in straight and curved microchannels with uniform heat flux are investigated. The slip velocity and the jump temperature boundary conditions at the wall are employed. Effects of centrifugal force in the curved microchannels on the hydraulic and thermal behaviors of fluid flow are studied. The Navier-Stokes and energy equations are discretized using the Finite Volume technique. The calculated results show good agreement with previous numerical data and analytical solutions.

The calculated results show that the entrance length and the curvature effects can be neglected, when the Reynolds number is less than 100. As a result,

microfluidic systems are simulated with considering a very long straight microchannel, which can be modeled as totally fully developed region. The fully developed equations are obtained with considering the Navier-Stokes equations at the fully developed conditions. The analytical solution, which is an eigenvalue problem, is presented. The calculated results for two- and three-dimensional straight microchannels are presented. Flow velocity and temperature fields are calculated with very low computational time.

Employing nanofluids is one of the best and practical methods for increasing heat transfer in microchannels. Thermal and hydraulic behaviors of nanofluid flow in microchannels with consideration of the slip velocity and the jump temperature conditions are investigated. Forced convection nanofluid flow in microchannels is simulated to study effects of rarefaction and Al_2O_3 nanoparticles concentration on the slip flow regimes. The Brownian motions of nanoparticles are considered to determine the thermal conductivity of nanofluid.

Contents

Nomenclature

a	convection-diffusion parameter
C_p	specific heat (kJ kg^{-1} K^{-1})
d	diameter of nanoparticle or water molecular
D_h	hydraulic diameter (m)
f	Fanning friction coefficient, ($=\frac{2\tau_w}{\rho\bar{u}^2}$)
h	heat transfer coefficient ($Wm^{-2}K^{-1}$)
k	thermal conductivity (Wm^{-1} K^{-1})
k_B	Boltzmann constant ($=1.3807\times10^{-23}$ J/k)
Kn	Knudsen number (λ/D_h)
L	length of microchannel (m)
Nu_x	local Nusselt number, ($=\frac{h_x D_h}{k}$)
p	pressure (Pa)
P	non-dimensional pressure
Po	Poiseuille number,($f\,\mathrm{Re}=\frac{2\tau_w D_h}{\mu\bar{u}}$)

Pe Peclet number (=Re Pr)

Pr Prandtl number ($= \frac{\mu C_p}{k}$)

q'' constant heat flux

Re Reynolds number ($= \frac{\rho u_{in} D_h}{\mu}$)

T temperature

T^* non-dimensional temperature ($= \frac{k\,(T - T_{in})}{q''\,D_h}$)

u velocity (m s^{-1})

U non-dimensional velocity

W width of microchannel (m)

x, y coordinates

X, Y non-dimensional coordinates

X^* reciprocal Graetz number ($x/(D_h\,Pe)$)

Greek letters

γ specific heat ratio

θ non-dimensional temperature ($= \frac{T - T_{in}}{T_{wall} - T_{in}}$)

β variable, defined in Eq. (19)

λ mean free path (m)

η variable, defined in Eq. (14)

μ dynamic viscosity (N s m^{-2})

ρ density (kg m^{-3})

σ_T thermal accommodation coefficient

σ_v tangential momentum accommodation coefficient

τ_w shear stress at the wall,($= -\mu \frac{\partial u}{\partial y}|_w$)

ϕ solid volume fraction

Φ independent variable

Subscripts

b balk

en entrance length

f base fluid

fd fully developed

i, j array indices

in inlet condition

nf nanofluid

s solid nanoparticles

wall at the wall

Chapter 1
Introduction

1.1 Background

Microscale cooling devices, such as microchannel heat sinks, have attracted much attention in current and future heat removal applications. Specifically, interest is in coolants flowing through large numbers of parallel, micromachined or etched conduits with the purpose to remove heat from and to generate uniform temperature distributions in micro-electro-mechanical systems, such as integrated circuit boards, laserdiode arrays, high-energy mirrors and other compact products. These products are characterized by high transient thermal loads where energy conservation, space, weight and cost savings are important considerations.

Compared to macrochannels, implementation of microchannels as heat exchanger devices exhibit several advantages, such as reduced size and weight, extremely high thermal efficiency and low material consumption. Key is their incredible high heat transfer surface-to-volume ratio that leads to high compactness as well as increased effectiveness of heat exchangers. With the advances in micro-manufacturing technologies and striking developments in micro-fluidic devices, microchannel heat exchangers are increasingly being implemented in a wide variety of applications to efficiently increase heat transfer.

Knowledge of hydraulics and thermal behavior of gas or liquid flow in microchannels leads to accurate predictions of heat transfer and pressure drop, which are essential requirements for safe operation and optimal design of micro heat exchanger devices.

Macroscale heat and fluid flow has been extensively investigated numerically and experimentally since the beginning of the 20th century. Empirical correlations for predicting pressure drop and heat transfer coefficient, have been proposed and are widely accepted. Although research of micro- and nanoscale technology has made huge progress in recent years, many issues related to fluid flow and heat transfer characteristics in small geometries remain unsolved and need to be clarified.

Microscale heat and mass transfer prediction currently present major difficulties. These can primarily be attributed to rarefaction effects that occur in fluids when the channel dimensions become comparable to the mean free path of the fluid molecules. These circumstances are associated with some degree of non-continuum effect. This is characterized by the Knudsen number Kn, which is defined as the ratio of the mean-free path to the appropriate macroscopic flow scale. The rarefaction effects influence velocity, pressure drop and heat transfer in the channels extremely. However, the rarefaction effects can be considered to improve the prediction of both gas and liquid flow and heat transfer in micro- and nano-devices.

1.2 Contribution of the Thesis

Microchannels have higher contact area and higher heat transfer coefficient in comparison with normal cooling circuits. Therefore, using microchannels for cooling of electronic and high power computer chip have great advantages. This research investigates slip flow and heat transfer in micro- and nano-channels for large systems. Whereas gas flow in microchannels is the primary focus of this investigation, liquid flow in slip flow and non-slip flow regimes is studied.

Microfluidic systems are separated into straight and curved parts, which are investigated in two- and three dimensions. Combined results of the straight and

curved microchannels simulations are interpreted for the entire microfluidic system.

Navier-Stokes and energy equations are solved numerically by employing slip velocity and jump temperature at the wall boundaries as the rarefaction effects. The sets of coupled non-linear differential equations are discretized using the Finite Volume Method. The slip velocity and the jump temperature boundary conditions are discretized and employed in the discretization equations. Several codes are developed by MATLAB programming to simulate slip flow in different geometries. Straight and curved rectangular microchannel geometries are considered as typical parts of microfluidic systems. The hydraulic and thermal behavior of fluid flow in slip and non-slip flow regimes are presented and discussed. A wide range of fluid flow and heat transfer characteristic parameters such as the Knudsen number (Kn), the Reynolds number (Re), the Prandtl number (Pr) and the Peclet number (Pe) are studied.

The fully developed slip flow equations for velocity and temperature in rectangular microchannel are solved for obtaining the fluid flow fields with a low computational time. Finally, heat transfer enhancement of the Al_2O_3-water nanofluid flow implementation in microchannels with considering the rarefaction effect has been investigated.

1.3 Research Methodology

Investigation of microfluidic systems with low computational time in order to obtain velocity and temperature fields is the objective of this research. Large microfluidic system are separated into straight and curved microchannels in order to investigate the entire system. Two- and three-dimensions Navier-Stokes equations with slip flow and jump temperature boundary conditions are considered to simulate gas and liquid flow and heat transfer in microchannels. The calculated results of the simulations are presented and interpreted for the entire system.

Furthermore, the analytical solutions of fully developed slip flow are considered in order to calculate the velocity and temperature profiles with low

computation time. The three dimensions analytical solution is an eigenvalue problem, which is solved with the integral transfer method.

Finally, in order to enhance the heat transfer in microchannels, the nanofluids flow application in microchannels is investigated and discussed.

1.4 Outline of the Thesis

The present chapter describes research background and research methods used and outlines the objectives of the research. In Chapter 2 a literature review on fluid flow and heat transfer in microchannels, especially on single phase slip flow regimes, is presented. The theoretical background of fluid flow in microchannels, slip flow and finite volume technique are discussed in Chapter 3.

Fluid flow and heat transfer in straight rectangular microchannels are presented in Chapter 4. It is shown that effects of entrance in microchannels are not significant, therefore these effects can be neglected. As a results, fluid flow in straight microchannels can be assumed to be a fully developed flow.

The curvature effect in the curved rectangular microchannels is investigated in Chapter 5. The results show that if the Reynolds number is small, the centrifugal force does not have any significant effect on the fluid flow and heat transfer in curved microchannels. Therefore, the curved microchannels can be simulated as straight microchannels.

In Chapter 6, the governing equations for fully developed slip flow are obtained. An analytical solution is presented. The solution in three dimensions is an eigenvalue problem, which is solved with the integral transfer technique.

Heat transfer enhancement of nanofluids flow in microchannels is studied and discussed in Chapter 7. Application of nanofluids in microchannels increases heat transfer but does not have any effect on the friction factor.

Finally, in the conclusion, key findings as well as suggestions for further work are presented.

Chapter 2

Literature Review

With the development of science and technology, it is realized that with decreasing size the system will possess many advantages that do not appear in conventional size, like compact size, disposability, and increased functionality [GAD99]. Microchannels are the basic structures in these systems. In the last two decades, a lot of efforts have been undertaken to study the single phase flow and heat transfer in microchannels. These studies have been summarized in review papers by Ho and Tai [HO98], Morini [MOR04], Stone [STO04], Squires and Quake [SQU05], Steinke and Kandlikar [STE06], Renksizbulut et al. [REN06], Hu and Li [HU07], Kraly et al. [KRA09], Rosa et al. [ROS09], Shao et al. [SHA09]. Morini [MOR04] summarized and analyzed experimental work on the convective heat transfer through microchannels. Rosa et al. [ROS09] reviewed and explained the numerical and experimental works on the single phase heat transfer in microchannels with emphasis on the scaling effects. They concluded that the classical theories of fluid flow and heat transfer are reliable, but the scaling effects must be accounted for. They classified suitable expressions for calculating fluid flow and heat transfer in microchannels with different conditions.

Fluid flow in microchannels is usually expected to be in the laminar regime; hence the Reynolds number is directly proportional to the diameter. According to classical macroscale theory, the Nusselt number is constant for laminar flow.

Therefore the heat transfer coefficient is inversely proportional to the diameter, suggesting high potential for microchannel heat sinks.

In the early 1980s, the first experimental investigations of flow through microchannels were motivated by the interest in high-performance heat transfer devices, in particular for cooling of electronics. Tuckerman and Pease [TUC81] showed that the laminar flow in a rectangular microchannel has higher heat extraction capabilities than turbulent flow in conventional size tubes. This finding opened up a new research field and it has been followed by many more studies by numerous researchers. A lot of studies have been done experimentally to investigate fluid flow and heat transfer in microchannels such as Harms et al. [HAR99], Mala and Li [MAL99], Xu et al. [XU00], Judy et al. [JUD02], Holden et al. [HOL03], Wu and Cheng [WU03], Li and Olsen [LI06], Hrnjak and Tu [HRN07], Silva et al. [SIL08], Wang and Wang [WAN09], El-Genk and Yang [ELG09].

Holden et al. [HOL03] designed and characterized a laminar microfluidic diffusion diluter (μDD) for the combinatorial study of concentration dependent phenomena. They proposed a non-dimensional parameter K, which describe this process and allows the efficient prediction of concentration values in the μDD.

Li and Olsen [LI06], Silva et al. [SIL08] and Wang & Wang [WAN09] implemented microfluidic particle image velocimetry (μPIV) to measure the fluid flow in microchannels. Silva et al. [SIL08] confirmed the influence of the surface roughness on the laminar microscopic liquid flow behavior with micro-PIV measurement and numerical analysis.

Wu and Cheng [WU03] and Xu et al. [XU00] investigated the friction factor of a liquid laminar flow in microchannels with different experimental methods. They confirmed that characteristics of flow in microchannels agree with convectional behavior predicted by the Navier-Stokes equations and these equations are still valid for the laminar flow in microchannels.

Based on the Knudsen number Kn (see appendix A for details) , the flow in microchannels has been classified into four flow regimes: continuum flow regime ($Kn \leq 0.001$), slip flow regime ($0.001 < Kn \leq 0.1$), transition flow regime ($0.1 < Kn \leq 10$) and free molecular flow regime ($Kn > 10$).

The slip velocity at the fluid-wall interface appears in both gas and liquid flows. These phenomena is more important in micro and nano-scales. In micro-scales and nano-scales the hydraulic diameter is smaller than the molecular mean free path. Therefore, the assumption of non-slip velocity is not valid. It is confirmed by the work of several researcher. They measured the slip velocity just above the solid surface ([TRE02], [NGO07] and [YAN03]). They found that the slip velocity cannot be neglected in the case of fluid flow and gas flow in microchannels.

Rarefied gas flow and heat transfer in the entrance region of rectangular microchannels in the slip flow regime has been investigated numerically by numerous authors, such as Beskok et al. [BES96], Yu and Ameel [YU01], Choi et al. [CHO03], Zhu and Liao [ZHU06], Renksizbulut et al. [REN06], Dongari et al. [DON07], Niazmand et al. [NIA08], Renksizbulut et al. [REN06], Lee and Garimella [LEE06], Niazmand et al. [NIA08] and Khadem et al. [KHA09].

Choi et al. [CHO03] applied a new slip model, the Langmuir slip condition, to a proposed numerical method for predicting gaseous compressible slip flow and compared it with the Maxwell slip condition. Renksizbulut et al. [REN06] solved slip flow and heat transfer in the entrance region of rectangular microchannels for cases in which the Prandtl number is equal to unity. Lee and Garimella [GAR06] investigated laminar convective heat transfer in the entrance region of rectangular micro channels with two different boundary conditions and proposed a generalized correlation for both the local and average Nusselt number in the thermal entrance region.

Khadem et al. [KHA09] studied slip flow and heat transfer characteristics in microchannels with considering the wall roughness. Dongari et al. [DON07] solved the Navier-Stokes equations for gaseous slip flow in long microchannels with a second-order accurate slip boundary condition at the wall. They derived an exact expression for pressure and velocity for slip flow regime. Biswal et al. [BIS07] simulated two dimensional free convective gas flows in symmetrically heated vertical microchannels with temperature dependent thermo-physical properties and they compared the results with macro-scale flow results.

The gas flow heat transfer in circular microtubes was investigated by Barron et al. [BAR97] and Avci and Aydin [AVC08] and they proposed some

expressions for the Nusselt number. Barkhordari and Etemad [BAR07] simulated flow and thermal fields of non-Newtonian fluids in circular microchannels. Al-Bakhit and Fakheri [ALB06] studied parallel flow heat exchangers numerically and investigated the effects of the wall conduction for microchannel heat exchangers. Duan and Muzychka [DUA07] investigated slip fluid flow in elliptic microchannels. They developed a model for Poiseuille number prediction.

Larrodé et al. [LAR00] and Sun et al. [SUN07] found that the temperature jump effects are very important and should be included in the modeling of the slip flow heat transfer problems. Neglecting these effects leads to a significant overestimation of the heat transfer coefficient. By applying the orthonormal function analysis, Zho and Liao [ZHO06] obtained a theoretical predicting for heat transfer behavior of the fully developed incompressible laminar flow in a microchannel with arbitrary cross section in the slip flow and temperature jump regime.

Numerically liquid slip flow and heat transfer in microchannels has also been studied, for example by Fedorov and Viskanta [FED00], Yu and Ameel [YU01], Senn and Poulikakos [SEN04], Alfadhel and Kothare [ALF05], Ngoma and Erchiqui [NGO07], Husain and Kim [HUS08], Xiao et al. [XIA09]. Yu and Ameel [YU01] investigated forced convection laminar slip flow under thermally developing flow for constant wall temperature and isoflux boundary conditions. Hettiarachchi et al. [HET08] investigated three-dimensional slip-flow and heat transfer in rectangular microchannels with velocity slip and temperature jumps. They proposed a correlation for the fully developed friction factor in different aspect ratio.

A vast body of literature exists on forced convection gas and liquid flows in micro-systems but most of them have employed non-slip flow regime at very low Re and Pe number ($Re<10$). The present work investigates slip velocity and jump temperature as the effects of rarefaction on the hydrodynamic and the thermal parameters of a laminar forced convection fluid flow in rectangular microchannels. A wide range of the Peclet number ($1<Pe<700$), the Reynolds number ($0.01<Re<1000$) and the Knudsen number ($0<Kn<0.1$) is considered. Heat transfer enhancement due to nanofluid implementation in the cooling

application of microchannels is studied. Simultaneous effects of the slip velocity and the jump temperature on the velocity, the developing of temperature, the balk temperature, the Poiseuille number and the Nusselt number are presented and discussed.

Chapter 3

Theoretical Background

In fact fluid flow in most applications of microfluidic systems, such as Micro Gyroscope, Accelerometer, Flow Sensors, Micro Nozzles, Micro Valves, is in slip flow regime, which is characterized by slip flow at the wall. Traditionally, the no-slip flow and an analogous no-temperature-jump conditions are applied for simulation fluid flow and heat transfer. Strictly speaking, no-slip/no-jump boundary conditions are valid only if fluid flow adjacent to the surface is in thermodynamic equilibrium. This requires an infinitely high frequency of collisions between the fluid and the solid surface ([GAD99], [BES94]). Flow in devices shows significant slip since characteristic length is on the order of the mean free path of the fluid or gas molecules. It means that the collision frequency is simply not high enough to ensure equilibrium and a certain degree of tangential velocity slip and temperature jump must be appeared.

The slip velocity at the wall is the most important feature in micro- or nano scale that differs from conventional internal flow. Therefore, the slip flow characteristics are very important for designing and optimizing the micro or nano systems.

Furthermore, the optimization of microchannels design is affected significantly by their reliability and thermal performance. Researchers have confirmed that the temperature jump has significant effects. It should be included in the modeling of the slip flow heat transfer problems.

Neglecting the effects of the slip velocity and the jump temperature leads to a significant overestimate of friction factor and heat transfer coefficient ([LAR00], [SUN07]). The modeling and physics of gas and liquid flows in micro systems, as well as simulation methods are explained and discussed in this chapter.

3.1 Fluid Modeling in Microfluidic systems

Fluid flows in microscale vary from those in macroscale. The conventional flow models such as the Navier–Stokes equations with non-slip boundary condition at a fluid–solid interface which apply routinely and successfully for larger flow devices, cannot always predict well the thermal and hydraulic behaviors of the operation of MEMS-based ducts, nozzles, valves, bearings, turbomachines, etc.

Examinations of fluid flow through microfluidic systems result in the questions which model to be used and which boundary conditions to be applied. Thermofluids researchers are accustomed to work with the Navier–Stokes equations together with the corresponding PDEs (partial differential equations) for energy (frequently) and mass transfer (more occasionally). In fact, there is a range of theoretical models available and the relationships between them are depicted in Fig. 3.1. Depending on the fluid flow, there are two main modeling approaches, which are called molecular and continuum model, respectively. The first model consists of deterministic and statistical methods (Molecular Dynamic MD, Direct Simulation Monte Carlo DSMC and Boltzmann). In the second model velocity, density, pressure, etc. are defined at every point in space and time, and conservation of mass, energy, and momentum lead to a set of nonlinear partial differential equations (Euler, Navier–Stokes, Burnett, etc.) ([GAD06]).

The continuum models are easier to handle mathematically than the molecular models. Therefore, the continuum models can be applied to numerous flow situations. It considers the fluid as a continuous medium describable in terms of the spatial and temporal variations of density, velocity, pressure, temperature, and other macroscopic flow quantities, which are more familiar to fluid dynamics.

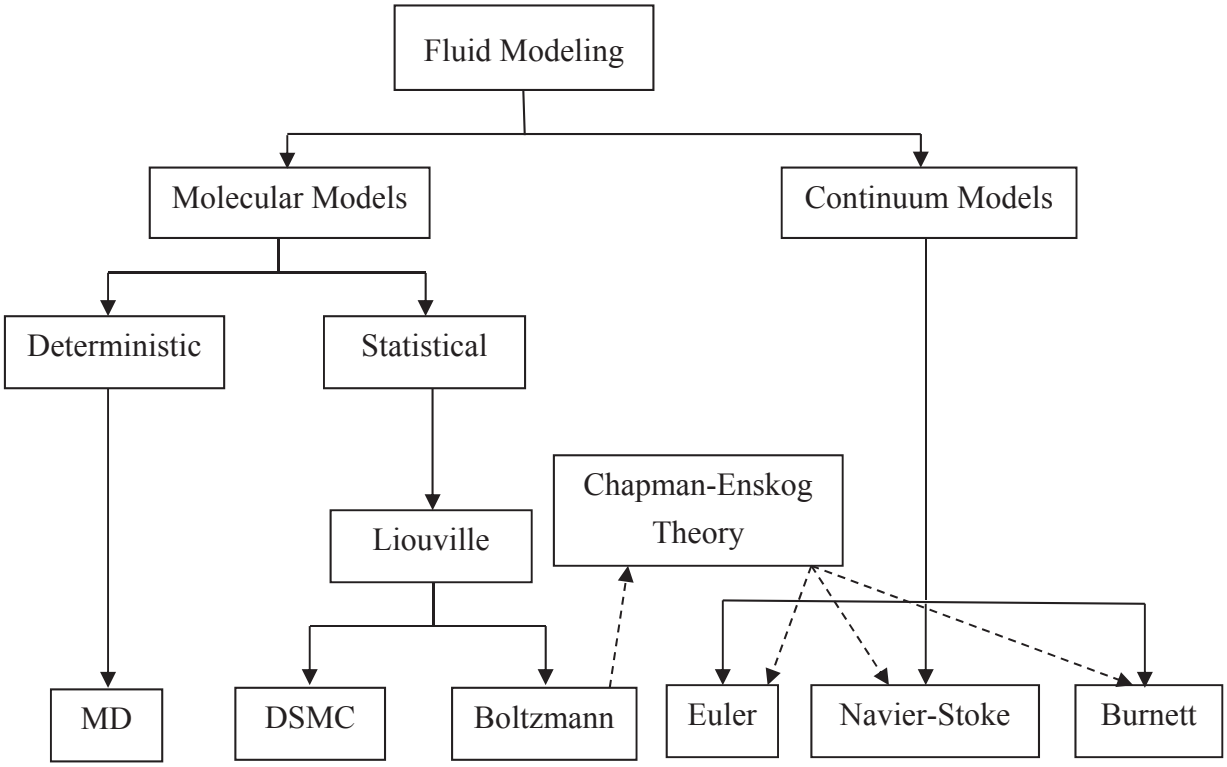

Fig. 3.1 Overall relationship of models in fluid mechanics (([ROS09])

Basically, the continuum model leads to fairly accurate predictions as long the flow is not too far from thermodynamic equilibrium. In the present research, because of the above advantages of the continuum approaches, the Navier-Stokes equations have been elected to apply for the simulation of microfluidic systems.

3.2 Flow Classification

The pioneering experiments in rarefied gas dynamics were conducted by Knudsen in 1909. The Knudsen number ($Kn = \frac{\lambda}{D_h}$) is defined as the ratio between the mean free path and the characteristic length.

Table 3.1 Recommendation models for Kn ranges ([ROS09])

Kn range	Range description	Recommended models
Kn→0	Neglect of diffusion	Euler equations
$Kn \leq 10^{-3}$	Continuum (no slip)	Navier-Stokes equations with non-slip boundary condition
$10^{-3} \leq Kn \leq 10^{-1}$	Continuum with slip flow	Navier-Stokes equations with slip boundary condition Burnett equations
$10^{-1} \leq Kn \leq 10$	Transition to molecular flow	Direct Simulation Monte Carlo
Kn>10	Free-molecular flow	Lattice Boltzmann
Kn very large	Extreme range	Molecular Dynamics

In this study, the hydraulic diameter D_h is considered as the characteristic length. The mean free path λ is the average distance moved by molecules between collisions. The continuum Navier–Stokes model is valid for gas or liquid flow simulation when λ is much smaller than the hydraulic diameter. The non-slip velocity condition and the non-jump temperature condition at a solid–fluid interface are no longer accurate and valid, when λ is not much smaller than D_h.

As presented in Table 3.1, fluid flow in microchannels has been classified into six flow regimes, based on the Knudsen number (Kn): Neglect of diffusion (Kn→0), continuum flow regime (Kn ≤0.001), slip flow regime (0.001 < Kn ≤0.1), transition flow regime (0.1 < Kn ≤ 10), free molecular flow regime (Kn>10) and extreme range (Kn very large) [ROS09]. In practice, the non-slip velocity and non-jump temperature conditions lead to fairly accurate predictions as long as $Kn < 0.001$. Beyond that, the collision frequency is simply not high enough to ensure equilibrium and a certain degree of tangential velocity slip and temperature jump must be applied. On the other hand, the traditional continuum approach is valid, albeit with modified boundary conditions, as long as $Kn < 0.1$. As Kn increases, rarefaction effects become more significant, and eventually the continuum approach breaks down.

3.3 Governing Equations

It has been well established that the Navier-Stokes equations with the slip velocity and the jump temperature boundary conditions can be applied for the modeling and simulation of the fluid flow in the microfluidic systems. The Navier-Stokes equations with the slip velocity and the jump temperature boundary conditions as rarefaction effects are presented in this section.

3.3.1 Navier–Stokes Equations

The Navier–Stokes equations describe the exchange (flux) of mass, momentum and energy through the boundary of a control volume. The three–dimensional Navier–Stokes equations for a Newtonian flow can be expressed in the vector form as:

$$\frac{\partial \rho \vec{u}}{\partial t} + \left(\rho \vec{u} \cdot \nabla\right) \vec{u} = -\nabla p + \nabla\left(\mu \nabla \vec{u}\right) + \vec{F}. \tag{3.1}$$

Each component of the Navier-Stokes can be explained as follows:

$$\overbrace{\underbrace{\frac{\partial \rho \vec{u}}{\partial t}}_{\substack{unsteady\\acceleration}} + \underbrace{\left(\rho \vec{u} \cdot \nabla\right) \vec{u}}_{\substack{convection\\acceleration}}}^{Inertia\ (per\ volume)} = \overbrace{\underbrace{-\nabla p}_{\substack{pressure\\gradient}} + \underbrace{\nabla\left(\mu \nabla \vec{u}\right)}_{\substack{diffusion\\term}}}^{Divergence\ of\ stress} + \underbrace{\vec{F}}_{body\ forces}, \tag{3.2}$$

where the first and second term at the left side are the unsteady and convection terms, respectively. The first and second term at the right side are the pressure gradient and diffusion terms, respectively, while F represents the body forces (forces per unit volume), such as the gravity or the centrifugal force.

The Navier–Stokes equations are strictly a statement of the conservation of momentum. Depending on assumptions made, more information is needed to describe completely the flow. This may include boundary data (non-slip, capillary surface, etc.), the conservation of mass, the conservation of energy, and/or an equation of state. Regardless of the flow assumptions, a statement of the conservation of mass is generally necessary. The mass continuity equation is given in its most general form as:

$$\frac{\partial \rho}{\partial t} + \nabla \cdot \rho \vec{u} = 0 \tag{3.3}$$

and the fluid energy equation can be expressed as:

$$\frac{\partial \rho T}{\partial t} + \left(\rho C_p \vec{u} \cdot \nabla\right) T = \nabla\left(k \nabla T\right), \tag{3.4}$$

where the first and second term at the left side are the unsteady and convection terms, respectively, whereas the term at the right is the diffusion term.

3.3.2 Rarefaction implementation

Surface effects are known to have important and dominating roles in small devices. The continuum approximation may be invalidated in the microscale. For a pipe with a characteristic length of 1m, the surface to volume ratio is $1m^{-1}$, while that for a microchannel, having a size of 1μm, is 10^6 m^{-1}. The million fold increase in surface area relative to the mass of the minute device substantially affects the transport of mass, momentum, and energy through the surface.

The slip velocity at the fluid-wall interface exists in the gas and liquid flows. This effect is more significant in the micro- and nano-scales, because in the macro-scale the hydraulic diameter is very large compared to the molecular mean free path (Kn≈0) and the assumption of non-slip velocity (i.e. slip velocity is zero at the fluid-wall interface) is valid. In cases of the micro and nano-scales, this assumption is no longer correct for both liquid and gas flows. This fact for the liquid flow is confirmed by the Tretheway and Meinhar [TRE02] investigation which measured experimentally the velocity profiles of the water flowing through 30×300 μm channels. They found that when a hydrophobic microchannel (uncoated glass) surface is coated with a 2.3 nm thick monolayer of hydrophobic octadecyltrichlorosilane, an apparent velocity slip is measured just above the solid surface. This velocity is approximately 10 % of the free stream velocity and yield slip length of approximately 1 μm. For this slip length, slip flow is negligible for length scales greater than 1mm but must be considered at the micro- and nano-scales. The results of Ngoma and Erchiqui [NGO07], Yang and Kwok [YAN03] and Barrat and Bocquet [BAR99] also confirm the use of the slip velocity for the liquid flows in the micro and nano-scales.

In the present work the range of the Knudsen number is selected between 0 to 0.1 to consider slip velocity at the nano-scales (Kn≈0.1) as well as micro-scales (0<Kn <0.1) and non-slip velocity at macro-scale (Kn≈0) in the liquid flows.

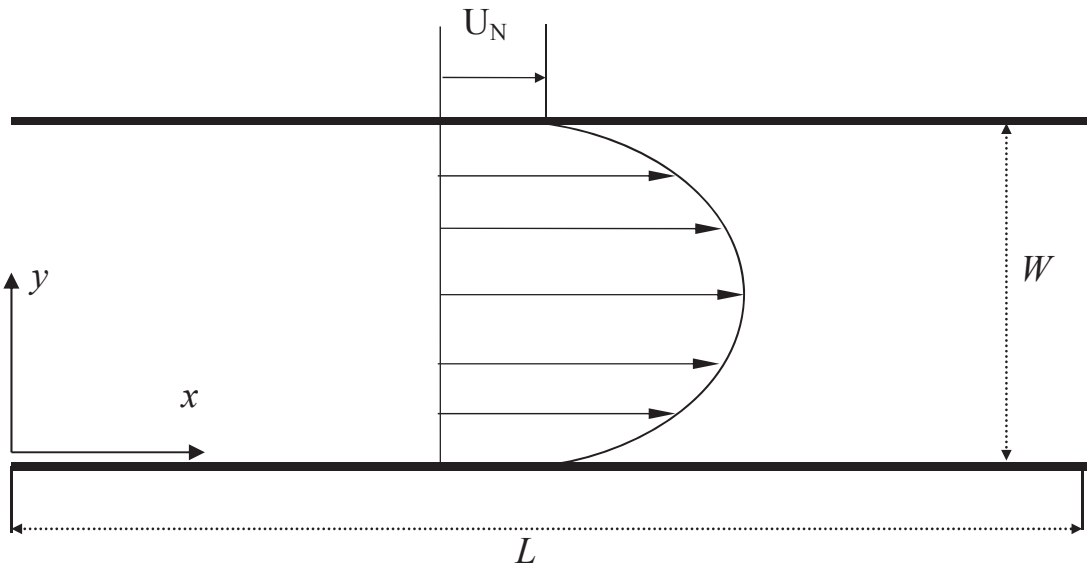

Fig. 3.2 Schematic of microchannel flow.

The second order non-dimensionalized velocity slip condition is expressed as [GAD06]:

$$U_N = \left(\frac{2-\sigma_V}{\sigma_V}\right) Kn \left.\frac{\partial U}{\partial Y}\right|_{wall} + \frac{3}{2\pi}\frac{(\gamma-1)}{\gamma}\frac{Kn^2 \operatorname{Re}}{Ec}\left.\frac{\partial \theta}{\partial X}\right|_{wall}, \tag{3.5}$$

here Ec is the Eckert number ($Ec = \frac{U^2}{C_p \Delta T}$). U_N is the axial velocity of the fluid flow near to the wall. The second term can be neglected if $\frac{\partial}{\partial Y} >> \frac{\partial}{\partial X}$ at the wall and also due to the fact that it is the second order in the Knudsen number. Similar arguments can be applied to the jump temperature boundary condition. The resulting from the Taylor series leads in dimensionless form as follows [GAD06]:

$$\theta_N - \theta_{wall} = \left(\frac{2-\sigma_T}{\sigma_T}\right)\left(\frac{2\gamma}{\gamma+1}\right)\frac{1}{\Pr}\left[Kn\left(\left.\frac{\partial \theta}{\partial Y}\right|_{wall}\right) + \frac{Kn^2}{2!}\left(\left.\frac{\partial^2 \theta}{\partial Y^2}\right|_{wall}\right) + \ldots\right], \tag{3.6}$$

where θ_N is the temperature of fluid near to the wall. The thermal and momentum accommodation coefficients (σ_V, σ_T) are near unity for most

engineering applications and they are taken as unity in the present study (see Appendix B for details about the thermal and momentum accommodation coefficients).

After simplifying, the non-dimensional forms of the slip velocity and jump temperature boundary conditions at the wall with respect to the used notation in Fig. 3.2 are given by:

$$U_N - U_{wall} = Kn \left.\frac{\partial U}{\partial Y}\right|_{wall}, \tag{3.7}$$

$$\theta_N - \theta_{wall} = \frac{Kn}{\beta} \left.\frac{\partial \theta}{\partial Y}\right|_{wall}, \tag{3.8}$$

where

$$\beta = \Pr\left(\frac{\gamma+1}{2\gamma}\right), \qquad \theta_{wall}=1 \text{ and } U_{wall}=0. \tag{3.9}$$

3.4 Numerical methodology

Computational fluid dynamics or CFD is employed in a wide variety of applications including fluid flow and heat transfer. Computational Fluid Dynamics is the study of fluid mechanics and heat transfer by means of numerical methods. It is attractive to industry since it is usually more cost-effective than physical testing. However, one must note that complex flow simulations are challenging and error-prone, therefore it takes a lot of engineering expertise to obtain valid solutions ([RED01]).

As mentioned above, fluid flow and heat transfer phenomena inside the microfluidic systems can be described by the set of governing equations: the continuity, the momentum (Navier-Stokes) and the fluid energy conservation equations with employing the slip velocity and jump temperature boundary

conditions at the wall. The solution, which is found by using CFD techniques, allows one to obtain a numerical description of the complete flow field of interest. The partial differential equations (PDEs) are converted into the algebraic form on a mesh, which defines the geometry and flow domain of the interest. Appropriate boundary and initial conditions are applied to the mesh. Distributions of quantities such as velocity, pressure, turbulence, temperature and concentration are determined iteratively at every point in space and time within the domain [PAT80]. This section focuses on the general description of Computational Fluid Dynamics which is used in this investigation.

The standard procedure for a CFD study consists of three main parts: preprocessing, solution and post-processing. During the pre-processing procedure the domain is created and the geometry is divided into sub-regions which are then meshed to create the control volumes. Each control volume is defined by its surfaces. The grid, which contains information about the geometry, is used in the solver part.

The governing equations can be discretized with three distinct streams of numerical solution techniques: Finite Difference, Finite Element and Finite Volume methods, which are explained briefly in the following sub-section. The solver part involves the discretized algebraic equations with employing the mesh and boundary information. The simulation is then started until a converged solution is reached. The obtained results can be visualized with a post-processing part. Contour and vector plots, as well as animations of the calculated quantities can be created.

3.4.1 Discretization methods

As already mentioned the domain needs to be divided into cells and nodes. After the grid is generated the governing differential equations must be discretized, or in other words replaced in CFD code with a set of algebraic equations. Finite Difference, Finite Element and Finite Volume methods are three well established methods of discretization. The following is a summary of the basic steps performed by the solver part:

- Formal integration of the governing equations of fluid flow over all the control volumes of the solution domain
- Approximation of the unknown flow variables by means of simple functions
- Discretization by substitution of the approximations into governing flow
- Solution of algebraic equations using an iterative method.

The main differences between the three separate methods are associated with the way in which the flow variables are approximated and with the discretization processes.

3.4.1.1 Finite Difference Method

The Finite Difference method (FDM) is the simplest and most efficient method for solving partial differential equations in problem regions with simple boundaries. At each grid point the derivative of a scalar function is substituted with a finite difference approximation. By substituting the difference formula into the PDE, a difference equation is obtained. Despite the fact that the Finite Difference method is the simplest method for discretization, it requires a structured grid. Therefore this method is difficult to apply to complex geometries and is more suitable for simple cases.

3.4.1.1 Finite Element Method

The Finite Element method (FEM) is used for finding approximate solutions to partial differential equations as well as to integral equations [STR73]. In the Finite Element method the domain is subdivided into elements. Each of these elements or cells has nodes at its vertices. The solution approach is based either on eliminating the differential equation completely (steady state problems), or rendering the PDE into an equivalent ordinary differential equation, which is then solved using standard techniques such as Finite Differences, etc. There are many ways of doing this, all with advantages and disadvantages. The Finite Element method is not widely used in CFD because of the higher computational effort required when compared to Finite Volume methods.

3.4.1.1 Finite Volume Method

The Finite Volume method is a special Finite Difference formulation which is employed in the most well established CFD codes. The Finite Volume method is a method for discretization and representing partial differential equations as algebraic equations. Similar to the Finite Difference method, values are calculated at discrete places on a meshed geometry. "Finite Volume" refers to the small volume surrounding each node point on a mesh. In the Finite Volume method, volume integrals in a partial differential equation that contain a divergence term are converted into surface integrals, using the divergence theorem. These terms are then evaluated as fluxes at the surfaces of each finite volume. Because the flux entering a given volume is identical to that leaving the adjacent volume, these methods are conservative. Advantage of the Finite Volume method is that it is easily formulated to allow for unstructured meshes.

The conservation of a general flow variable Φ , for example a velocity component or temperature, within a finite control volume can be expressed as a balance between the various processes tending to increase or decrease it as follows:

$$\begin{bmatrix} Rate\,of\ \Phi\ changes \\ in\ a\ control\ volume \\ with\ respect\ to\ time \end{bmatrix} = \begin{bmatrix} Net\ flux\ of\ \Phi\ du\ to \\ convection\ through \\ the\ control\ volume \end{bmatrix} + \begin{bmatrix} Net\ flux\ of\ \Phi\ du\ to \\ diffusion\ through \\ the\ control\ volume \end{bmatrix} + \begin{bmatrix} Net\,rate\ of\ \Phi \\ generation\ inside \\ the\ control\ volume \end{bmatrix}$$

CFD codes contain discretization techniques suitable for the treatment of the key transport phenomena, convection (transport due to fluid flow) and diffusion (associated with the creation or destruction of Φ) and the rate of change with respect to time. The underlying physical phenomena are complex and non-linear so an iterative solution approach is required [PAT80].

3.4.2 Velocity –Pressure Coupling Algorithms

In the numerical solution of fluid flow and heat transfer problems, the “pressure-correction approach” is the most popular method used in CFD. The first pressure-correction algorithm was the SIMPLE proposed by Patankar and

Spalding [PAT72]. The acronym SIMPLE stands for semi-implicit method for the pressure-linked equation.

The SIMPLER algorithm successfully overcomes the first approximation, and is widely employed in the current CFD community [PAT80]. Although there are more than ten variants of the SIMPLE-like algorithm, many attempts have been made to resolve their problem. In 1984, van Doormaal and Raithby [VAN84] changed the definition of the velocity correction equation coefficients to propose the SIMPLEC algorithm. In the algorithm SIMPLEX ([VAN85]; [RAI88]), by solving a set of algebraic equation for the coefficients in the velocity correction equations, the effects of dropping the neighboring grids are also taken into account.

In 1985, the PISO method is proposed by Issa [ISS85] to implement two or more correction steps of pressure correction. The revised method was called MSIMPLER. All the above-mentioned algorithms and some others not mentioned above, for example, SIMPLESSEC, SIMPLESSE of Gjesdal and Lossius [GJE97], and the method proposed in Wen and Ingham [WEN93] are usually called SIMPLE-like or SIMPLE-family algorithm.

The SIMPLER algorithm, which is employed in this thesis to create the author designed CFD code to solve the problem, is explained as follows [PAT80]:

Equation (3.1) after discretizing by the finite volume method on a staggered grid system (Fig. 3.3), could be given as:

$$a_P \Phi_P = \sum a_{nb} \Phi_{nb} + b, \tag{3.10}$$

where Φ is the general valuable standing for u and v, the subscripts P and nb refer to the gird point P and its neighboring grids, respectively. a_p is the coefficient for the main grid point, a_{nb}'s are the coefficients of neighboring grid points and b is the source term.

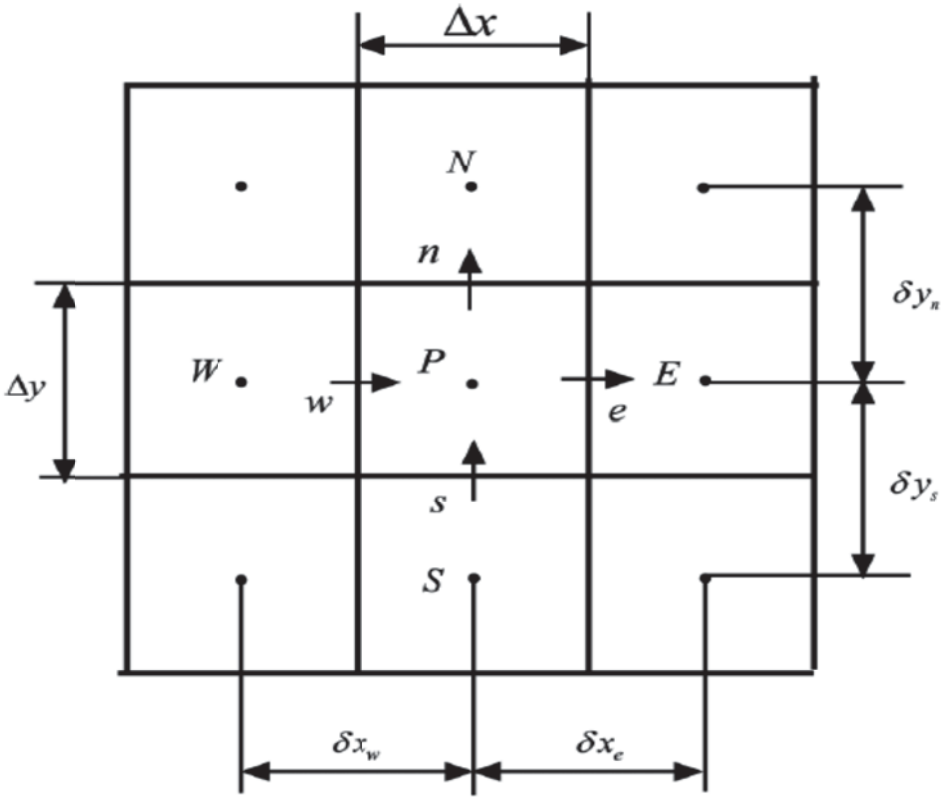

Fig. 3.3 staggered grid system.

After separating the pressure gradient term from the b-term and replacing the general valuable by u or v and according to the notation used in Fig. 3.3, we have:

$$a_e u_e = \sum a_{nb} u_{nb} + (p_P - p_E) A_e + b, \tag{3.11}$$

$$a_n v_n = \sum a_{nb} v_{nb} + (p_P - p_N) A_n + b. \tag{3.12}$$

The discretized pressure equation can be concluded from the momentum equations and the continuity equation as follows:

$$a_P p_P = \sum a_{nb} p_{nb} + b_P. \tag{3.13}$$

By solving equations (3.11) and (3.12), we can obtain the intermediate solutions, symbolized by u^* and v^* which need to be improved such that the improved velocities can satisfy the mass conservation condition for each control volume. By introducing a pressure correction term, p', and the corresponding velocity correction terms u' and v', the improved velocities can be expressed by:

$$u = u^* + u', \tag{3.14}$$

$$v = v^* + v'. \tag{3.15}$$

These improved velocities are required to satisfy the continuity condition. The equations for the velocity correction terms, u', v', can be derived by substitution and rearrangement ([PAT80]), and take the following form:

$$a_e\, u'_e = \sum a_{nb}\, u'_{nb} + (p'_P - p'_E)A_e, \tag{3.16}$$

$$a_n\, v'_n = \sum a_{nb}\, v'_{nb} + (p'_P - p'_N)A_n. \tag{3.17}$$

At this point an approximation, i.e. the second approximation in the SIMPLE algorithm, is applied by dropping the terms $\sum a_{nb}\, u'_{nb}$ *and* $\sum a_{nb}\, v'_{nb}$ in the above equations. Then we obtain:

$$u'_e = d_e(p'_P - p'_E), \tag{3.18}$$

$$v'_n = d_n(p'_P - p'_N), \tag{3.19}$$

where d_e, d_n are defined as:

$$d_e = \frac{A_e}{a_e}, \tag{3.20}$$

$$d_n = \frac{A_n}{a_n}. \tag{3.21}$$

Then the improved velocities are rewritten as follows:

$$u_e = u^*_e + d_e\,(p'_P - p'_E), \tag{3.22}$$

$$v_n = v^*_n + d_n\,(p'_P - p'_N). \tag{3.23}$$

Upon substitution of the improved velocities of equations (3.22) and (3.23) into continuity equation, the equation for the pressure correction term is then derived as:

$$a_P\, p'_P = \sum a_{nb}\, p'_{nb} + b_P, \tag{3.24}$$

where

$$b_P = (\rho u^* A)_w - (\rho u^* A)_e + (\rho v^* A)_s - (\rho v^* A)_n. \tag{3.25}$$

In Equation (3.25) the coefficients are the same as those in the Equation (3.13) except the b-term, where the velocities take the values of the previous iteration, rather than the intermediate solutions.

The solution procedure of the SIMPLER algorithm, which is shown as a flow chart in Fig. 3.4, is as follows:

1. guess an initial velocity field u^0, v^0;
2. calculate the coefficients(a_{nb}, a_e, a_n) of the discretized momentum equations and the pseudo-velocities $\hat{u}$ and $\hat{v}$ by following equations:

$$\hat{u}_e = \frac{\sum a_{nb} u_{nb}^0 + b}{a_e}, \tag{3.26}$$

$$\hat{v}_n = \frac{\sum a_{nb} u_{nb}^0 + b}{a_n}. \tag{3.27}$$

3. solve pressure Equation (3.10) to get p^*;
4. solve the discretized momentum equations with p^* to get u^* and v^* (Equation (3.11) and Equation (3.12) with u^* , v^* and p^*)
5. solve the pressure correction equation(3.24) to get p';
6. correct the velocities by Equation (3.14) and Equation (3.15);
7. solve the discretized equations for other scalar variables if necessary; and return to step 2 until convergence condition is satisfied.

It is to be noted that in the SIMPLER algorithm, the pressure correction term is only used to correct the velocities, but not used to correct the pressure. The obtained pressure correction values are appropriate to correct the velocities, but not to pressure values. The discretized equations are solved by iterative methods. The solutions of velocities of the current iteration are based on the coefficients and source term determined by the solutions of the last iteration.

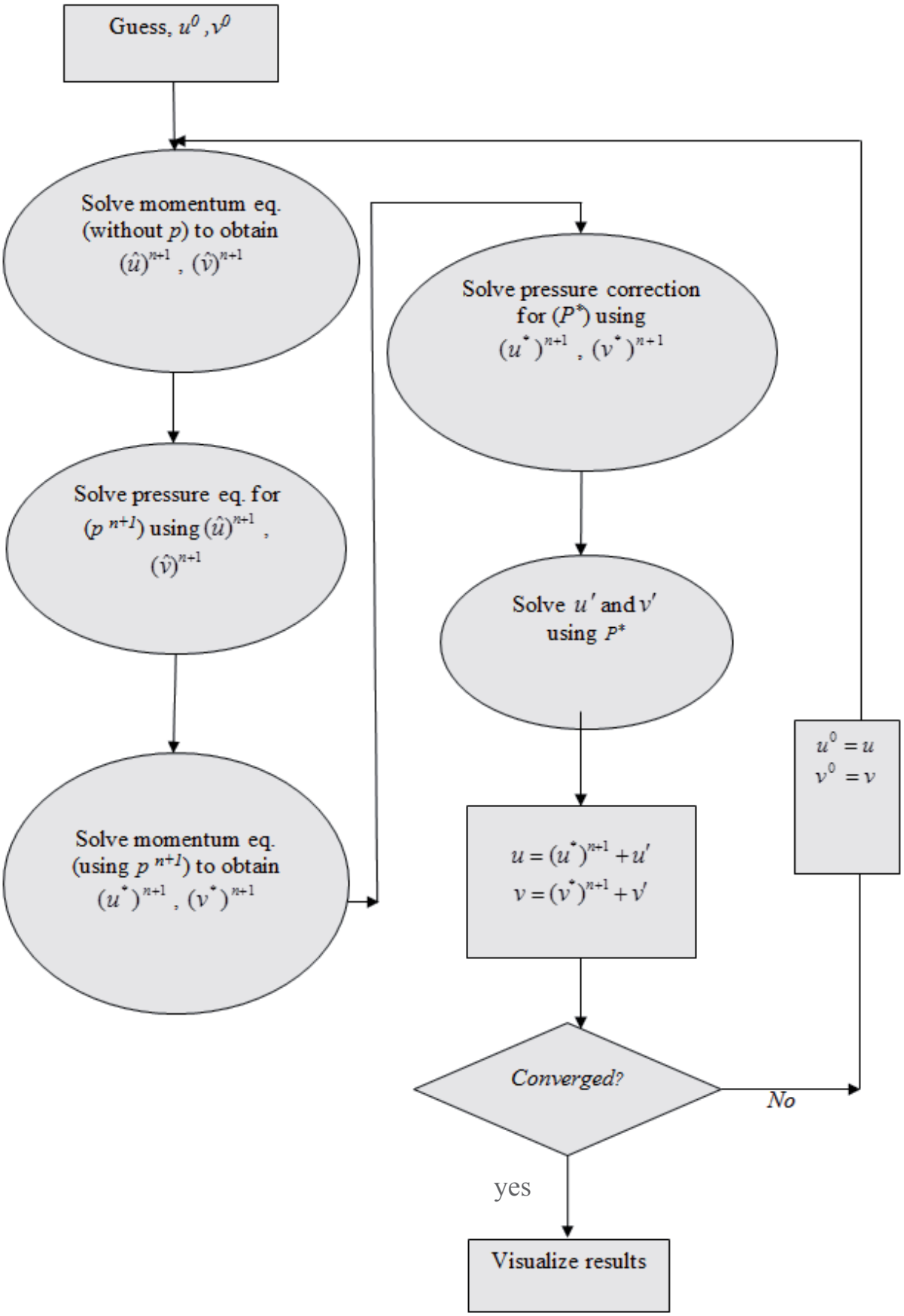

Fig. 3.4 Flow diagram of SIMPLER algorithm.

3.4.3 Approximation Schemes in Finite Volume Method

There are several schemes of approximation in FVM such as Central difference, Upwind, Hybrid and Exponential and Power Law. Since the Power Law scheme has been used in this thesis to discretize the convection and diffusion terms, this section is focused on it. The governing equation for very simple one-dimensional convection and diffusion problem is as follows [PAT80]:

$$\frac{d(\rho u \varphi)}{dx} = \frac{d}{dx}\left(\Gamma \frac{d\varphi}{dx}\right). \tag{3.28}$$

Both density, ρ, and diffusivity, Γ, are assumed to be constants. The continuity equation for this one-dimensional problem is

$$\frac{d(\rho \varphi)}{dx} = 0. \tag{3.29}$$

Equation (3.28) is subject to the following boundary conditions:

- at $x=0$: $\varphi=\varphi_0$
- at $x=L$: $\varphi=\varphi_L$

The governing equation (3.28) and the boundary conditions are made non-dimensional with the following dimensionless variables.

$$\Phi = \frac{\varphi - \varphi_0}{\varphi_L - \varphi_0}, \quad X = \frac{x}{L}. \tag{3.30}$$

Therefore, the non-dimensional governing equation and boundary conditions are given as:

$$\mathrm{Pe}\frac{d\Phi}{dX} = \frac{d^2\Phi}{dX^2}, \tag{3.31}$$

with:

- at $X=0$: $\Phi=0$
- at $X=1$: $\Phi=1$,

where Pe ($\mathrm{Pe} = \frac{\rho u L}{\Gamma}$, see Appendix A) is the Peclet number that reflects the relative level of convection and diffusion. Pe becomes zero for the case of pure diffusion and becomes infinite for the case of pure convection.

The exact solution of (3.31) is obtained as:

$$\Phi = \frac{\varphi - \varphi_0}{\varphi_L - \varphi_0} = \frac{e^{\mathrm{Pe}\,X} - 1}{e^{\mathrm{Pe}} - 1}. \tag{3.32}$$

3.4.3.1 Power Law Schemes

Since the exact solution of (3.28) exists, one can reasonably expect that an accurate scheme could be derived if the result of the exact solution (3.32), is utilized. (3.28) can be rewritten as:

$$\frac{d}{dx}\left(\rho u \varphi - \Gamma \frac{d\varphi}{dx}\right) = 0. \tag{3.33}$$

The total flux of J due to convection and diffusion is defined as:

$$J = \rho u \varphi - \Gamma \frac{d\varphi}{dx}. \tag{3.34}$$

Thus (3.33) becomes

$$\frac{dJ}{dx} = 0. \tag{3.35}$$

Integrating (3.35) over the control volume P in one-dimensional problem, yields

$$J_e = J_w. \tag{3.36}$$

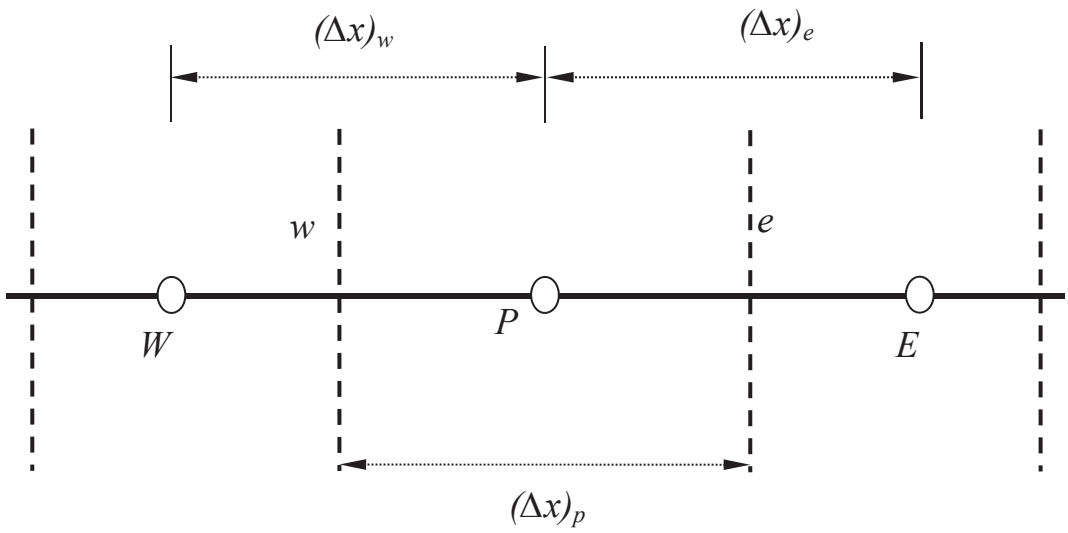

Fig. 3.5 Grid point for a one-dimensional problem.

The distribution of φ between grid points can be taken as that obtained from the exact solution (3.32). After employing (3.32) between grid points E and P corresponding to Fig. 3.5, we have:

$$\frac{\varphi(x)-\varphi_P}{\varphi_E-\varphi_P}=\frac{e^{\mathrm{Pe}_{\Delta e}\left[\frac{x-x_P}{(\delta x)_e}\right]}-1}{e^{\mathrm{Pe}_{\Delta e}}-1}. \tag{3.37}$$

Substituting (3.37) into (3.34) and evaluating the result at $x = x_e$, the total flux of J at the face of control volume becomes

$$J_e = F_e\left[\varphi_P+\frac{\varphi_P-\varphi_E}{e^{\mathrm{Pe}_{\Delta e}}-1}\right], \tag{3.38}$$

where the mass flux, F, can be given as follows:

$$F = \rho u. \tag{3.39}$$

Similarly, the total flux at the west face of the control volume is

$$J_w = F_w\left[\varphi_W + \frac{\varphi_W - \varphi_P}{e^{\mathrm{Pe}_{\Delta w}} - 1}\right]. \tag{3.40}$$

After substituting (3.38) and (3.40) into (3.36) and rearranging the resulting equation, the following standard form could be given by

$$a_P\varphi_P = a_E\varphi_E + a_W\varphi_W, \tag{3.41}$$

where

$$a_E = \frac{F_e}{e^{\mathrm{Pe}_{\Delta e}} - 1}, \tag{3.42}$$

$$a_W = \frac{F_w e^{\mathrm{Pe}_{\Delta w}}}{e^{\mathrm{Pe}_{\Delta w}} - 1}, \tag{3.43}$$

$$a_P = a_E + a_W + (F_e - F_w). \tag{3.44}$$

Equations (3.42) and (3.43) can be rewritten in another format as follows:

$$\frac{a_E}{D_e} = \frac{\mathrm{Pe}_{\Delta e}}{e^{\mathrm{Pe}_{\Delta e}} - 1}, \tag{3.45}$$

$$\frac{a_W}{D_w} = \frac{\mathrm{Pe}_{\Delta w} e^{\mathrm{Pe}_{\Delta w}}}{e^{\mathrm{Pe}_{\Delta w}} - 1}, \tag{3.46}$$

where diffusive conductance D is defined as:

$$D = \frac{\Gamma}{\delta x}. \tag{3.47}$$

In the Power Law scheme, the coefficient of the neighbor grid point on the east side is obtained by:

$$\frac{a_E}{D_e} = \begin{cases} -\mathrm{Pe}_{\Delta e} & \mathrm{Pe}_{\Delta e} \le -10 \\ \left(1 - 0.1\mathrm{Pe}_{\Delta e}\right)^5 - \mathrm{Pe}_{\Delta e} & -10 < \mathrm{Pe}_{\Delta e} \le 0 \\ \left(1 - 0.1\mathrm{Pe}_{\Delta e}\right)^5 & 0 < \mathrm{Pe}_{\Delta e} \le 10 \\ 0 & \mathrm{Pe}_{\Delta e} > 10 \end{cases} \tag{3.48}$$

which can be rewritten in the following compact form as:

$$\frac{a_E}{D_e} = [[0,(1-0.1\mathrm{Pe}_{\Delta e})^5]]+[[0,\text{-}\mathrm{Pe}_{\Delta e}]]. \tag{3.49}$$

(3.49) for another scheme under any grid Peclet number can be expressed as:

$$\frac{a_E}{D_e} = A(|\mathrm{Pe}_{\Delta e}|)+[[0,\text{-}\mathrm{Pe}_{\Delta e}]], \tag{3.50}$$

where $A(|\mathrm{Pe}_{\Delta e}|)$ in (3.50) for any schemes can be found in Table 3.2.

Table 3.2 Summary of $A(|\mathrm{Pe}_{\Delta e}|)$ for different schemes([PAT80])

Scheme	$A(\lvert\mathrm{Pe}_{\Delta e}\rvert)$
Central difference	$1-0.5\lvert\mathrm{Pe}_{\Delta e}\rvert$
Upwind	1
Hybrid	$[[0,1-0.5\lvert\mathrm{Pe}_{\Delta e}\rvert]]$
Exponential	$\frac{\lvert\mathrm{Pe}_{\Delta e}\rvert}{e^{\lvert\mathrm{Pe}_{\Delta e}\rvert}-1}$
Power Law	$[[0,(1-0.1\mathrm{Pe}_{\Delta e})^5]]$

A comparison between the Power Law scheme and other scheme is depicted in Fig. 3.6. In order to compare the Power Law scheme with other schemes, the exact solution for one-dimensional steady-state convection and diffusion is considered.

It is seen that the hybrid scheme is viewed as an envelope of the exponential scheme. The hybrid scheme is a good approximation if the absolute value of the grid Peclet number is either very large or near zero. While the exponential scheme is accurate, the computational time is much longer than for the central difference, upwind or hybrid schemes. Patankar [PAT80] proposed the Power Law scheme that has almost the same accuracy as the exponential scheme but also has a substantially shorter computational time.

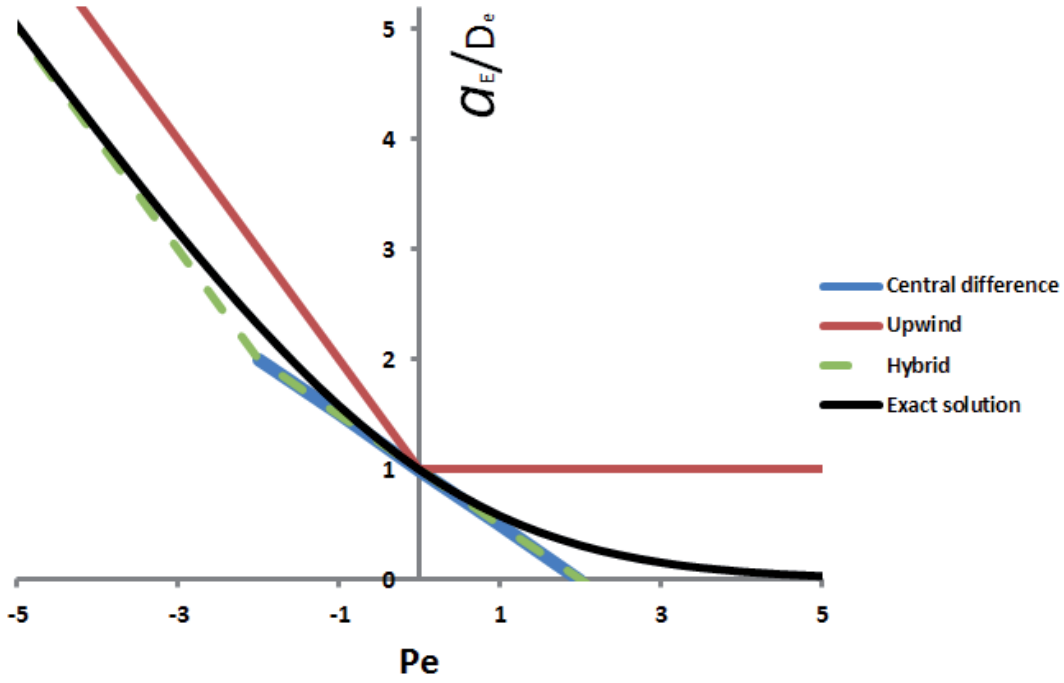

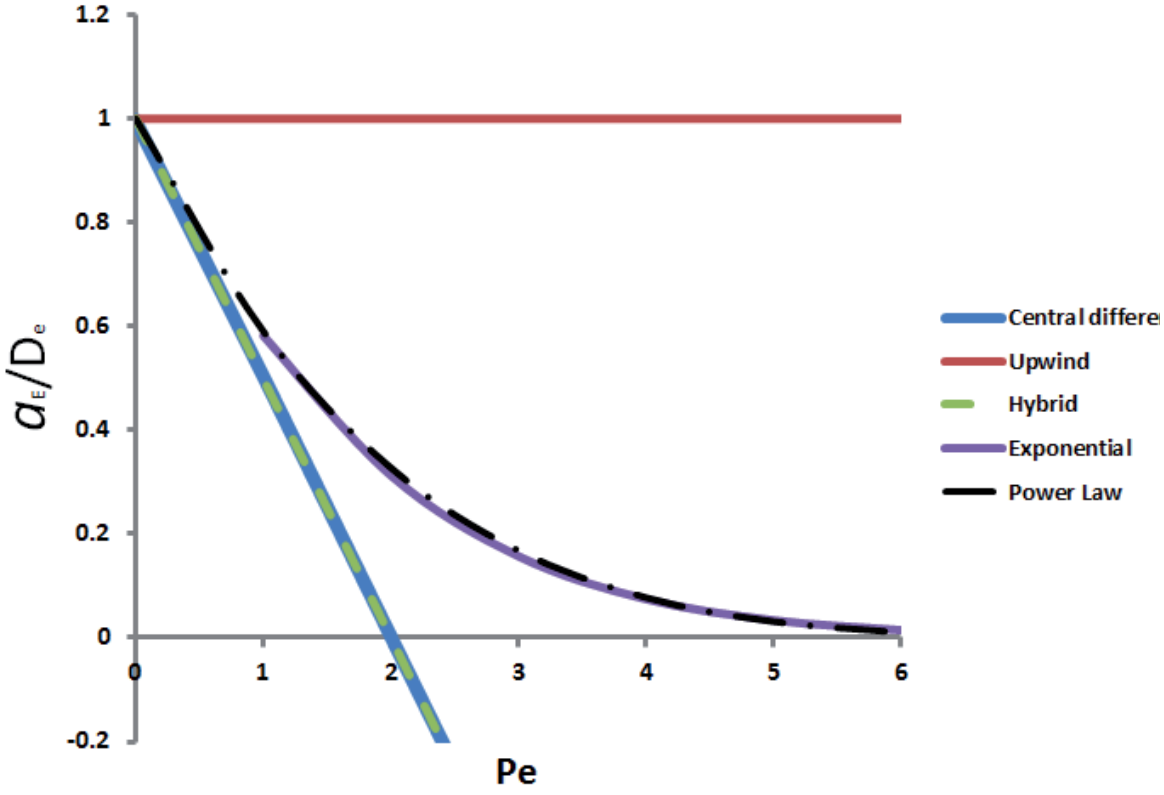

Fig. 3.6 Comparison among different schemes [PAT80]

Chapter 4

Straight Microchannels

Microchannels are composed of straight channels, curved channels or combinations of them. In this chapter, straight rectangular microchannels as parts of microfluidic systems are studied. Effects of rarefaction on forced convection heat transfer of laminar, steady and incompressible fluid flows in straight microchannels with uniform heat flux are considered. The slip velocity and the jump temperature boundary conditions at the wall are applied. The Navier-Stokes and energy equations are discretized using Finite Volume technique as described in the chapter 3. The calculated results show good agreement with previous numerical data and analytical solutions ([AKB10B], [AKB10C], [AKB09A], [AKB09B]).

4.1. Structure and Assumptions

The structure of two and three dimensional straight microchannels and appropriate coordinate systems are shown in Fig. 4.1 and Fig. 4.2, respectively. The flow is considered along the x-axis and the channel length L is chosen long enough to insure that fully developed flow conditions are reached at the outlet. Fully developed region is defined as the zone where the gradient in the axial direction in comparison with the gradients in the other directions can be neglected.

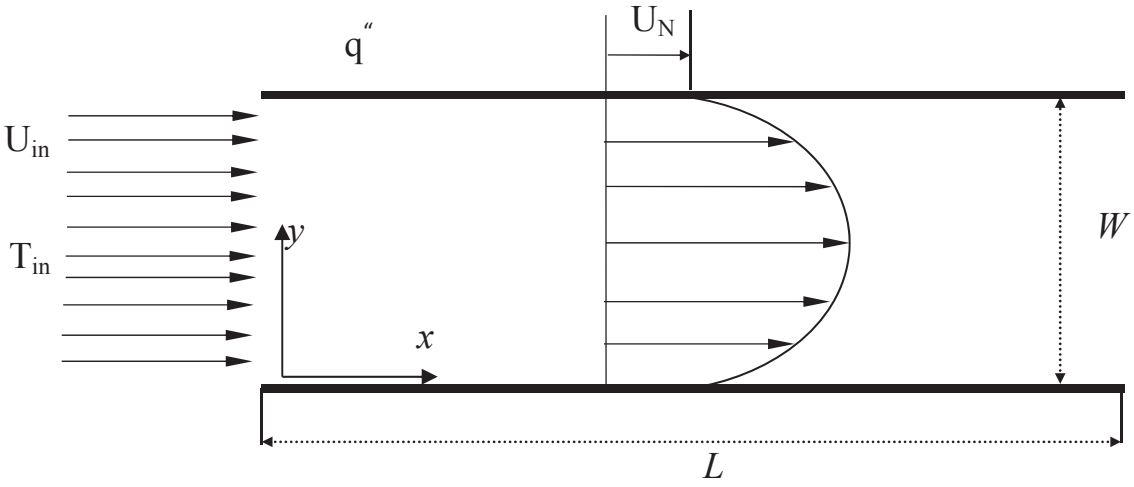

Fig. 4.1 Schematic diagram of a two-dimensional rectangular microchannel.

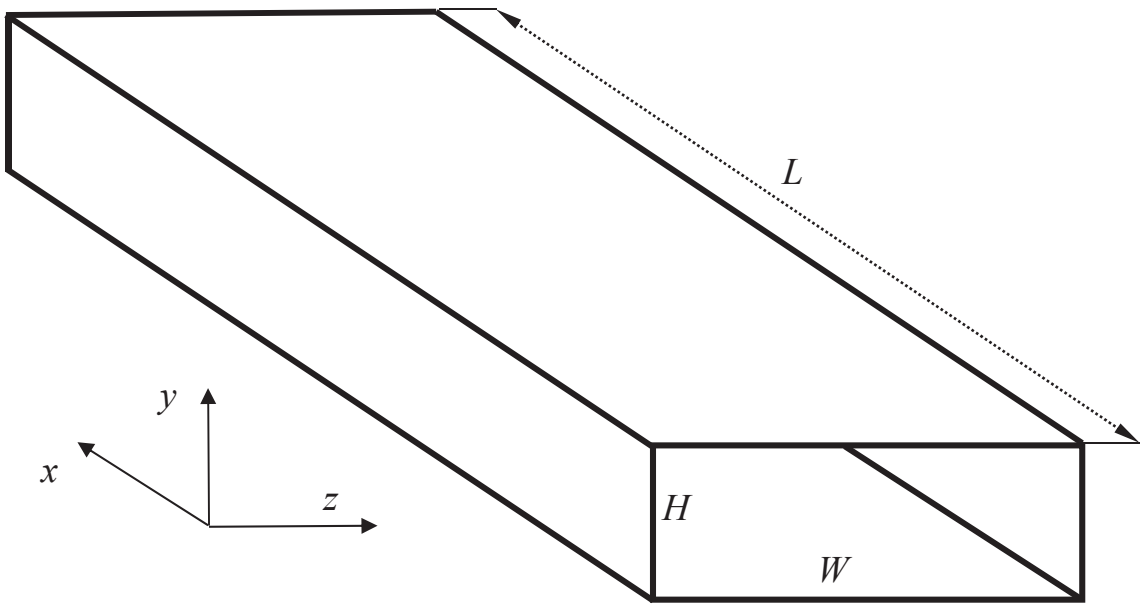

Fig. 4.2 Schematic diagram of a three-dimensional rectangular microchannel.

The slip flow and the heat transfer in rectangular microchannels are considered. The following assumptions are applied:

- The fluid flow is laminar, steady state and incompressible,
- The properties of fluid flow are assumed to be constant and homogeneous,

- Dissipation and pressure works are neglected,
- There is not any significant body forces (gravity force, magnetic force,…),
- The rarefaction effects set slip velocity and jump temperature at the fluid–wall interface.

4.2 Governing Equations

With the above assumptions, the steady state governing equations describing the fluid flow and the heat transfer in a three-dimensional rectangular straight microchannel in the Cartesian coordinate can be derived from Equations (3.1)-(3.4) as follows:

- continuity equation:

$$\frac{\partial u}{\partial x}+\frac{\partial v}{\partial y}+\frac{\partial w}{\partial z}=0, \tag{4.1}$$

- momentum equation in x direction:

$$\rho\left(u\frac{\partial u}{\partial x}+v\frac{\partial u}{\partial y}+w\frac{\partial u}{\partial z}\right)=\mu\left(\frac{\partial^2 u}{\partial x^2}+\frac{\partial^2 u}{\partial y^2}+\frac{\partial^2 u}{\partial z^2}\right)-\frac{\partial p}{\partial x}, \tag{4.2}$$

- momentum equation in y direction:

$$\rho\left(u\frac{\partial v}{\partial x}+v\frac{\partial v}{\partial y}+w\frac{\partial v}{\partial z}\right)=\mu\left(\frac{\partial^2 v}{\partial x^2}+\frac{\partial^2 v}{\partial y^2}+\frac{\partial^2 v}{\partial z^2}\right)-\frac{\partial p}{\partial y}, \tag{4.3}$$

- momentum equation in z direction:

$$\rho\left(u\frac{\partial w}{\partial x}+v\frac{\partial w}{\partial y}+w\frac{\partial w}{\partial z}\right)=\mu\left(\frac{\partial^2 w}{\partial x^2}+\frac{\partial^2 w}{\partial y^2}+\frac{\partial^2 w}{\partial z^2}\right)-\frac{\partial p}{\partial z}, \tag{4.4}$$

- fluid energy equation:

$$\rho C_p\left(u\frac{\partial T}{\partial x}+v\frac{\partial T}{\partial y}+w\frac{\partial T}{\partial z}\right)=k\left(\frac{\partial^2 T}{\partial x^2}+\frac{\partial^2 T}{\partial y^2}+\frac{\partial^2 T}{\partial z^2}\right), \tag{4.5}$$

where ρ is density, μ is dynamic viscosity, C_p is specific heat, k is thermal conductivity, T is temperature, p is pressure and u, v *and* w are the velocity components.

The continuity, momentum and energy equations are non-dimensionalized using the following dimensionless parameters:

$$X_i = \frac{x_i}{D_h}\ ,\ U_i = \frac{u_i}{u_{in}}\ ,\ P = \frac{p}{\rho u_{in}^2}\ ,\ T^* = \frac{T - T_{in}}{\left(q'' D_h\right)/k}, \tag{4.6}$$

where subscript '*in*' is related to the value of the parameter at the inlet and q'' is a constant heat flux at the wall. The dimensionless governing equations in tensor forms can be given as follows:

- continuity equation:

$$\frac{\partial U_j}{\partial X_j} = 0, \tag{4.7}$$

- momentum equations:

$$\frac{\partial}{\partial X_j}(U_j U_i) = \frac{1}{\mathrm{Re}}\left(\frac{\partial^2 U_j}{\partial X_i^2}\right) - \frac{\partial P}{\partial X_j}, \tag{4.8}$$

- fluid energy equation:

$$\frac{\partial}{\partial X_j}\left(U_j T^*\right) = \frac{1}{Pe}\frac{\partial^2 T^*}{\partial X_j}, \tag{4.9}$$

where $Pe = \mathrm{Re}\,\mathrm{Pr}$, $\mathrm{Re} = \frac{\rho u_{in} D_h}{\mu}$ and $\mathrm{Pr} = \frac{\mu c_p}{k}$ are the Peclet number, the Reynolds number and the Prandtl number, respectively (see Appendix A for details about dimensionless numbers).

4.3 Rarefaction implementation

The first order dimensionless velocity slip and jump temperature condition are considered as expressed in Equation (3.7) and Equation (3.8). With the following procedure, the slip velocity and the jump temperature boundary conditions can be employed in the discretization equations as a standard form in the Finite Volume method.

In order to simplify, a two-dimensional control volume close to the wall boundary is shown in Fig. 4.3. The slip velocity near the wall results from Equation (3.7) in

$$U_N - U_{wall} = Kn \left.\frac{\partial U}{\partial Y}\right|_{wall}, \tag{4.10}$$

where U_{wall} is equal to zero. By applying the first order approximation for the velocity gradient near to the wall we obtain:

$$\left.\frac{\partial U}{\partial Y}\right|_{wall} = \frac{U_P - U_N}{\Delta Y}. \tag{4.11}$$

Inserting (4.11) into (4.10) we obtain:

$$U_N - U_{wall} = Kn \frac{U_P - U_N}{\Delta Y}. \tag{4.12}$$

After arranging we have:

$$U_N - U_P = \frac{\left(U_{wall} - U_P\right)}{\left(1 + \frac{Kn}{\Delta Y}\right)}. \tag{4.13}$$

The discretized momentum equation for a control volume adjacent to the wall from Patankar [PAT80] is given as:

$$a_N\left(U_N - U_p\right) + a_S\left(U_S - U_p\right) + a_E\left(U_E - U_p\right) + a_W\left(U_W - U_p\right) + b = 0. \tag{4.14}$$

After replacing the term (U_N-U_P) in (4.14) by (4.13), it is written as:

$$\frac{\left(a_N\right)}{\left(1 + \frac{Kn}{\Delta Y}\right)}\left(U_N - U_p\right) + a_S\left(U_S - U_p\right) + a_E\left(U_E - U_p\right) + a_W\left(U_W - U_p\right) + b = 0. \tag{4.15}$$

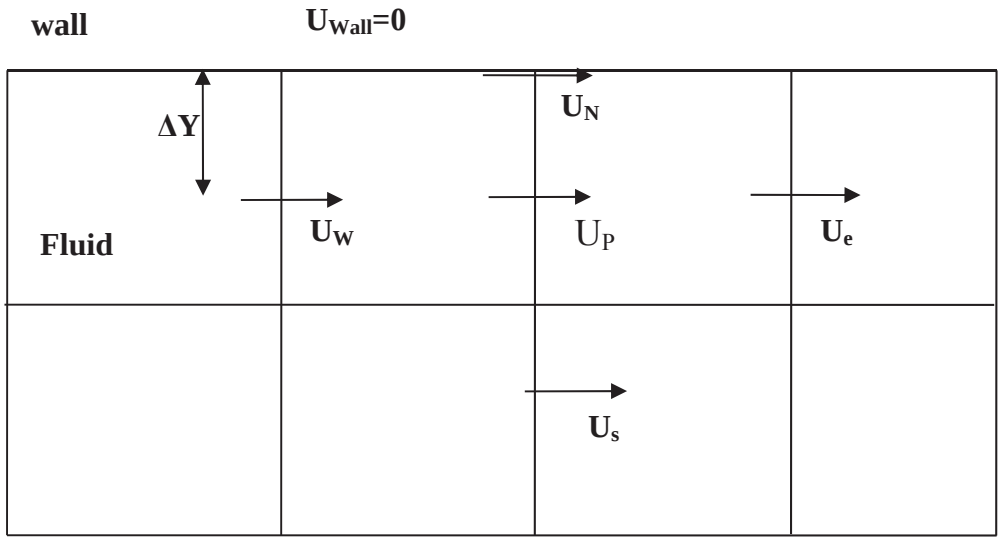

Fig. 4.3 Control volume close to the wall.

This form can be used as Equation (3.10) in algebraic discretized equations. A similar procedure for the jump temperature boundary condition in the discretized energy equation can be given as proposed by Hettiarachchi et al. [HET08]:

$$\frac{(b_N)}{\left(1+\frac{Kn}{\beta \Delta Y}\right)}(\theta_N-\theta_p)+b_S(\theta_S-\theta_p)+b_E(\theta_E-\theta_p)+b_W(\theta_W-\theta_p)+b_T=0. \tag{4.16}$$

4.4. Boundary Conditions

The nonlinear governing equations (4.7) to (4.9) are solved with the following appropriate boundary conditions:

- At the channel inlet: the fluid velocity and the temperature profiles are assumed uniform and constant (U=1 and T^*=0). Pressure is calculated at the inlet,
- At the fluid-solid interface: The velocity in the direction normal to the walls is zero. The slip velocity adjacent to the wall is proportional to

normal velocity gradient at the wall (4.10). The jump temperature adjacent to the wall is proportional to the temperature gradient at the fluid–wall interface (4.11). A uniform and constant heat flux ($\left.\frac{\partial T^*}{\partial Y}\right|_{wall} = -1$) at the wall is applied,

- At the channel outlet: the diffusion flux in the direction normal to the exit is assumed to be zero for the velocity and the temperature while a zero pressure is assigned at the flow exit.

4.5 Numerical methods

The sets of coupled non-linear differential equations ((4.7) to (4.9)) are discretized using the Finite Volume technique whereas the Power Law scheme is used for the convective and diffusive terms. The SIMPLER procedure is introduced to couple velocity and pressure as described in Chapter 3. The slip velocity and the jump temperature boundary conditions are discretized and employed in the discretization equations.

A structured non uniform grid distribution is used for the computational domain. It is finer near the microchannel entrance and near the wall where the velocity and the temperature gradients are high. Channel lengths are set to a value greater than the estimated entrance lengths of the flow to ensure that fully developed conditions are achieved at the exit.

The test of independency of results on the grid distribution is essential for a numerical work. Therefore, several different grid distributions are tested to ensure that the calculated results are grid independent. As it is shown in Fig. 4.4, increasing the quantity of nodes in the case of two-dimensional flow more than 60 nodes in y direction and 160 nodes in x direction will not change the velocity significantly. In the three dimensional case, 20×20 nodes in any cross section and 160 nodes in axial direction will do it. Therefore, the selected grid for the

present calculations consists of 60×160 and 20×20×160 nodes for two-and three-dimensional, respectively. The solution is assumed converged when $\left|\frac{\left(\phi^{n+1}-\phi^{n}\right)}{\phi^{n+1}}\right| \leq 10^{-6}$ is satisfied for all independent variables.

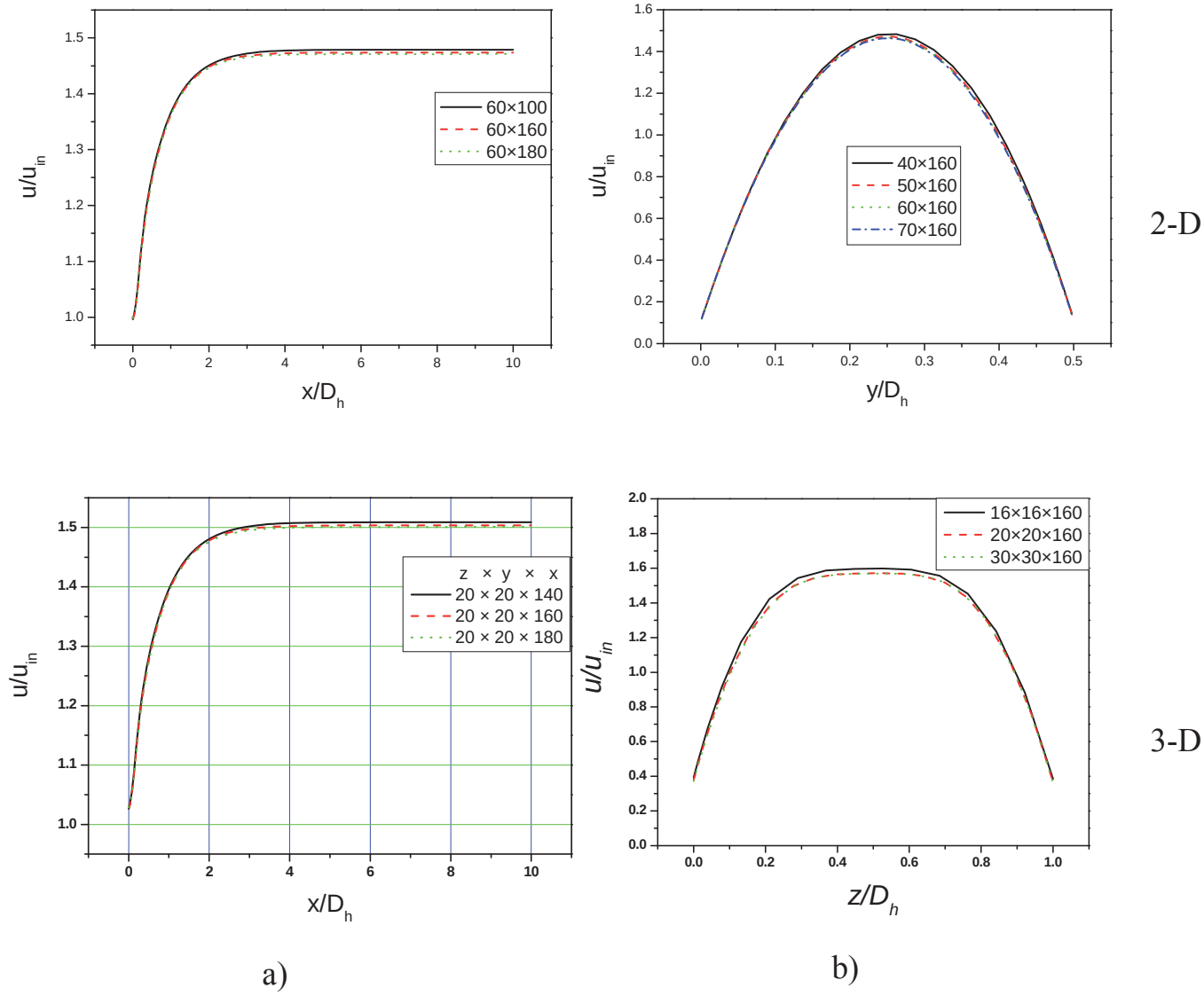

Fig. 4.4 Grid independent test a) in x direction b) in y direction.

4.6 Validations

In order to demonstrate the validity and precision of the model assumptions and the numerical analysis, several calculated variables are compared with corresponding published experimental and numerical data.

The fully developed values of the Poiseuille number ($f\,\mathrm{Re} = \dfrac{\tau_w \; D_h}{\frac{1}{2}\mu\,\bar{u}}$ where f is Fanning friction coefficient , $f = \dfrac{\tau_w}{\frac{1}{2}\rho\bar{u}^2}$ and τ_w is shear stress at the wall, $\tau_w = -\mu \left.\dfrac{\partial u}{\partial y}\right|_{wall}$) is compared with available numerical and analytical solution at Re=100 and different Kn. The calculated Poiseuille numbers in Table 4.1 show a good agreement with numerical results by Renksizbulut et al. [REN06] and analytical values, which vary with Kn according to $f\,\mathrm{Re}_{fd} = \dfrac{24}{(1+12Kn)}$.

Table 4.1. Comparison of the Poiseuille number at fully developed region .

Kn	$(f\,\mathrm{Re})_{fd}$		
	Analytical solution	Previous numerical results **[REN06]**	Present calculation
0	24.00	23.87	24.25
0.001	23.72	-	23.95
0.005	22.64	22.54	22.79
0.01	21.43	21.33	21.53
0.025	18.46	18.39	18.48
0.05	15.00	14.95	14.96
0.1	10.91	10.88	10.91

The local Nusselt numbers are presented and compared in Fig. 4.5 with published results carried out by Yu and Ameel [YU01] for Kn=0.04, β=10 and infinity aspect ratio. As seen from this figure, also a significant agreement between the calculated and numerical results is observed.

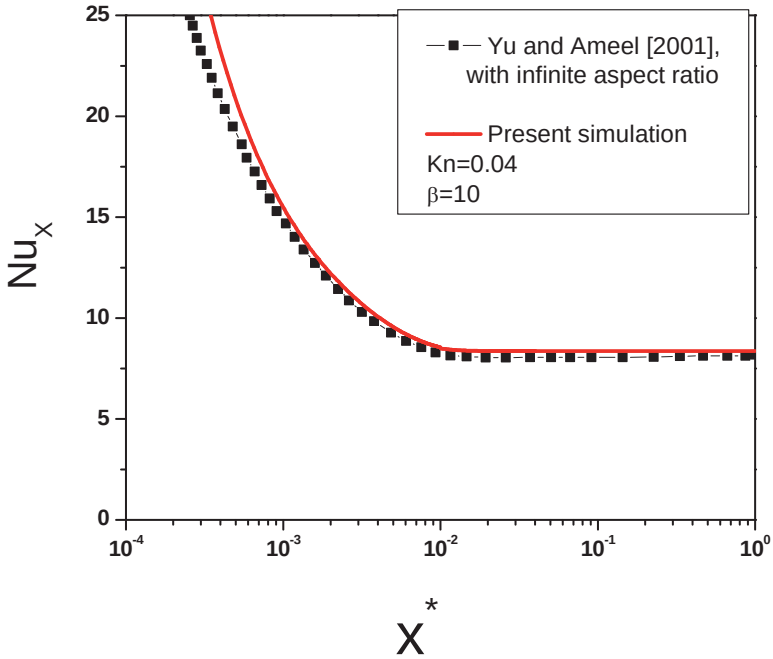

Fig. 4.5 Comparison of the local Nusselt number with results of [Yu01] for Kn=0.04 and *β*=10 with infinity aspect ratio.

The calculated velocity at the developed region is compared with corresponding experimental results carried out by Wang and Wang [WAN09] for water at Re=100 and 200 in two different square microchannels as shown in Fig. 4.6. They investigated the fluid flow in square microchannels experimentally and they measured the velocity of water in microchannel with 0.4 mm and 0.8 mm widths by using a micro-PIV technique (Particle Image Velocimetry technique). We have set very small Kn equal to 0.001 for this validation. As can be seen from the figure, the present computation is in excellent agreement with the experimental results at different widths of the square microchannel.

The comparisons show that the numerical procedure, assumptions made and the used codes with MATLAB programming are correct and reliable.

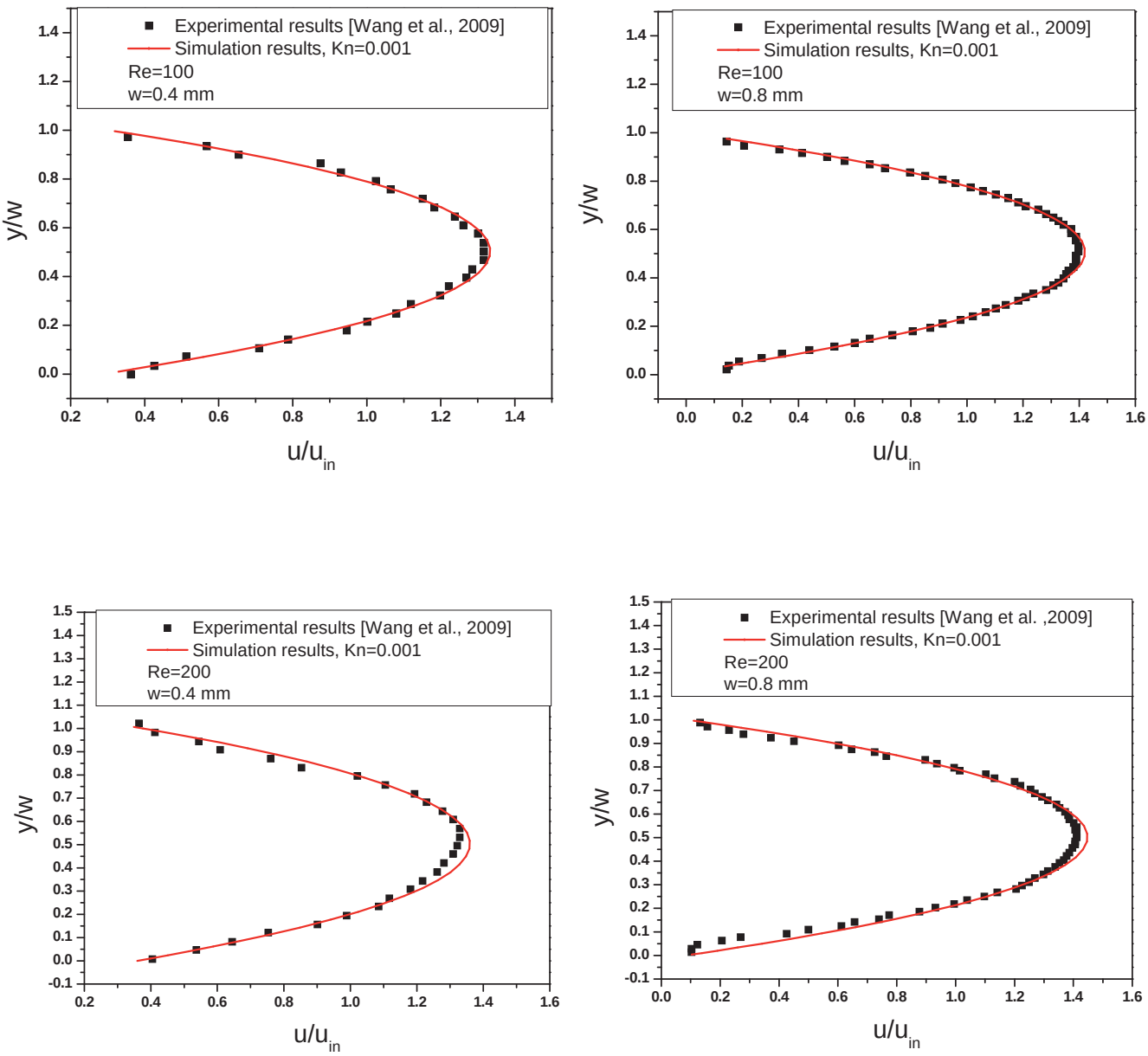

Fig. 4.6 Comparison of the non-dimensional velocity with results of [WAN09] at Re=100 and 200 for W=0.4 and 0.8 mm.

4.7 Results and Discussion

Numerical simulations are done on a wide range of Re and Pe for different values of the Knudsen number. Because of similar behaviors and lack of space, the results presented here are only for $1 \leq Re \leq 600$ and $1 \leq Pe \leq 700$ with different values of slip velocity and jump temperature ($0 \leq Kn \leq 0.1$ and $0.6 \leq \beta \leq 10$). X^* denotes to reciprocal Graetz number ($x/(D_h\ Pe)$). Constant heat fluxes are applied on the walls and the result of thermal and hydraulics field are presented and discussed in the following.

4.7.1 Velocity field

The developing process of velocity profiles at different Re for Kn=0.01 are shown in Fig. 4.7. At the beginning of the microchannel, the velocity profiles are very steep near the wall and they are uniform in the center. In stream wise direction, the velocity gradient near the wall becomes smooth while the maximum velocity appears at the centerline. The fully developed condition takes place at X=1.0720 for the case of Re=20 and Kn=0.001, and it takes place at X=3.5977 for the case of Re=200 and Kn=0.01.

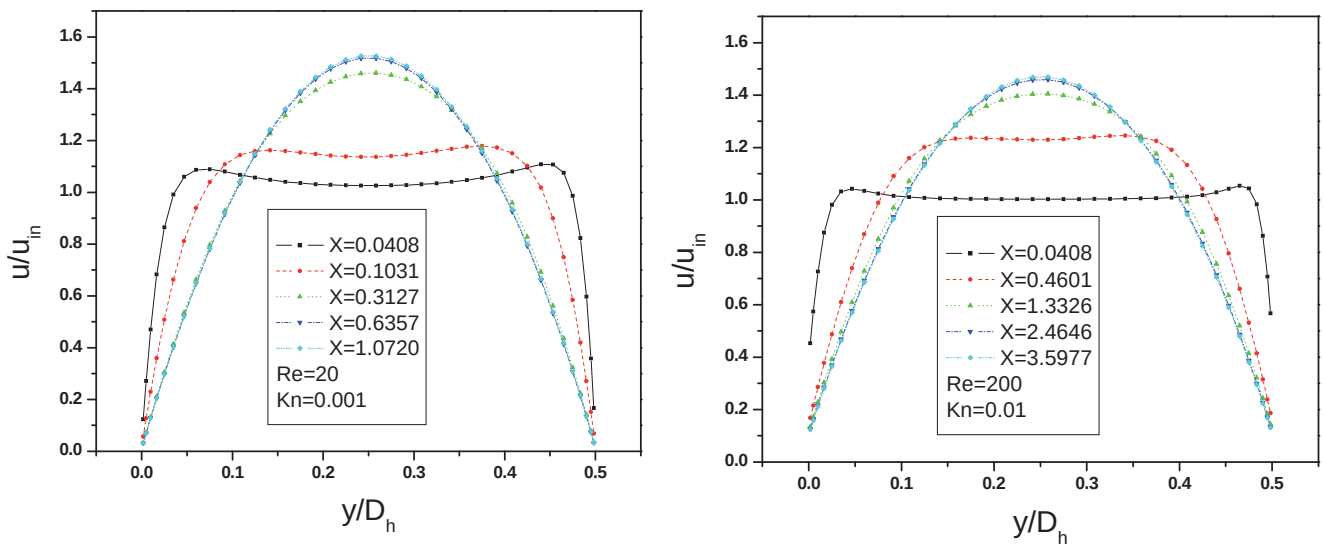

a) b)

Fig. 4.7 Developing of the non-dimensional velocity profile at a) Re=20, Kn=0.001 and b) Re=200, Kn=0.01.

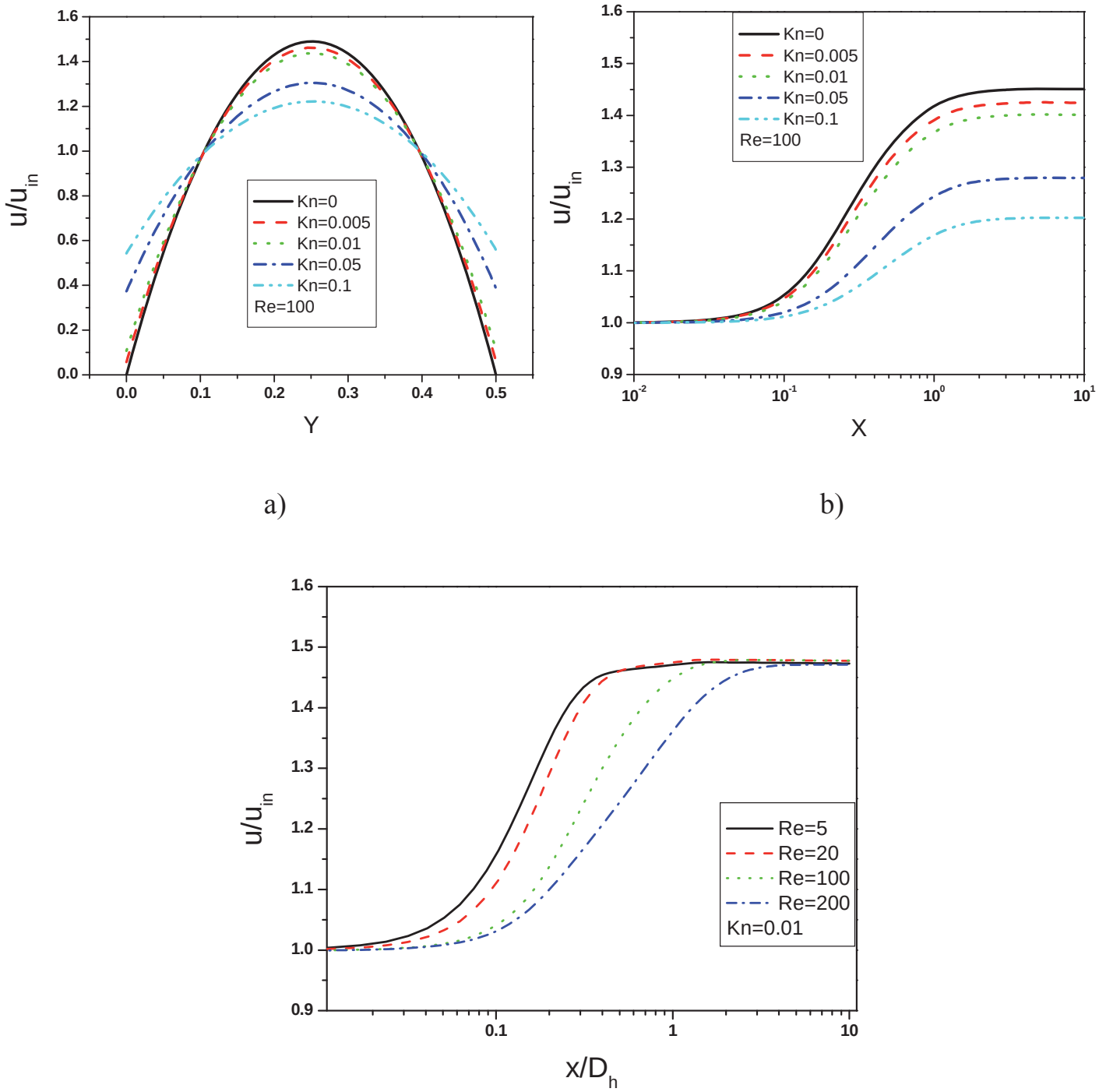

Fig. 4.8 Variation of the non-dimensional velocity with Kn.

The non-dimensional velocity profiles for different Kn and Re are shown in Fig. 4.8. It is shown that at any Re, the slip velocity causes to augment the velocity near the wall while the maximum velocity at the center line reduces. It

is illustrated that the velocity distribution in microchannels (slip flow) is flattened compared to continuum flows (Kn=0).

Fig. 4.8. shows that the velocity at the center line (maximum velocity) is decreased by increasing the slip velocity (increasing Kn) at any Re. The maximum non-dimensional velocity at fully developed region is decreased about 25% by increasing Kn to 0.1. Fig. 4.8.c presents that the Reynolds number has a reducing effect on the maximum non-dimensional velocity at the beginning of the microchannel. It further postpones the fully developed condition whereas it does not have any significant effect on the maximum fully developed velocity.

4.7.2 Pressure field

The variation of the non-dimensional pressure profile with Kn at two different Re is shown in Fig. 4.9. After passing the entrance region, the local pressure decreases linearly along the microchannel. The slip velocity has a decreasing effect on the local pressure at any Reynolds number. Fig. 4.9b illustrates that the pressure is uniform and constant at any cross section at the fully developed region. It means that after passing the entrance length, the pressure is not a function of y and behaves like the non-slip flow regime; it varies linearly along the microchannel. There is a smaller pressure drop in a microchannel compared to the continuum flows (Kn=0).

The variation of pressure drops as a function of the Knudsen number and the Reynolds number in microchannels are presented in Fig. 4.10. The slip velocity allows the fluid to flow near the wall, therefore takes place a smaller pressure drop than non-slip flow. It is also shown in Fig. 4.10a that increasing Kn has a decreasing effect on the pressure drop in channels at any Re, as much as 50% by increasing Kn to 0.1. Fig. 4.10b depicts that, as expected, the Reynolds number has an increasing effect on the pressure drop.

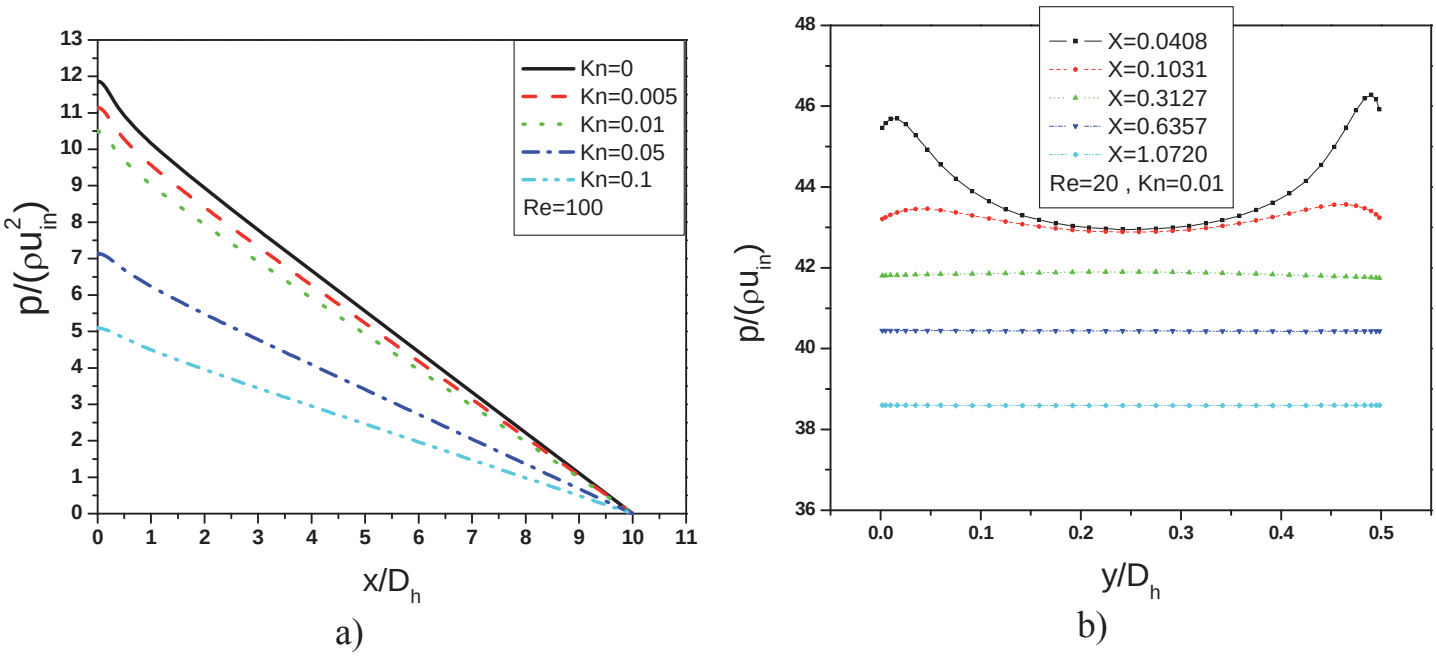

Fig. 4.9 Variation of the non-dimensional pressure with Kn.

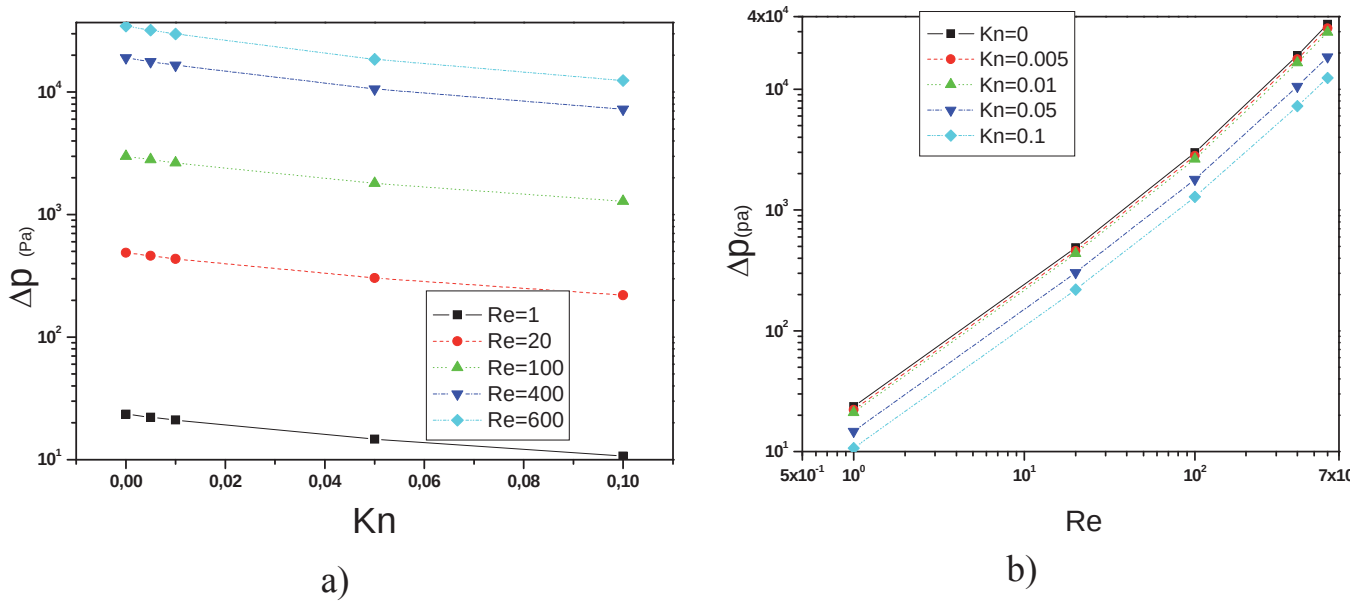

Fig. 4.10 The pressure drop in microchannels at different Re and Kn.

4.7.3 Entrance length

The effects of the slip velocity and Re on the variations of the entrance length in the microchannels are presented in Fig. 4.11. The dimensionless entrance length, X_{en} , is defined as the distance where the maximum velocity reaches 99% times the corresponding fully developed value over hydraulic diameter. Fig. 4.11 illustrates that the slip velocity has an increasing effect on the entrance length at any Re, but its effect is more significant at higher Re.

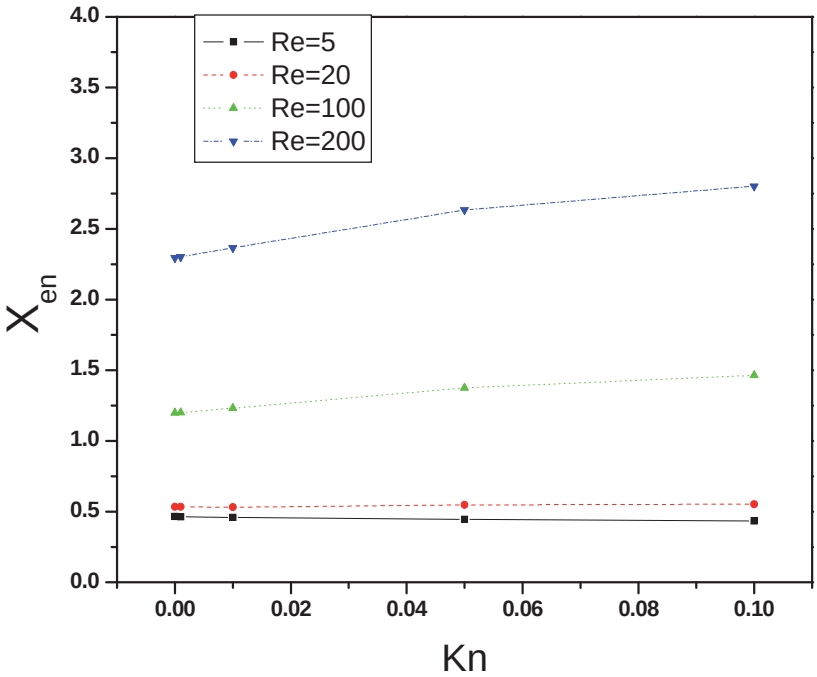

Fig. 4.11 Effect of the slip velocity on the non-dimensional entrance length at different Re.

4.7.4 Skin friction factor

The local Poiseuille number (fRe) is obtained by:

$$f\,\mathrm{Re} = 2\frac{\left.\dfrac{\partial u}{\partial y}\right|_{wall}}{\bar{u}} D_h . \tag{4.17}$$

After using dimensionless parameters, it becomes as follow:

$$f\,\mathrm{Re} = 2\left.\frac{\partial U}{\partial Y}\right|_{wall} . \tag{4.18}$$

By submitting the term $\left.\frac{\partial U}{\partial Y}\right|_{wall}$ from (4.10) into (4.18), the friction coefficient is expressed as:

$$f\,\mathrm{Re} = \frac{2}{Kn} U_{cw} \,. \tag{4.19}$$

Variation of the Poiseuille number with Kn for different Re is illustrated in Fig. 4.12. The figures show that in the entrance region, the slip velocity results in a large reduction of the friction coefficient. For the non-slip flow, $X = 0$ is a singularity plane resulting in an infinitely large wall shear. In the case of the slip flows, the friction coefficient value at the channel inlet is finite, as seen in Fig. 4.12. This can be obtained simply by substituting the inlet velocity boundary condition(U_{in}=1) into (4.19). Thus it can be easily shown that as $X \to 0 : f\,\mathrm{Re}(0) \to \frac{2}{Kn}$. The friction coefficient profiles start with value nearly $\frac{2}{Kn}$ for the case of slip flow (Kn=0.01 and Kn=0.1) while its value is infinite for the non-slip flow (Kn=0). Increasing Kn causes the local friction factor in microchannels reduces for any Re. Because in the slip flow regimes, the layer of fluid close to the wall can flow. Furthermore the changes in the stream-wise velocity profile to reach its final fully developed profile require much less momentum in compared to the non-slip flow regimes. It is interesting that in the case of high Kn (Kn=0.1), the local friction coefficient values do not change significantly from the inlet to the outlet (see Fig. 4.12c).

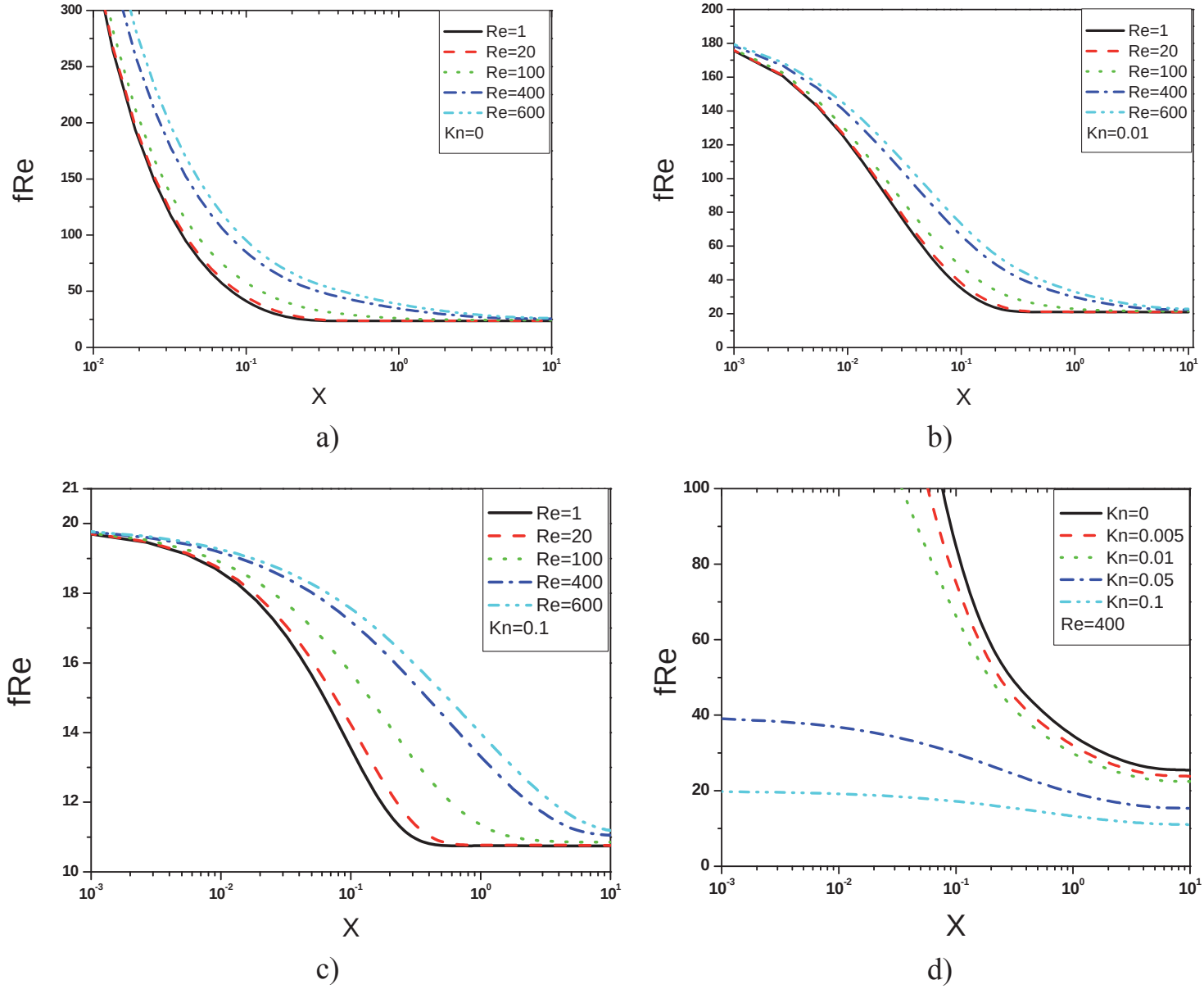

Fig. 4.12 Variation of the local Poiseuille number with Re and Kn.

4.7.5 Temperature field

Effects of the slip velocity and the jump temperature on the temperature field are shown in Fig. 4.13. Increasing the slip velocity and the jump temperature (increasing Kn) has a reducing effect on the temperature at any cross section, but this effect is more significant when the jump temperature is high (for smaller value of β). Because the jump temperature does not increase significantly with the increasing Kn at high value of β (β=7). Reducing jump temperature

(increasing β) does not have any significant effect on the temperature at any cross section for the case of Kn=0.01. However, an increase in the Knudsen number causes the temperature of fluid closed to the wall to decrease.

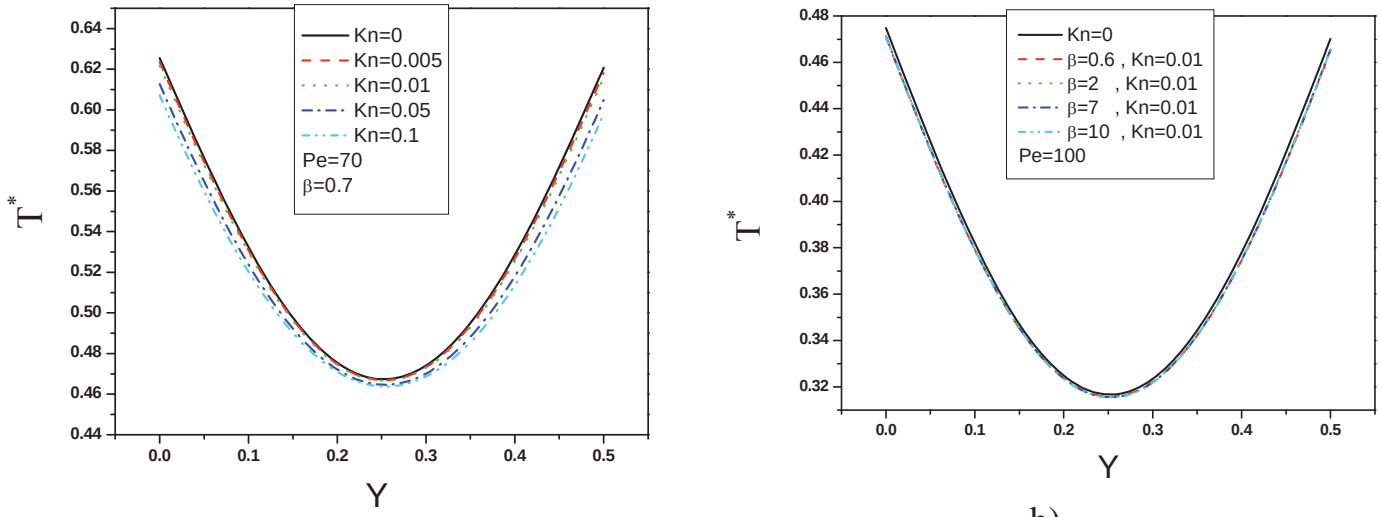

a) b)

Fig. 4.13 Variation of the non-dimensional temperature at the outlet with the Knudsen number.

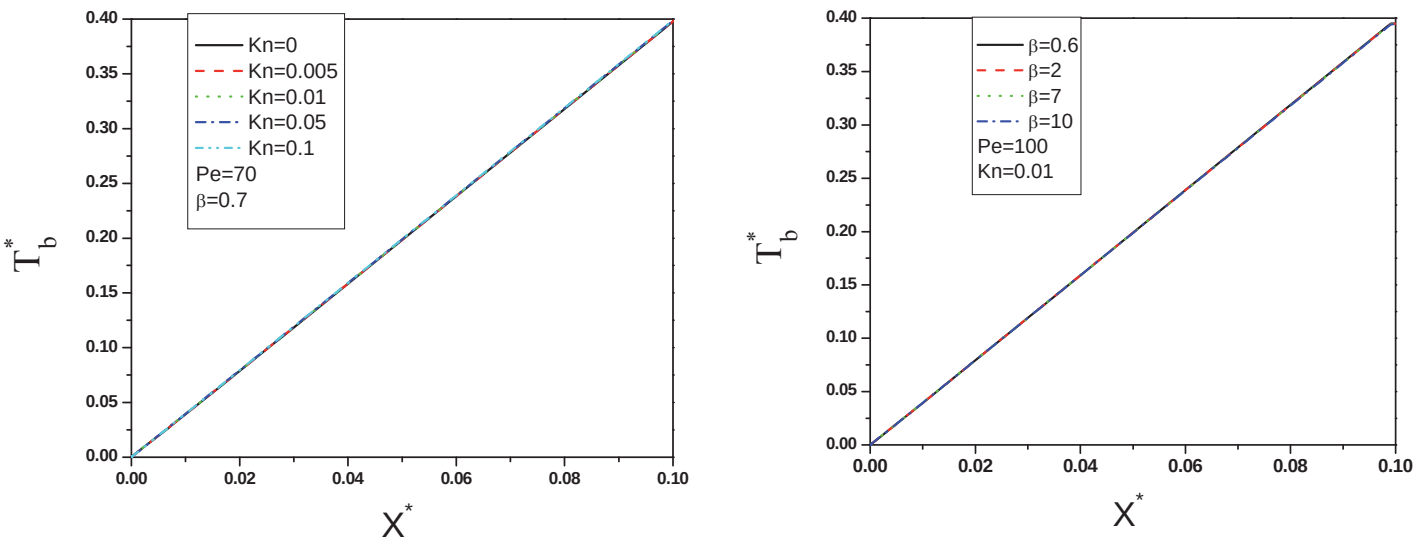

a) b)

Fig. 4.14 Effect of rarefaction on the non-dimensional bulk temperature.

In the case of the fluid flows inside a uniformly heated tube, the bulk temperature is well known to vary linearly along the channel. The energy balance from the inlet to any cross section over the channel can be written as follows:

$$2\,x\,q'' = \dot{m}c_p\left(T_b - T_{in}\right), \tag{4.20}$$

therefore

$$T_b - T_{in} = \frac{4x\,q''}{\rho u_{in}\,D_h\,c_p}, \tag{4.21}$$

then

$$\frac{T_b^*}{X} = \frac{4\,k}{\rho\,u_{in}\,D_h\,c_p}. \tag{4.22}$$

The right side of (4.22) is dependent only on the properties of the fluid and microchannel. Consequently, in the case of uniform heat flux, the bulk temperature varies linearly from the inlet to out of channel, as is illustrated by Fig. 4.14. Variation of the bulk temperature with the slip velocity and the jump temperature is presented in Fig. 4.14. The slip velocity and the jump temperature do not have any effect on the bulk temperature.

4.7.6 Nusselt number

The local Nusselt number (Nu) is obtained by:

$$Nu = \frac{hD_h}{k}, \tag{4.23}$$

where

$$h = \frac{q''}{\left(T_{wall} - T_b\right)}, \tag{4.24}$$

$$q'' = -k\left.\frac{\partial T}{\partial y}\right|_{wall}. \tag{4.25}$$

After applying (4.24) and (4.25) into (4.23) and making it non-dimensional, the local Nusselt number is calculated from:

$$Nu = \frac{-\left.\frac{\partial T^*}{\partial Y}\right|_{wall}}{T^*_{wall} - T^*_b}. \tag{4.26}$$

By substituting the term $\left.\frac{\partial T^*}{\partial Y}\right|_{wall}$ from (4.11) into (4.26), the local Nusselt number is expressed as:

$$Nu = \frac{\frac{\beta}{Kn}\left(T^*_{wall} - T^*_{cw}\right)}{T^*_{wall} - T^*_b}. \tag{4.27}$$

On the other hand, by applying (4.24) into (4.23) we obtain:

$$Nu = \frac{D_h}{k}\frac{q''}{\left(T_{wall} - T_b\right)}. \tag{4.28}$$

After making (4.28) non-dimensional, the local Nusselt number for the case of uniform heat flux is expressed as:

$$Nu = \frac{1}{T^*_{wall} - T^*_b}. \tag{4.29}$$

Variation of the local Nusselt number with the Peclet number in the non-slip flow and the slip flow is shown in Fig. 4.15. In the non-slip flow, Nu_x starts from an infinite value and drops extremely to get the fully developed value. Due to the presence of the slip velocity and the jump temperature in the slip flow, Nu_x starts with a finite value. Similar to the skin friction factor, for the non-slip flow $X = 0$ has a singularity plane for the Nusselt number, but it has a finite value for the slip flow regime which can be obtained from (4.27). At the channel inlet where $X = 0$, the non-dimensional temperature(T^*) and the non-dimensional bulk temperature T^*_b in (4.27) are near zero and therefore $X \to 0 : Nu(0) \to \frac{\beta}{Kn}$. It is illustrated in Fig. 4.15 that after passing the beginning part of the channel, the local Nusselt number behaves the same in both the slip flow and non-slip flow regimes. Increasing the Peclet number causes the local Nusselt number to increase at any Kn and β.

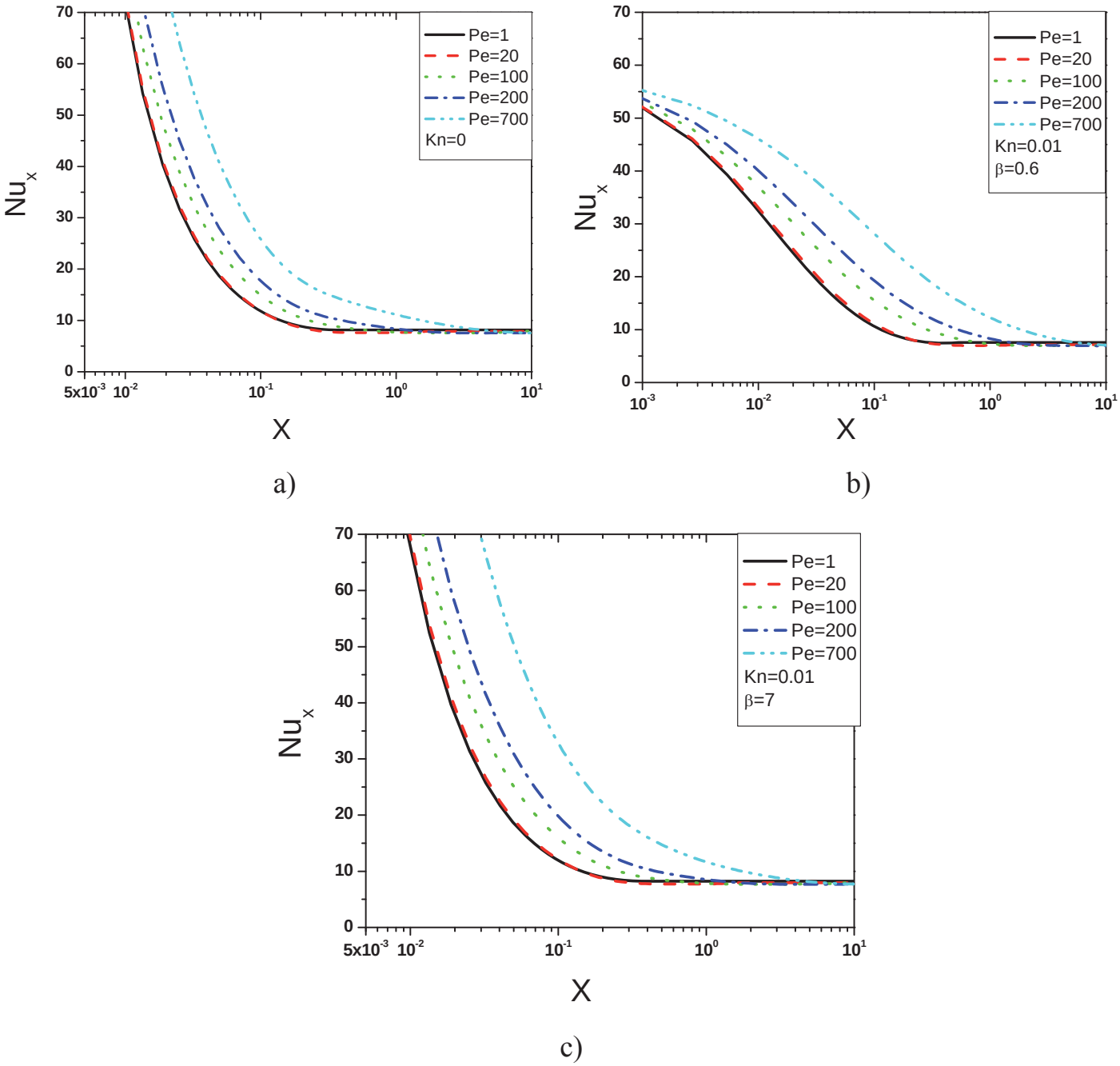

Fig. 4.15 The local Nusselt number profiles for different Peclet number at a) Kn=0, b) Kn=0.01, β=0.6 and c) Kn=0.1, β=7.

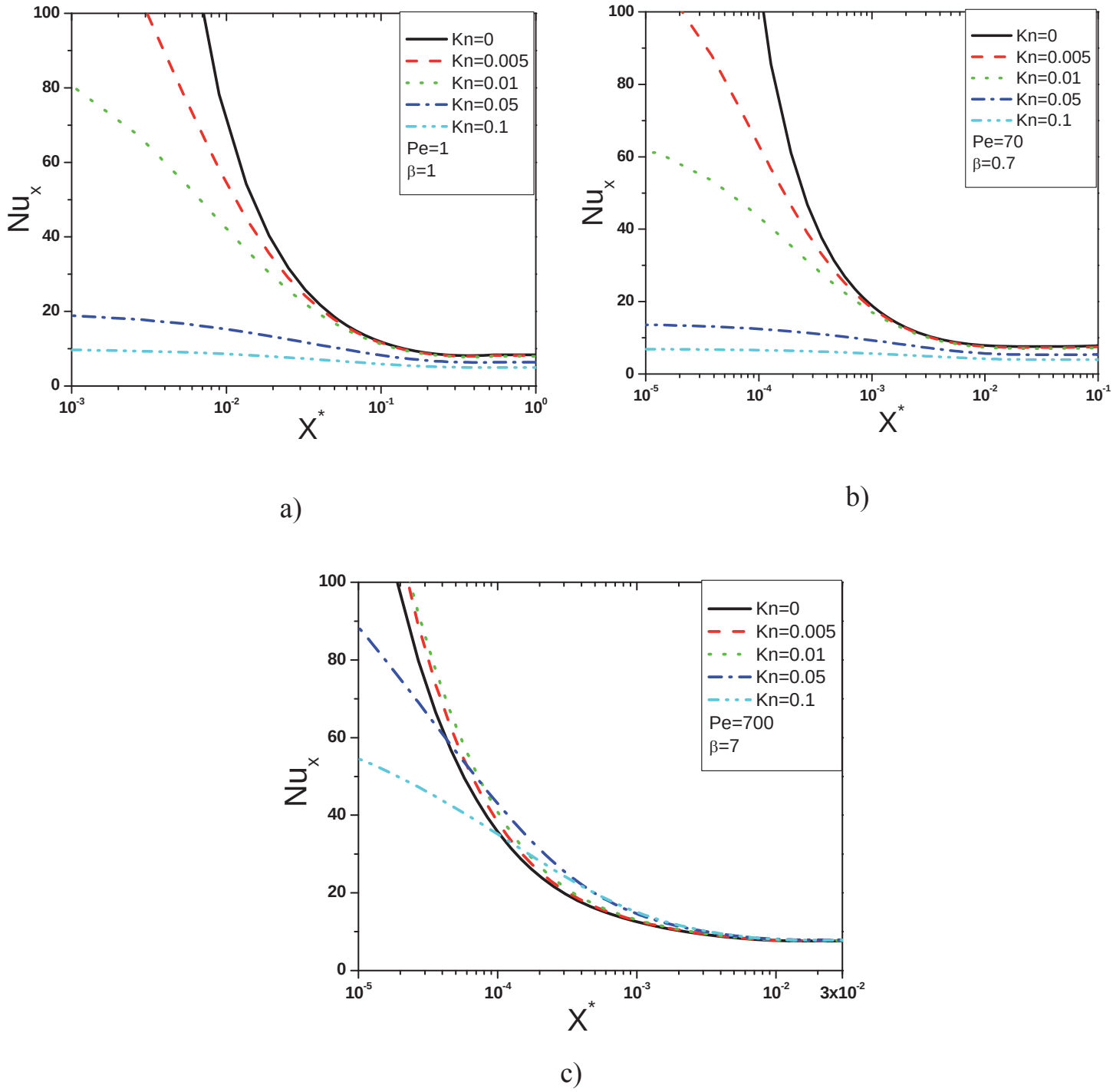

Fig. 4.16 Effects of the slip velocity on the local Nusselt number at a) Pe=1, β=1 , b) Pe=70, β=0.7 and c) Pe=700, β=7.

Variation of the local Nusselt number along the channel with the slip velocity at different jump temperature is shown in Fig. 4.16. In the slip flow, the presence of the slip velocity and the jump temperature significantly affects the local Nusselt number. The slip velocity increases the advection near the wall, therefore the heat transfer increases. In addition, the jump temperature increases

the thermal resistance at the wall-fluid interface causing a decrease in the heat transfer. The combined effect of the slip velocity and the jump temperature could increase or decrease the heat transfer, depending on their relative magnitude. It is shown in Fig. 4.16a and Fig. 4.16b that although both the slip velocity and the jump temperature increase with increasing Kn, it results in a decrease in Nu at the cases of high jump temperature (β=0.7and 1). The local Nusselt number increases or decreases with increasing Kn according to the relative Kn magnitude for the case of low jump temperature (β=7) (see Fig. 4.16c). It is evident that increasing effect of the slip velocity on the heat transfer is dominant at the low jump temperature (high value of β).

The effects of jump temperature on Nu at two different Kn is presented in Fig. 4.17. Decreasing the jump temperature has a positive effect on Nu and causes it to increase. This effect is more significant for high slip velocity, when Kn is high. The results show that the decreasing effect of jump temperature on the heat transfer is dominant at the high slip velocity values.

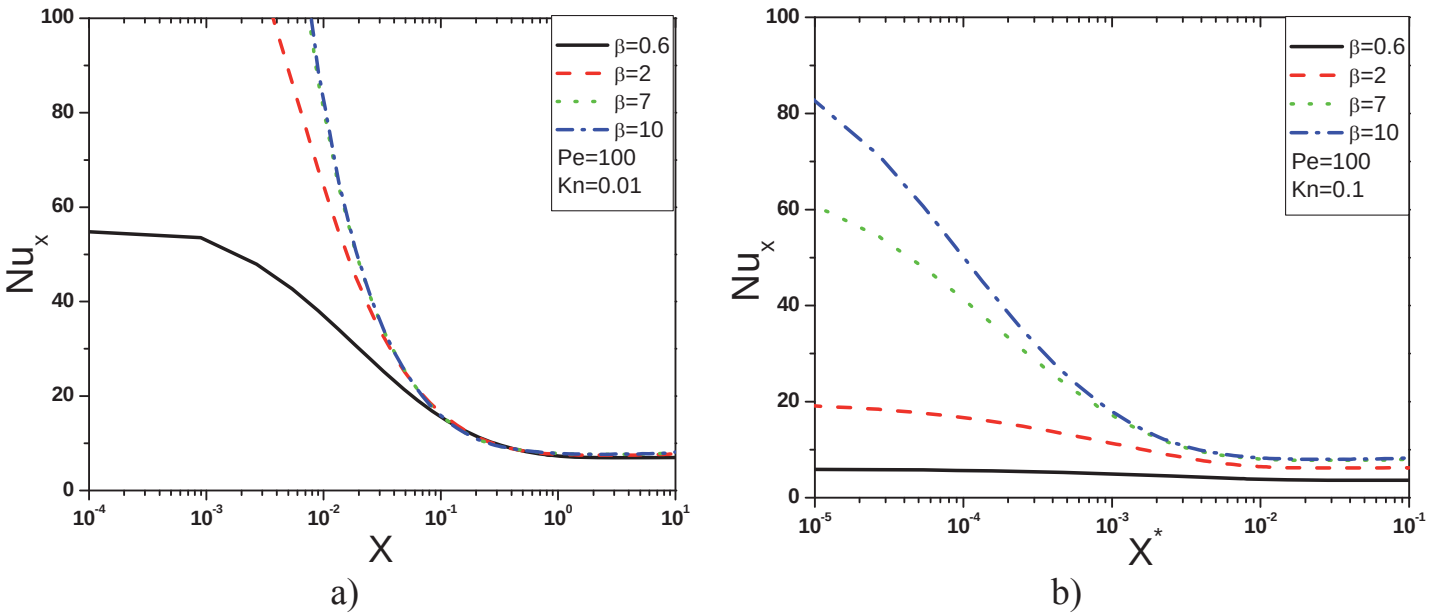

Fig. 4.17 Variation of the local Nusselt number with the jump temperature at a) Pe=100, Kn=0.01 , b) Pe=100, Kn=0.1.

4.8 Conclusions

Effects of rarefaction on the forced convection heat transfer of laminar, steady and incompressible fluid flows in straight microchannels with uniform heat flux were investigated using the Navier-Stokes and energy equations and using the slip velocity and the jump temperature boundary conditions at the wall. It was presented that increasing the Knudsen number decreases the maximum velocity while the velocity close to the wall increases. The results show that the velocity distribution in the slip flow regimes is flattened compared with the non-slip flow regimes.

The pressure profile changes linearly along the channel. The pressure reduces with increasing slip velocity. The slip velocity has a decreasing effect by more than 50% on the pressure drop for the case of Kn=0.1. The local friction coefficient decreases by increasing the slip velocity at any Reynolds number. In the case of slip flow, the Poiseuille number and the Nusselt number have finite values at the entrance of the channel, which are calculated by $f\,\mathrm{Re}(0) = \frac{2}{Kn}$ and $Nu(0) = \frac{\beta}{Kn}$, respectively. The Knudsen number has an increasing effect on the entrance length at any Re but this effect is more significant at high Re.

The combined effect of the slip velocity and the jump temperature could increase or decrease the Nusselt number based on their relative magnitude. Increasing effect of the slip velocity on the heat transfer is dominant for the low jump temperature (high value of β). The decreasing effect of jump temperature on the heat transfer is more dominant for the high slip velocity values.

Chapter 5

Curved Microchannels

In this Chapter, effects of the centrifugal force on the hydraulic and thermal behaviors of fluid slip flow in curved microchannels are investigated. The effects of rarefaction on laminar, steady state and incompressible forced convection fluid flow in curved microchannels with uniform heat flux are considered. Slip velocity and jump temperature boundary conditions at the wall are applied. The Navier-Stokes and energy equations are discretized, using the finite volume technique. The calculated results show good agreements with previous numerical data and analytical solutions [AKB10D].

5.1. Schematic of the Problem

The geometries of the two- and three-dimensionally considered problems are shown in Fig. 5.1 and Fig. 5.2, respectively. The computation domain is composed of a curved rectangular microchannel where the axial angle θ ranges from 0° to 180°, with the width of W and the curvature radius of r_0.

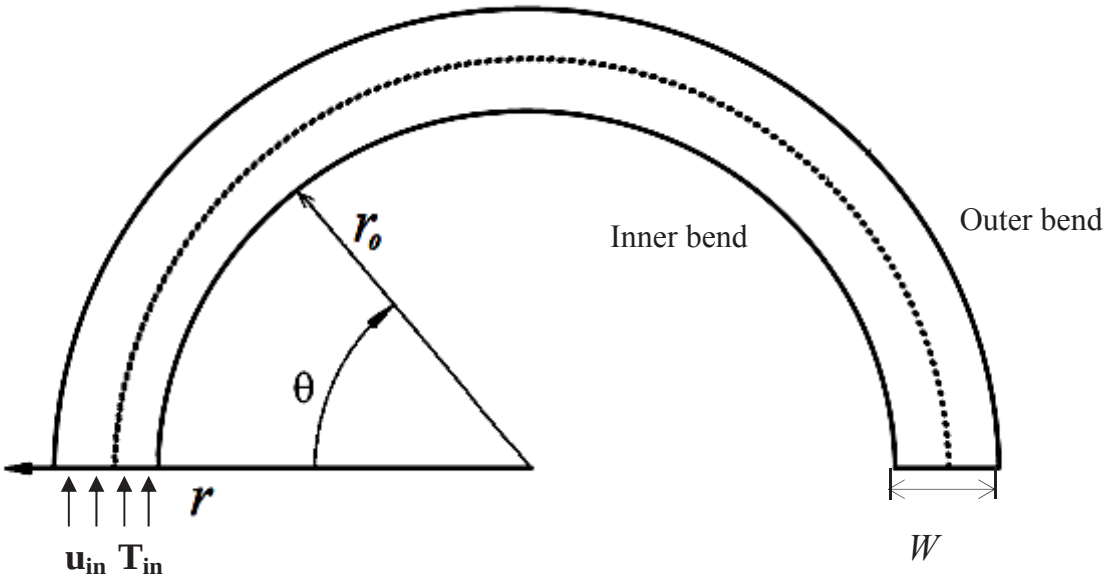

Fig. 5.1. Schematic diagram of a two dimension curved microchannel.

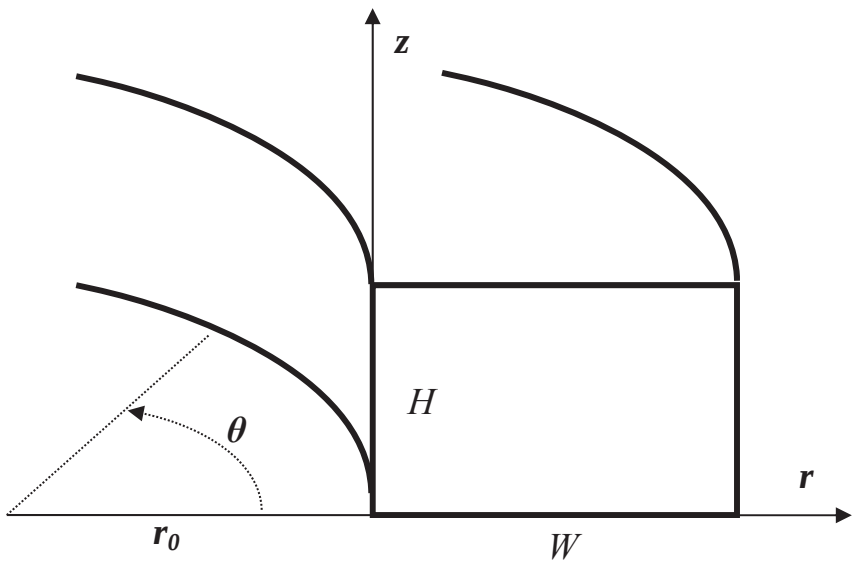

Fig. 5.2 Schematic diagram of a three-dimensional rectangular microchannel.

5.2 Fluid Flow and Heat Transfer Assumptions

In this study, the laminar forced convection fluid flow in curved rectangular microchannels are considered. The following assumptions are applied:

- The fluid flow is laminar, steady state and incompressible,
- The properties of fluid flow are assumed to be constant and homogenous,
- Dissipation and pressure work are neglected,
- There are no significant body forces (gravity force, magnetic force,…),
- The rarefaction effects set the slip velocity and the jump temperature at the fluid–wall interface.

5.3 Governing Equations

Working with the above assumptions, the steady state governing equations describing the fluid flow and the heat transfer in a three-dimensional rectangular curved microchannel in the cylindrical coordinate can be derived from Equations (3.1)-(3.4) as follows:

- continuity equation:

$$\frac{\partial u_r}{\partial r}+\frac{\partial u_\theta}{r\partial\theta}+\frac{\partial u_z}{\partial z}=0, \tag{5.1}$$

- momentum equation in r direction:

$$\rho\left(u_r\frac{\partial u_r}{\partial r}+\frac{u_\theta}{r}\frac{\partial u_r}{\partial\theta}+u_z\frac{\partial u_r}{\partial z}-\frac{u_\theta^2}{r}\right)=\mu\left[\frac{1}{r}\frac{\partial}{\partial r}\left(r\frac{\partial u_r}{\partial r}\right)+\frac{1}{r^2}\frac{\partial^2 u_r}{\partial\theta^2}+\frac{\partial^2 u_r}{\partial z^2}-\frac{u_r}{r^2}-\frac{2}{r^2}\frac{\partial u_\theta}{\partial\theta}\right]-\frac{\partial p}{\partial r}, \tag{5.2}$$

- momentum equation in θ direction:

$$\rho\left(u_r\frac{\partial u_\theta}{\partial r}+\frac{u_\theta}{r}\frac{\partial u_\theta}{\partial\theta}+u_z\frac{\partial u_\theta}{\partial z}+\frac{u_r u_\theta}{r}\right)=\mu\left[\frac{1}{r}\frac{\partial}{\partial r}\left(r\frac{\partial u_\theta}{\partial r}\right)+\frac{1}{r^2}\frac{\partial^2 u_\theta}{\partial\theta^2}+\frac{\partial^2 u_\theta}{\partial z^2}-\frac{u_\theta}{r^2}+\frac{2}{r^2}\frac{\partial u_r}{\partial\theta}\right]-\frac{\partial p}{\partial\theta}, \tag{5.3}$$

- momentum equation in z direction:

$$\rho\left(u_r\frac{\partial u_z}{\partial r}+\frac{u_\theta}{r}\frac{\partial u_z}{\partial \theta}+u_z\frac{\partial u_z}{\partial z}\right)=\mu\left[\frac{1}{r}\frac{\partial}{\partial r}\left(r\frac{\partial u_z}{\partial r}\right)+\frac{1}{r^2}\frac{\partial^2 u_z}{\partial \theta^2}+\frac{\partial^2 u_z}{\partial z^2}\right]-\frac{\partial p}{\partial z}, \tag{5.4}$$

- fluid energy equation:

$$\rho C_p\left(u_r\frac{\partial T}{\partial r}+\frac{u_\theta}{r}\frac{\partial T}{\partial \theta}+u_z\frac{\partial T}{\partial z}\right)=k\left(\frac{\partial^2 T}{\partial r^2}+\frac{1}{r^2}\frac{\partial^2 T}{\partial \theta^2}+\frac{\partial^2 T}{\partial z^2}\right), \tag{5.5}$$

where ρ is density, μ is dynamic viscosity, C_p is specific heat, k is thermal conductivity, T is temperature, p is pressure and u_r, u_θ, u_z are velocity components.

5.4 Rarefaction Implementation

The first order velocity slip and jump temperature condition for the cylindrical coordinate from (3.7) and (3.8) are given as:

$$u_\theta=\left(\frac{2-\sigma_u}{\sigma_u}\right)Kn\,D_h\left.\frac{\partial u_\theta}{\partial r}\right|_{wall}, \tag{5.6}$$

$$T-T_{wall}=\left(\frac{2-\sigma_T}{\sigma_T}\right)\left(\frac{2\gamma}{\gamma+1}\right)\frac{1}{\Pr}\left[Kn\,D_h\left(\left.\frac{\partial T}{\partial r}\right|_{wall}\right)\right]. \tag{5.7}$$

Values of the thermal and momentum accommodation coefficients (σ_u, σ_T) are near unity for most engineering applications and they are taken as unity in the present study (see Appendix B for details about thermal and accommodation factors).

After simplifying, the slip flow velocity and jump temperature boundary conditions are given by:

$$u_{\theta,N}-u_{\theta,wall}=Kn\,D_h\left.\frac{\partial u_\theta}{\partial r}\right|_{wall}, \tag{5.8}$$

$$T_N-T_{wall}=\frac{Kn\,D_h}{\beta}\left.\frac{\partial T}{\partial r}\right|_{wall}, \tag{5.9}$$

where

$$\beta = \Pr\left(\frac{\gamma+1}{2\gamma}\right). \tag{5.10}$$

With the following procedure, the slip velocity and the jump temperature boundary conditions are employed in the discretization equations. In order to simplify, a two-dimensional control volume close to the wall boundary is considered as it is shown in Fig. 5.3.

The slip velocity near the wall from (5.8) is given as:

$$u_{\theta,N} - u_{\theta,wall} = Kn\, D_h \left.\frac{\partial u_\theta}{\partial r}\right|_{wall}, \tag{5.11}$$

where $u_{\theta,wall}$ is equal to zero. By applying the first order approximation for the velocity gradient close to the wall we obtain:

$$\left.\frac{\partial u_\theta}{\partial r}\right|_{wall} = \frac{u_{\theta,P} - u_{\theta,N}}{\Delta r}. \tag{5.12}$$

Inserting (5.12) into (5.11) we obtain:

$$u_{\theta,N} - u_{\theta,wall} = Kn\, D_h \frac{u_{\theta,P} - u_{\theta,N}}{\Delta r} \tag{5.13}$$

and consequently

$$u_{\theta,N} - u_{\theta,P} = \frac{\left(u_{\theta,wall} - u_{\theta,P}\right)}{\left(1 + \frac{Kn\, D_h}{\Delta r}\right)}. \tag{5.14}$$

The discretized momentum equation for a control volume adjacent to the wall from Patankar [PAT80] was given as:

$$a_N\left(u_N - u_p\right) + a_S\left(u_S - u_p\right) + a_E\left(u_E - u_p\right) + a_W\left(u_W - u_p\right) + b = 0. \tag{5.15}$$

After replacing the term (u_N-u_P) in (5.15) by (5.14), it is written as:

$$\frac{\left(a_N\right)}{\left(1 + \frac{Kn\, D_h}{\Delta r}\right)}\left(u_{\theta,N} - u_{\theta,p}\right) + a_S\left(u_{\theta,S} - u_{\theta,p}\right) + a_E\left(u_{\theta,E} - u_{\theta,p}\right) + a_W\left(u_{\theta,W} - u_{\theta,p}\right) + b = 0. \tag{5.16}$$

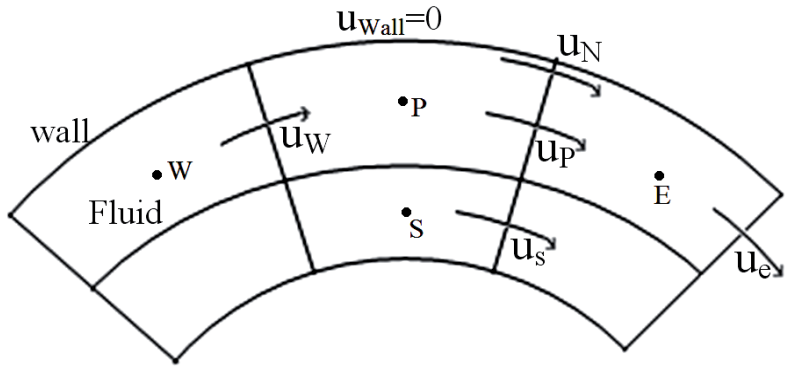

Fig. 5.3 Curved control volume close to the wall.

5.5. Boundary Conditions

The associated boundary conditions for solving the above set of nonlinear governing equations (5.1) to (5.5) are as follows:

- At the channel inlet ($\theta=0$); the fluid velocity and the temperature are assumed uniform and constant (u_{in} , T_{in}). Pressure at the inlet is calculated by the program.
- At the fluid-solid interface ($r=r_0$, $r= r_0+W$ and $0 \le \theta \le \pi$): The velocity in r direction is zero. The slip velocity of the fluid flow adjacent to the wall in θ direction is proportional to the normal velocity gradient at the wall as shown in (5.8). The jump temperature of the fluid flow adjacent to the wall is proportional to the normal temperature gradient at the fluid–wall interface (5.9). An uniform heat flux ($q'' = -k\left.\frac{\partial T}{\partial r}\right|_{wall}$) is applied at the wall.
- At the channel outlet ($\theta=\pi$) the diffusion flux in the direction normal to the exit is assumed to be zero for the velocity and the temperature while a zero pressure is assigned at the flow exit.

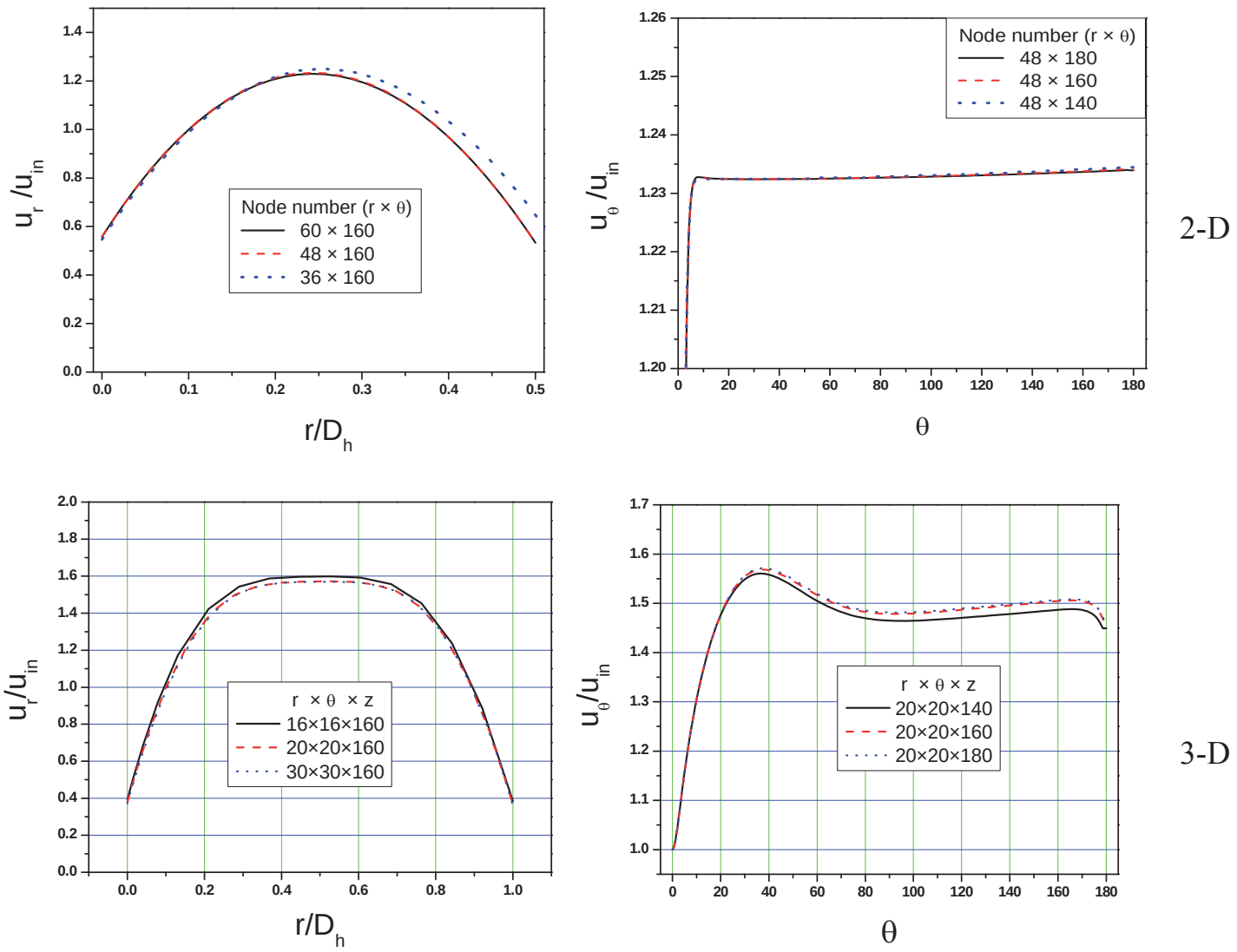

Fig. 5.4 grid independent test for various directions.

5.6 Numerical Methods

The sets of coupled non-linear differential equations (5.1) to (5.5) are discretized, using the Finite Volume technique. The Power law scheme is used for the convective and diffusive terms while the SIMPLER procedure is used to couple velocity and pressure (as described in Chapter 3). The slip velocity and the jump temperature boundary conditions are discretized and employed in the discretization equations.

A structured non uniform grid distribution is used for the computational domain. It is finer near the microchannel entrance and near the wall, where the velocity and the temperature gradients are high.

Several different grid distributions are tested to ensure that the calculated results are grid independent. More than 48 nodes in r direction and 160 nodes in θ direction will not change the non-dimensional velocity significantly, as shown in Fig. 5.4. The grid for the case of three-dimensional flow is 20×20 nodes in any cross section and 160 nodes in axial direction. The selected grid for the present calculations consisted of 60×160 and 20×20×160 nodes for two-and three-dimensional, respectively. The solution is assumed converged when $\left|\frac{\left(\phi^{n+1}-\phi^{n}\right)}{\phi^{n+1}}\right| \leq 10^{-6}$ is satisfied for all independent variables.

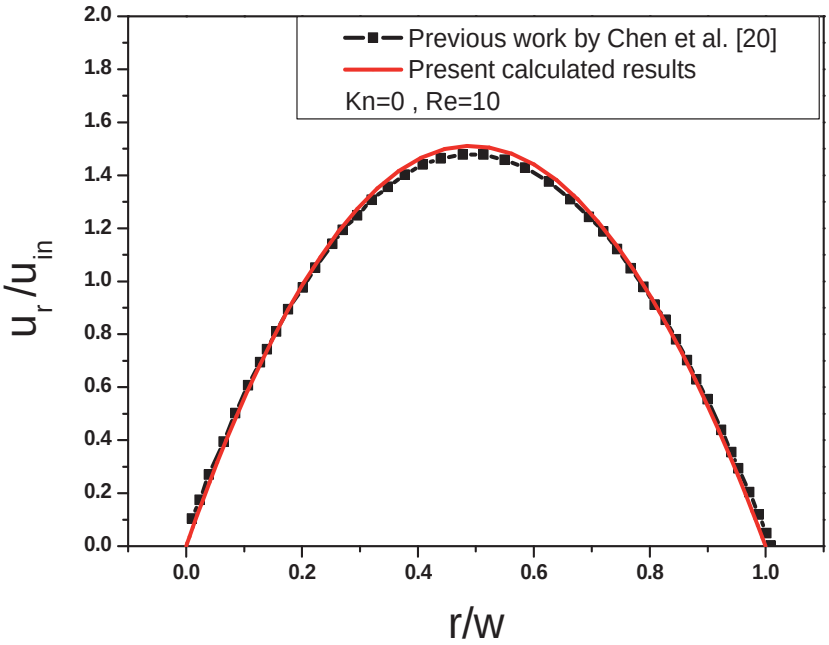

Fig. 5.5 Comparison of the fully developed velocity profile with results of [CHE10]

5.7 Validations

In order to demonstrate the validity and precision of the model assumptions and the numerical analysis, calculated velocity at developed region is compared with the corresponding numerical results carried out by Chen et al. [CHE10] for

water at Re=10 and Kn=0 in the curved microchannels as shown in Fig. 5.5. The local Poiseuille number is compared with the corresponding values from the work of Chen et al. [CHE10] at Re=50, Kn=0 in a curved microchannel with $\frac{r_0}{r_0 + W} = 0.9$ as presented in Fig. 5.6.

It is observed from Fig. 5.5 and Fig. 5.6 that the present computation has an excellent agreements with the published results.

Table 5.1. Comparison of the Poiseuille number at fully developed region with results of [REN06].

Kn	$(f\,\mathrm{Re})_{fd}$					
	Analytical solution	Previous numerical results	Present calculation			
			Re=0.1	Re=10	Re=100	Re=1000
0	24.00	23.87	24.72	24.77	24.89	27.62
0.01	21.43	21.33	21.96	22.04	22.46	23.62
0.05	15.00	14.95	15.33	15.37	15.66	16.11
0.1	10.91	10.88	11.13	11.14	11.34	11.66

In Table 5.1 fully developed values of the Poiseuille number is compared with available numerical and analytical solutions at different Re and Kn. The Renksizbulut et al. [REN06] have calculated the Poiseuille number for two parallel planes, which vary with Kn according to $f\,\mathrm{Re}_{fd} = \frac{24}{(1+12Kn)}$. The calculated Poiseuille numbers in Table 5.1 show a good agreement with numerical results by Renksizbulut et al. [REN06] at low Reynolds numbers. The centrifugal force increases with increasing velocity in the curved tube. The centrifugal force does not have any effect in the straight tube. Due to the increase of centrifugal force at high Reynolds number, differences between the calculated results and published results increase.

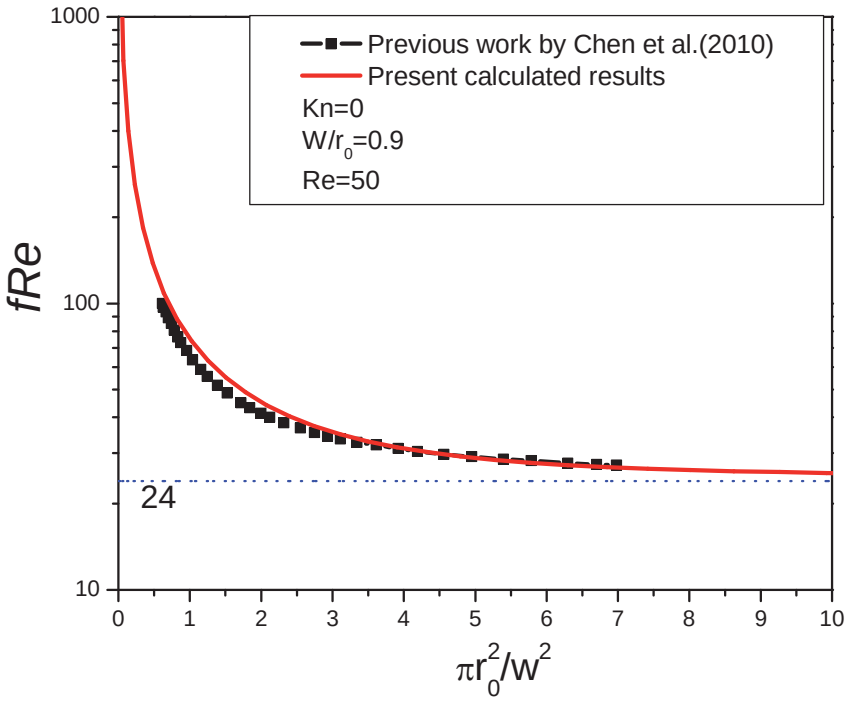

Fig. 5.6 Comparison of the local Poiseuille number with results of [CHE10] for *Kn*=0.

5.8 Results and Discussion

Numerical simulations are done on a wide range of Re between 0.01 to 1000 for different values of Knudsen number and Prandtl number. Because of similar behaviors and lack of space the results presented here are for Re=0.01, 10, 100 and 1000 with four different values of Knudsen number (0, 0.01, 0.05, 0.1). Two different values of Prandtl number (0.7 and 7) with different values of slip velocity and jump temperature ($0 \leq Kn \leq 0.1$ and $0.6 \leq \beta \leq 10$) are considered. Variation of the velocity profiles, pressure, the friction factor and the Nusselt number with the slip velocity, the jump temperature and the curvature effects are presented and discussed.

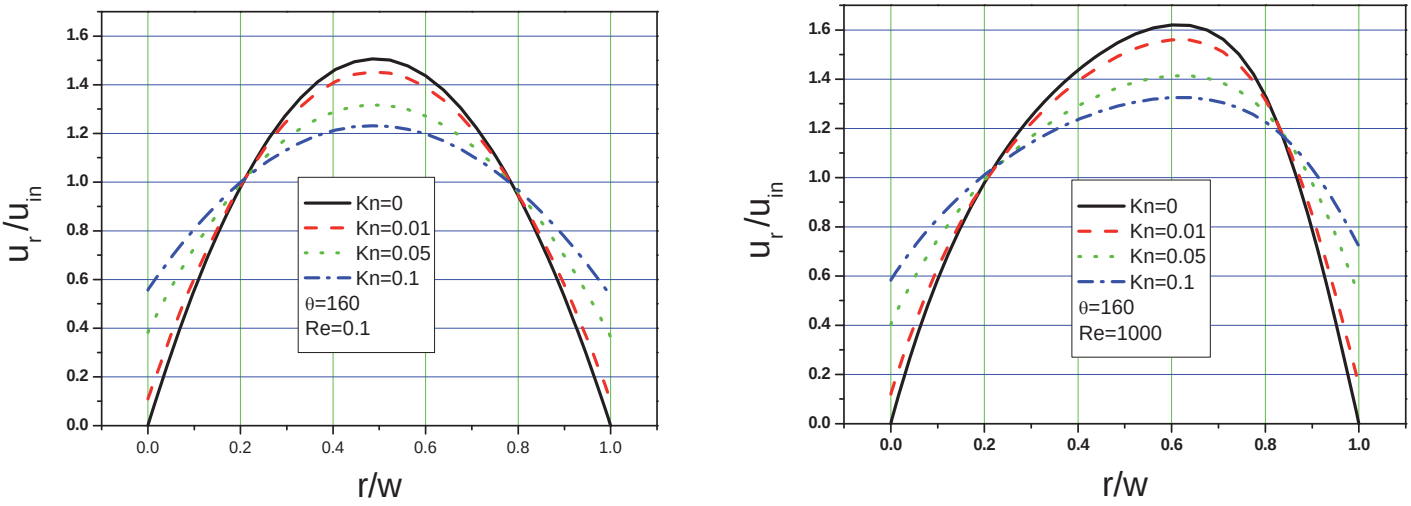

a) b)

Fig. 5.7 Variation of the fully developed velocity profile in the curved microchannels with the Knudsen number at a) Re=0.1 and b) Re=1000.

5.8.1 Velocity field

Variation of the non-dimensional velocity profiles with the Knudsen number at fully developed region for two different values of Re are presented in Fig. 5.7. It is shown that at any Re, the slip velocity causes an increase in the flow velocity near the wall while the maximum flow velocity at the center line reduces. It is illustrated that the flow velocity distribution in microchannels (slip flow regimes) is flattened compared to continuum flows (non-slip flow regimes). The centrifugal force does not affect the flow velocity profiles for the case of Re=0.1, however it shifts the flow velocity profile to the outer bend for the case of Re=1000.

Fig. 5.8 shows the variation of non-dimensional flow velocity with the Reynolds number for Kn=0.01. It is clear from Fig. 5.8a that the centrifugal force does not have any significant effect on the velocity profile with increasing Re up to 100. But effect of curvature causes the velocity near the outer bend to increase for the case of Re=1000.

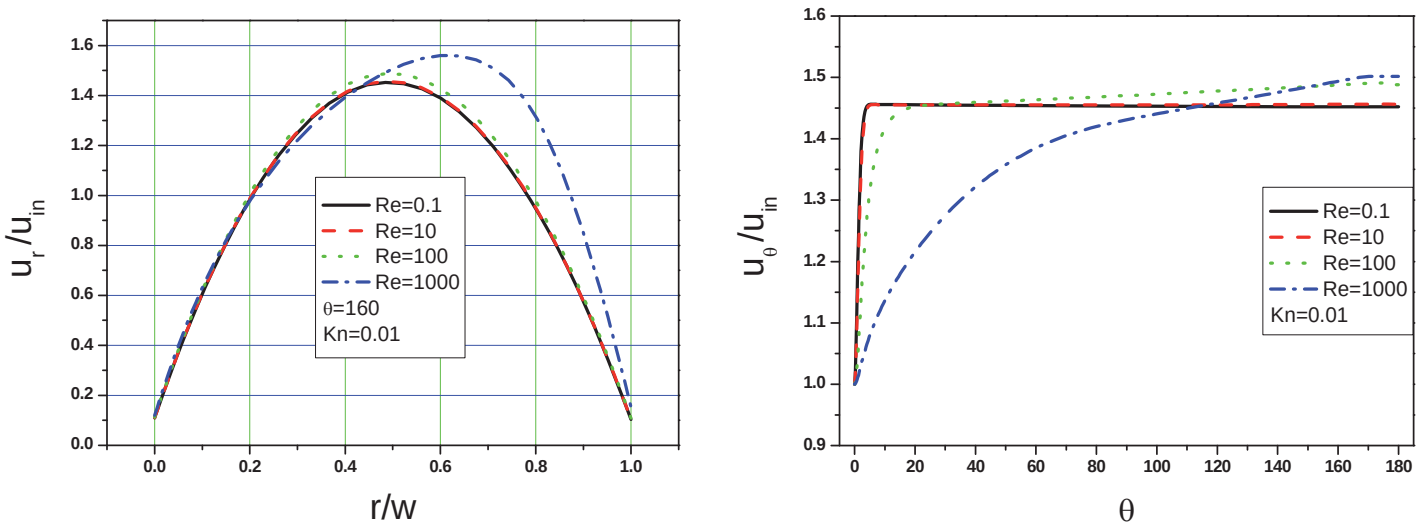

a) b)

Fig. 5.8 The non-dimensional velocity profiles in the curved microchannel for different values of the Reynolds number.

The non-dimensional velocity profiles at the middle line along the channel length at different Re are shown in Fig. 5.8 b. The Reynolds number has a reducing effect on the non-dimensional velocity at the entrance length and it postpones the fully developed condition. It causes the fully developed velocity at the middle line to increase. It is remarkable that the flow velocity becomes fully developed at $\theta<10^0$ when Re<100 but the fully developed condition does not happen for the case of Re=1000.

Fig. 5.9 shows the non-dimensional velocity at the middle line along the channel length for different Kn. The flow velocity at the center line decreases by increasing the slip velocity (increasing Kn) at any Re. The fully developed non-dimensional velocity at the middle line decreases about 25% by increasing Kn to 0.1.

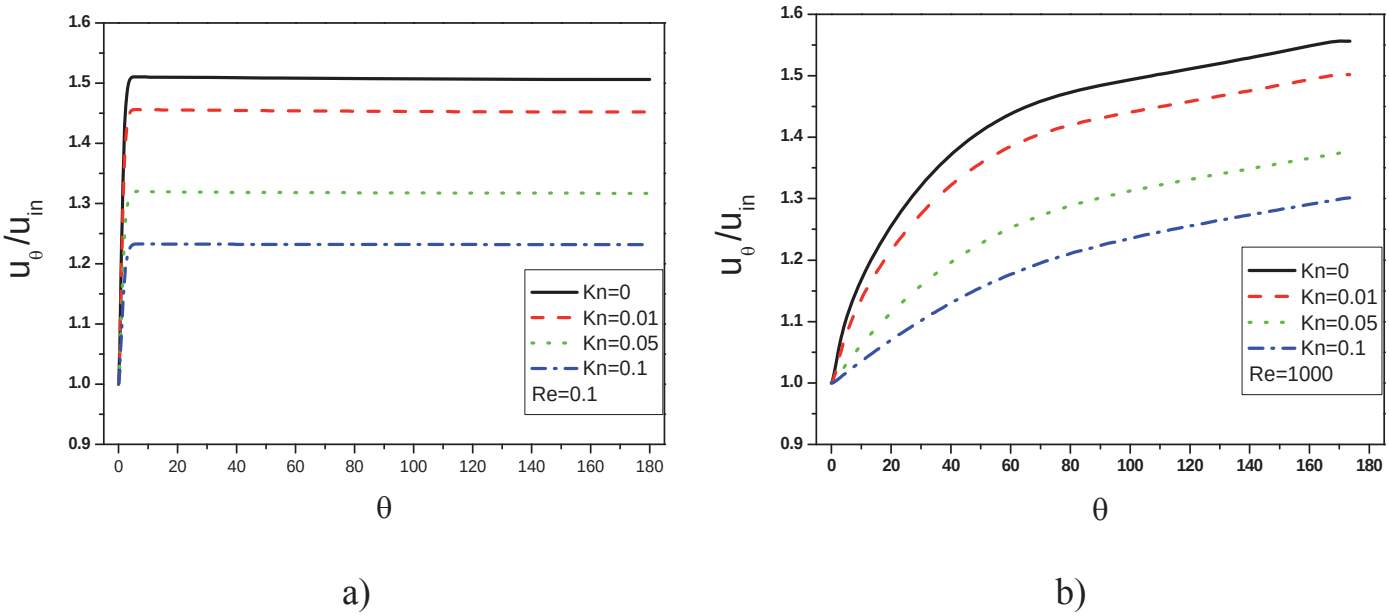

a) b)

Fig. 5.9 Variation of the non-dimensional velocity with Kn along the channel at a)Re=0.1 and b)Re=1000.

5.8.2 Pressure

Variation of the non-dimensional pressure profile with Kn at two different Re is shown in Fig. 5.10. The local pressure decreases linearly along the microchannel. It means that after passing the entrance length, pressure is not a function of r direction. It behaves like the non-slip flow regime, which varies linearly along the curved microchannel. Slip velocity has a decreasing effect on the non-dimensional local pressure at any Reynolds number. There is a smaller pressure drop for slip flows in comparison with the continuum flows (Kn=0).

The variation of pressure drop with the Knudsen number and the Reynolds number are presented in Fig. 5.11. The slip velocity allows the fluid near the wall to flow, therefore a smaller pressure drop takes place. It is also shown in Fig. 5.11 that increasing Kn has a decreasing effect about 50% on the pressure drop by increasing Kn to 0.1. It is depicted in Fig. 5.11 that the Reynolds number has an increasing effect on the pressure drop.

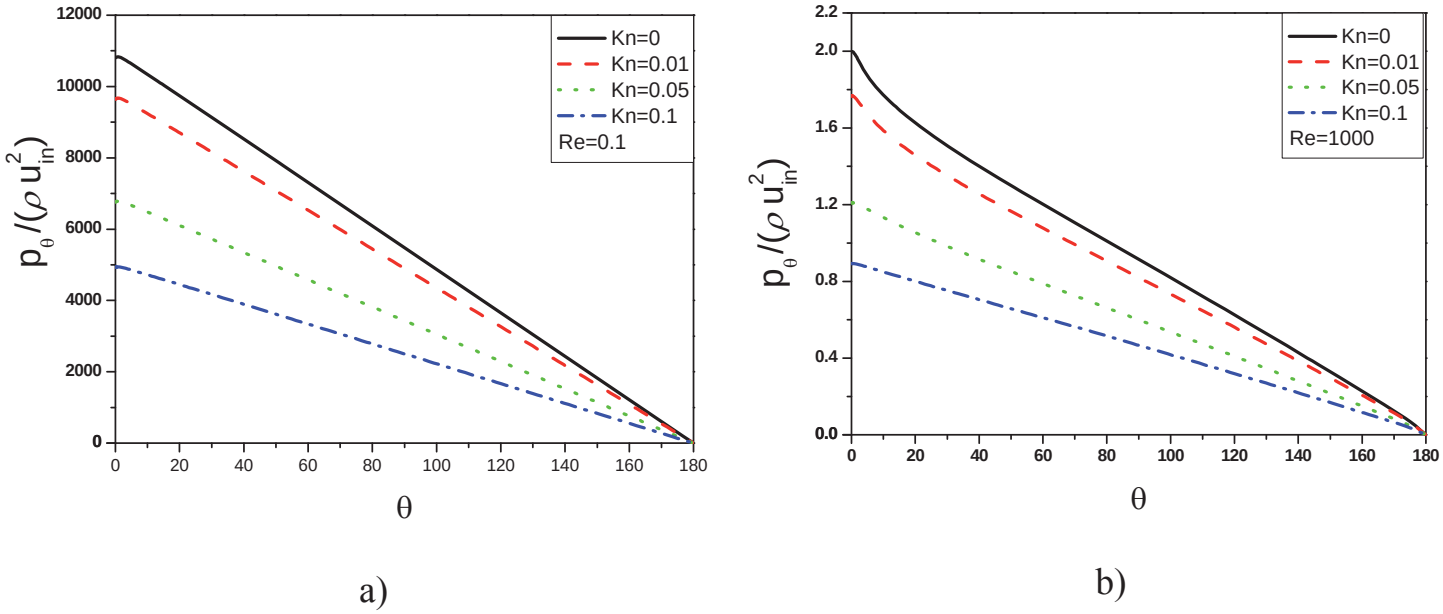

Fig. 5.10 Variation of the pressure with Kn along the curved microchannel at a)Re=0.1 and b)Re=1000.

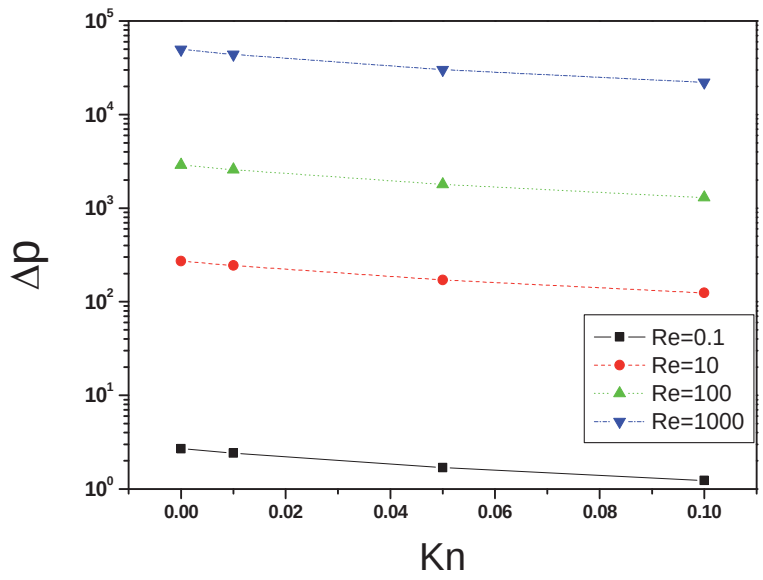

Fig. 5.11 The pressure drop in a curved microchannel at different Re and Kn.

5.8.3 Skin friction factor

The Fanning friction coefficient is given by:

$$f = \frac{\tau_{wall}}{\frac{1}{2}\rho u_{in}^2}, \tag{5.17}$$

where

$$\tau_{wall} = \mu \left.\frac{\partial u_\theta}{\partial r}\right|_{wall}. \tag{5.18}$$

Therefore, the Poiseuille number (fRe) is obtained by

$$f\,\mathrm{Re} = 2\frac{\left.\frac{\partial u_\theta}{\partial r}\right|_{wall}}{\bar{u}_{in}} D_h\ . \tag{5.19}$$

Inserting the term $\left.\frac{\partial u_\theta}{\partial r}\right|_{wall}$ from (5.8) into (5.19); the friction coefficient is expressed as:

$$f\,\mathrm{Re} = \frac{2}{KnD_h}\left(u_N - u_{wall}\right). \tag{5.20}$$

The variation of the Poiseuille number with Kn for different Re is illustrated in Fig. 5.12. It shows that in the entrance region, the slip velocity results in a large reduction of the friction coefficient. For the non-slip flow, $\theta = 0^\circ$ is a singularity plane resulting in an infinitely large wall shear. The friction coefficient for the slip flows at the channel inlet is finite as seen in Fig. 5.12. It can be easily shown that if $\theta \to 0^\circ$ *then* $f\,\mathrm{Re}_0 \to \frac{2}{Kn}$. The friction coefficient starts with a value of nearly $\frac{2}{Kn}$ for the case of slip flow while its value is infinite for the non-slip flow (Kn=0).

In the slip flow regimes, the layer of fluid close to the wall flows. Therefore, an increasing in Kn causes to reduce the local friction factor. The Reynolds number has an increasing effect on the Poiseuille number, as shown in Fig. 5.12 c).

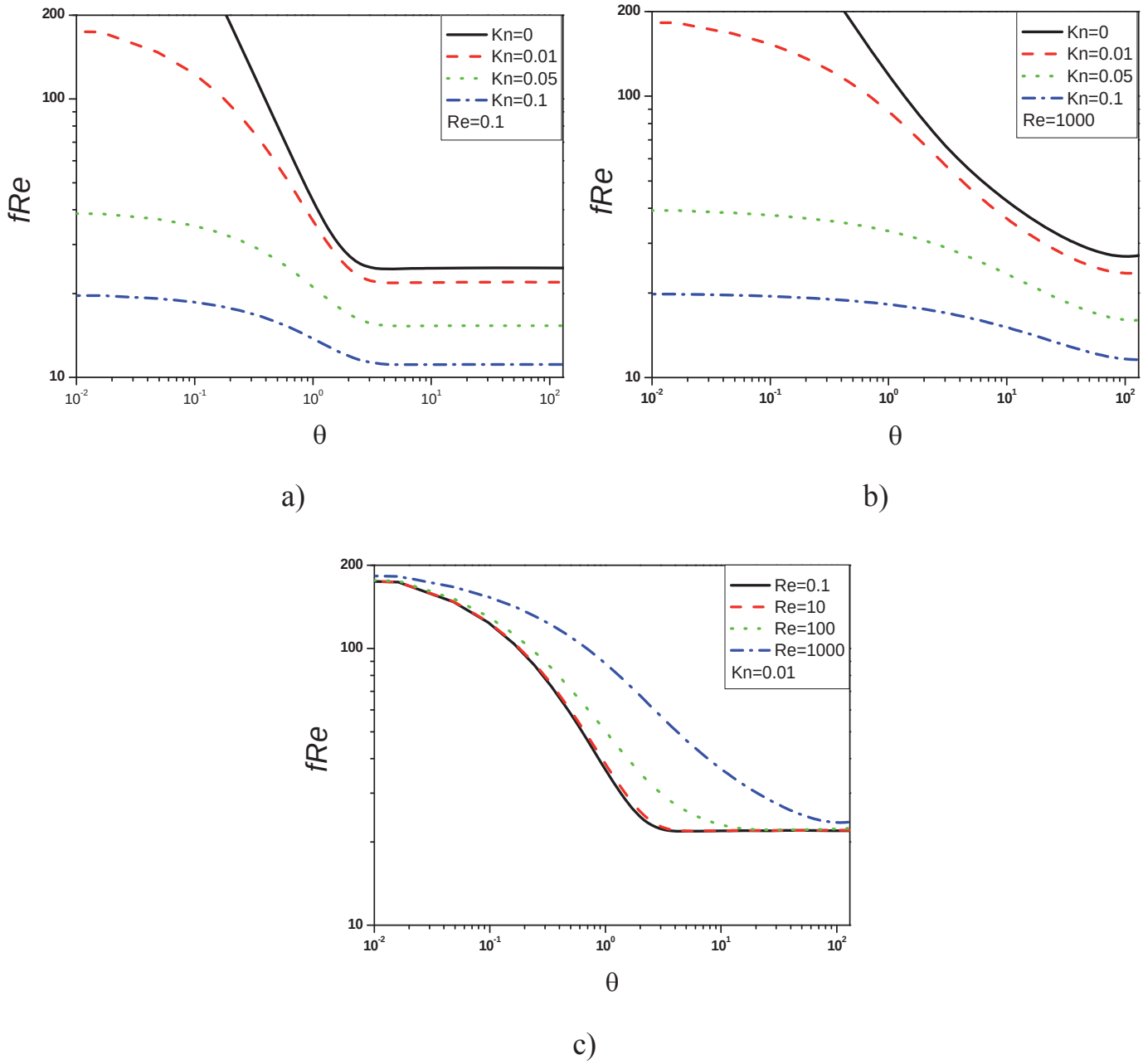

Fig. 5.12 Variation of the Poiseuille number with Kn and Re.

5.8.4 Nusselt number

The Nusselt number (*Nu*) is obtained by:

$$Nu = \frac{h\, D_h}{k}, \tag{5.21}$$

where

$$h = \frac{q''}{\left(T_{wall} - T_b\right)}. \tag{5.22}$$

By inserting (5.22) into (5.21), the Nusselt number for the uniform heat flux is calculated from:

$$Nu = \frac{q''\, D_h}{k\left(T_{wall} - T_b\right)}. \tag{5.23}$$

In the non-slip flow, the local Nusselt number starts from an infinite value and drops to get the fully developed value. Due to the presence of slip velocity and jump temperature in the slip flow, Nu starts with a finite value. Similar to the skin friction factor, in the case of non-slip flow, $\theta = 0^\circ$ is a singularity plane for the Nusselt number. Nu has a finite value for the case of slip flow regime at $\theta = 0^\circ$. By applying $q'' = -k\left.\frac{\partial T}{\partial r}\right|_{wall}$ and $\left.\frac{\partial T}{\partial r}\right|_{wall}$ from (5.9) into (5.23), the Nusselt number is expressed as:

$$Nu_\theta = \frac{\frac{\beta}{Kn}\left(T_{wall} - T_N\right)}{T_{wall} - T_b}. \tag{5.24}$$

Therefore at the channel inlet where $\theta = 0^\circ$, if $\theta \to 0^\circ$ *then* $Nu(0) \to \frac{\beta}{Kn}$. Variation of the local Nusselt number along the curved microchannel with slip velocity at two different values of Prandtl number ($\beta = \Pr\left(\frac{\gamma+1}{2\gamma}\right)$.) is shown in Fig. 5.13. In the slip flow, the presence of slip velocity and jump temperature significantly affects the local Nusselt number. The slip velocity increases the advection near the wall, therefore the heat transfer increases. Jump temperature increases the thermal resistance at the wall-fluid interface causing a decrease in the heat transfer. The combined effect of the slip velocity and the jump

temperature can increase or decrease heat transfer depending on their relative magnitude.

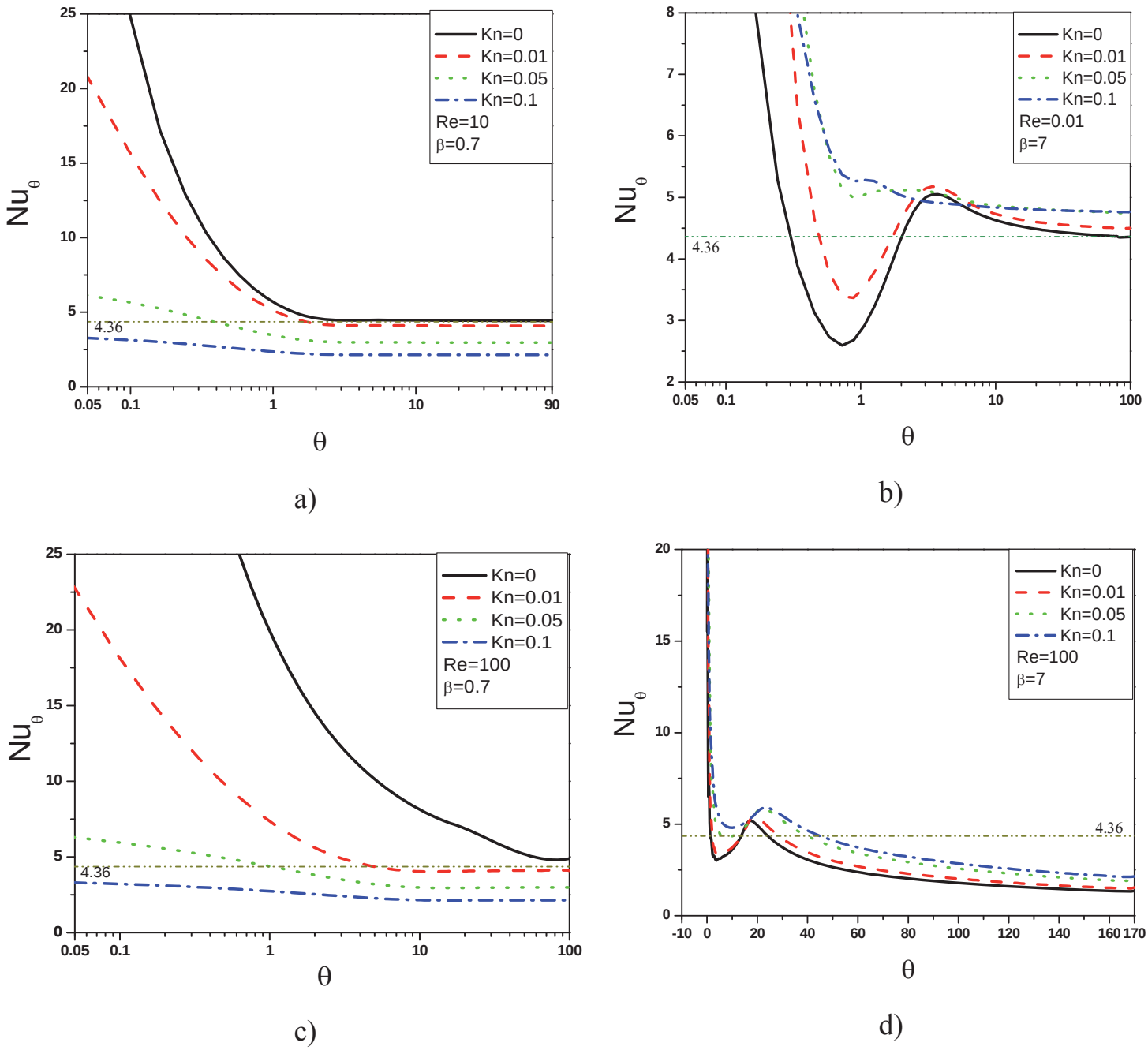

Fig. 5.13 The local Nusselt number for different Kn at a) Re=10, *β*=0.7, b) Re=0.01, *β*=7, c) Re=100, *β*=0.7, and d) Re=100, *β*=7.

It is shown in the Fig. 5.13 that although both the slip velocity and the jump temperature increase with increasing Kn, it results in a decrease in Nu_θ in the cases of high jump temperature (β=0.7). But the local Nusselt number increases with increasing Kn for the case of low jump temperature (β=7). It is evident that the increasing effect of slip velocity on heat transfer is dominant for low jump temperature (high value of β) at any Re as illustrated in Fig. 5.13 a) and Fig. 5.13 c). The reduction effect of jump temperature on the heat transfer dominates at low values of Prandtl number (β) and at any Re as shown in Fig. 5.13 b) and Fig. 5.13 d).

The Nusselt number is 4.36 at fully developed flow in straight channels. It is remarkable that the fully developed Nusselt number in the curved microchannel is near 4.36 when Re is low, while it is less than 4.36 for the case of Re=100. It shows that the centrifugal force in the curved micro channels does not have a significant effect on heat transfer. Therefore, the curved microchannels can be simulated as straight microchannels.

5.9 Conclusions

The effect of centrifugal force on hydraulics and thermal behavior of slip fluid flow in the curved microchannels is investigated. Effects of rarefaction on the forced convection heat transfer of laminar, steady and incompressible fluid flows in curved microchannels with uniform heat flux are considered. The Navier-Stokes and energy equations are applied. The slip velocity and the jump temperature boundary conditions are used at the wall. It is presented that increasing the Knudsen number decreases the maximum flow velocity while the flow velocity close to the wall increases. The results show that the flow velocity distribution in the slip flow regimes is flattened compared with the non-slip flow regimes.

Pressure changes linearly along the microchannels. Pressure reduces with increasing the slip velocity. The slip velocity has a decreasing effect by more

than 50% on the pressure drop for the case of Kn=0.1. The local friction coefficient decreases when the slip velocity increases.

In the case of slip flow, the Poiseuille number and the Nusselt number have finite values at the channel entrance with $f\,\mathrm{Re}(0)=\frac{2}{Kn}$ and $Nu(0)=\frac{\beta}{Kn}$. The Knudsen number has an increasing effect on the entrance length at any Re but this effect is more significant at high Re.

The combined effect of the slip velocity and the jump temperature might increase or decrease the Nusselt number based on their relative magnitude. The increasing effect of the slip velocity on heat transfer is dominant for low jump temperature (high value of β). The decreasing effect of the jump temperature on the heat transfer is more dominant for high slip velocity values.

Chapter 6

Analytical Solution of the Fully Developed Slip Flow

The microfluidic systems are composed of straight and curved microchannels. A good understanding of fluid flow in a microfluidic system can be obtained when one considers the results of straight and curved channels together.

A very fast computing of fluid and temperature fields in microchannels is one of the purposes of this work. It is known that the iterative methods need a lot of time to give the results. Therefore, from the two important results of the previous chapters, the use of analytical solution for simulation of a microfluidic system is proposed.

The first result is from Chapter 4, where Fig. 4.11 shows that the entrance length in the straight microchannels is very small in comparison with the whole length when Re is less than 100. Consequently, the entrance length, which is a very small part of a microfluidic system, can be neglected.

The second important result is from Chapter 5, where Fig. 5.8a illustrates that the curvature effects are not significant when Re is less than 100. It is well known that, the Reynolds number of most fluid flow in microchannels is less than 100.

The entrance length and the curvature effects can be neglected when Re is less than 100. Therefore, curved parts of microchannel could be considered as

straight part. By that, large microfluidic systems, that contain a lot of straight and curved microchannels, can be simulated by considering a very long straight microchannel. They can be modeled as a totally fully developed region.

In this chapter the fully developed Navier-Stokes equations are obtained and the analytical solution and the results for two- and three-dimensional straight microchannels are presented.

6.1 Two-dimensional Microchannels

A very large two-dimensional microfluidic system with the length of L and the width of W is considered as shown in Fig. 6.1. The length is much longer than the width of the channel ($W << L$).

The fluid flow is laminar, steady state and incompressible with constant properties while dissipation, pressure work and body forces are neglected. The rarefaction effects set the slip velocity and the jump temperature at the fluid–wall interface. Therefore, the two-dimensional steady state governing equations describing the fluid flow in a long straight microchannel in the Cartesian coordinate is presented from Equation (3.2) as follows:

- continuity equation:

$$\frac{\partial u}{\partial x}+\frac{\partial v}{\partial y}=0, \tag{6.1}$$

- Navier-Stokes equations in Cartesian coordinates:

in x direction $$\rho\left(u\frac{\partial u}{\partial x}+v\frac{\partial u}{\partial y}\right)=-\frac{\partial p}{\partial x}+\mu\left(\frac{\partial^2 u}{\partial x^2}+\frac{\partial^2 u}{\partial y^2}\right), \tag{6.2}$$

in y direction $$\rho\left(u\frac{\partial v}{\partial x}+v\frac{\partial v}{\partial y}\right)=-\frac{\partial p}{\partial y}+\mu\left(\frac{\partial^2 v}{\partial x^2}+\frac{\partial^2 v}{\partial y^2}\right). \tag{6.3}$$

The fully developed region is defined with the following conditions:

a) $v=0$, where v is the velocity in y direction and

b) u is a function of y (from (6.4)), where u is the velocity in x direction.

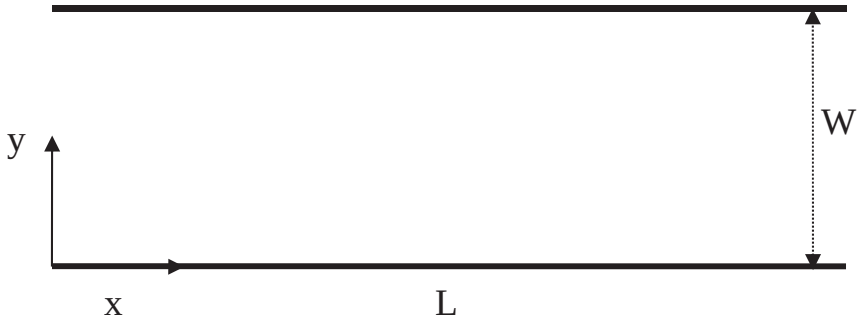

Fig. 6.1 Schematic of a two-dimensional large microchannel.

From condition a) and the continuity equation (6.1), it is obtained

$$\frac{\partial u}{\partial x} = 0 \text{ , therefore } \frac{\partial^2 u}{\partial x^2} = 0. \tag{6.4}$$

From (6.3) and condition a) we have $\frac{\partial v}{\partial x} = \frac{\partial v}{\partial y} = \frac{\partial^2 v}{\partial x^2} = \frac{\partial^2 v}{\partial y^2} = 0$,

then (6.3) results in

$$\frac{\partial p}{\partial y} = 0. \tag{6.5}$$

This means that the pressure is only a function of x.

From (6.2), because of the condition a) we have: $v\frac{\partial u}{\partial y} = 0$, and by inserting (6.4) into (6.2), it is obtained

$$\mu \frac{\partial^2 u}{\partial y^2} = \frac{dp}{dx} \tag{6.6}$$

(6.6) is the two dimensional governing equation of the fluid flow at the fully developed region. It is applied with the following boundary conditions for the slip flow in microchannels:

$$\left.\frac{\partial u}{\partial y}\right|_{y=W/2} = 0 \quad ,$$
$$u\big|_{y=0,W} - u_w = Kn\, 2h \left.\frac{\partial u}{\partial y}\right|_{y=0,W} \quad , \tag{6.7}$$

where $u_w=0$.

Integrating Equation (6.6) twice and applying the boundary conditions (6.7) results in a non-dimensional velocity profile in two dimensions as following:

$$\frac{u(y/h)}{u_{in}} = \frac{u_s}{u_{in}} + 6\left(1-\frac{u_s}{u_{in}}\right)\left(\frac{y}{h}-\frac{y^2}{h^2}\right),$$
$$\frac{u_s}{u_{in}} = 1-\frac{1}{1+12Kn}. \tag{6.8}$$

6.2 Three-dimensional Microchannels

A very long three-dimensional microchannel with the length of L, the width of W and the height of H is considered as shown in Fig. 6.2. The length is much longer than the width and height of the channel ($W << L, H$).

The fluid flow is laminar, steady state and incompressible with constant properties while dissipation, pressure work and body forces are neglected. The rarefaction effects set the slip velocity and the jump temperature at the fluid–wall interface. Therefore, the three-dimensional steady state governing equations describing the fluid flow in a long straight microchannel in the Cartesian coordinate can be presented from Equation (3.2) as follows:

- continuity equation:

$$\frac{\partial u}{\partial x}+\frac{\partial v}{\partial y}+\frac{\partial w}{\partial z}=0, \tag{6.9}$$

- Navier-Stokes equations in Cartesian coordinates :

in x direction $$\rho\left(u\frac{\partial u}{\partial x}+v\frac{\partial u}{\partial y}+w\frac{\partial u}{\partial z}\right)=-\frac{\partial p}{\partial x}+\mu\left(\frac{\partial^2 u}{\partial x^2}+\frac{\partial^2 u}{\partial y^2}+\frac{\partial^2 u}{\partial z^2}\right), \tag{6.10}$$

in y direction $$\rho\left(u\frac{\partial v}{\partial x}+v\frac{\partial v}{\partial y}+w\frac{\partial v}{\partial z}\right)=-\frac{\partial p}{\partial y}+\mu\left(\frac{\partial^2 v}{\partial x^2}+\frac{\partial^2 v}{\partial y^2}+\frac{\partial^2 v}{\partial z^2}\right), \tag{6.11}$$

in z direction $$\rho\left(u\frac{\partial w}{\partial x}+v\frac{\partial w}{\partial y}+w\frac{\partial w}{\partial z}\right)=-\frac{\partial p}{\partial z}+\mu\left(\frac{\partial^2 w}{\partial x^2}+\frac{\partial^2 w}{\partial y^2}+\frac{\partial^2 w}{\partial z^2}\right). \tag{6.12}$$

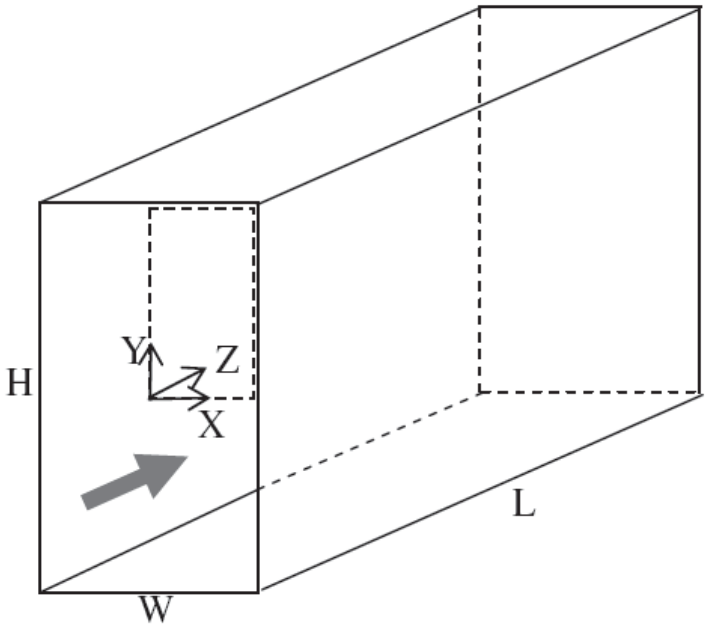

Fig. 6.2 Schematic of a three-dimensional long microchannel.

The fully developed region is defined as:

a) *v=u=0*, where *v* is the velocity in *y* direction and *u* is velocity in *x* direction and

b) *w* is function of x and y (from (6.13a) and (6.13b)), where *w* is the velocity in *z* direction

From condition a) and from the continuity equation (6.9), it is obtained

$$\frac{\partial w}{\partial z} = 0, \tag{6.13a}$$

therefore

$$\frac{\partial^2 w}{\partial z^2} = 0. \tag{6.13b}$$

From (6.10), (6.11) and condition a) we have $\frac{\partial u}{\partial x} = \frac{\partial u}{\partial y} = \frac{\partial u}{\partial z} = \frac{\partial^2 u}{\partial x^2} = \frac{\partial^2 u}{\partial y^2} = \frac{\partial^2 u}{\partial z^2} = 0$ and $\frac{\partial v}{\partial x} = \frac{\partial v}{\partial y} = \frac{\partial v}{\partial z} = \frac{\partial^2 v}{\partial x^2} = \frac{\partial^2 v}{\partial y^2} = \frac{\partial^2 v}{\partial z^2} = 0$, then (6.10) and (6.11) result in

$$\frac{\partial p}{\partial x} = 0,$$
$$\frac{\partial p}{\partial y} = 0. \tag{6.14}$$

This means that the pressure is only a function of z.

In (6.12) because of condition a) we have $v\frac{\partial w}{\partial y} = u\frac{\partial w}{\partial x} = 0$, and by inserting (6.13) in (6.12) it is obtained:

$$\mu\left(\frac{\partial^2 w}{\partial x^2} + \frac{\partial^2 w}{\partial y^2}\right) = \frac{dp}{dz}. \tag{6.15}$$

(6.15) is the three dimensional governing equation of fluid flow at fully developed region. It is applied with the following boundary conditions for the slip flow in microchannels:

$$\left.\frac{\partial w}{\partial y}\right|_{y=0} = 0,$$
$$\left.\frac{\partial w}{\partial x}\right|_{x=0} = 0,$$
$$w\Big|_{y=\frac{H}{2},-\frac{H}{2}} - w_{wall} = Kn\, D_h \left.\frac{\partial w}{\partial y}\right|_{y=\frac{H}{2},-\frac{H}{2}}, \tag{6.16}$$
$$w\Big|_{x=\frac{W}{2},-\frac{W}{2}} - w_{wall} = Kn\, D_h \left.\frac{\partial w}{\partial x}\right|_{y=\frac{W}{2},-\frac{W}{2}},$$

where $w_{wall}=0$.

Equation (6.15) with the boundary conditions (6.16) can be solved with the following method as describe by Tunc and Bayazitoglu [TUN02].

The governing equation and the boundary conditions are made non-dimensional by the following parameters:

$$w^* = \frac{w}{\overline{w}}, \quad x^* = \frac{x}{W}, \quad y^* = \frac{y}{W}. \tag{6.17}$$

Then the (6.15) becomes

$$\frac{\partial^2 w^*}{\partial x^{*2}} + \frac{\partial^2 w^*}{\partial y^{*2}} = P^*, \tag{6.18}$$

with the boundary conditions (6.16)

$$w^* = \beta_s \quad \text{at } x^*=0,\ x^*=1 \text{ and } y^*=0,\ y^*=\gamma, \tag{6.19}$$

where

$$P^* = \frac{W^2}{\mu w_m}\frac{dP}{dz}, \quad \beta_s = \frac{w_s}{w_m} \ and\ \gamma = \frac{H}{W}.$$

γ is the aspect ratio and β_s is the slip coefficient, respectively.

The boundary conditions (6.19) are non-homogenous. Therefore, a filtering function is needed to eliminate non-homogeneity. A one-dimensional problem in y direction is defined such that it satisfies the boundary conditions for the original problem.

$$w(x,y) = w_y(y) + \tilde{w}(x,y), \tag{6.20}$$

where w_y is filtering function, which satisfies the following system

$$\begin{aligned} &\frac{\partial^2 w_y}{\partial y^2} - w_y = 0, \\ &w_y = \beta_s \quad \text{at } y=0 \text{ and } y=\gamma. \end{aligned} \tag{6.21}$$

The solution of the equation above is as follows

$$w_y = \frac{e^y + e^{\gamma - y}}{1+e^\gamma}\beta_s. \tag{6.22}$$

After substitution of (6.20) in (6.18), the governing equation and the boundary conditions (6.19) take the following form:

$$P - w_y = \frac{\partial^2 \tilde{w}}{\partial x^2} + \frac{\partial^2 \tilde{w}}{\partial y^2}, \tag{6.23}$$

$$\begin{aligned} &\tilde{w} = \beta_s - w_y \quad \text{at } x=0 \text{ and } x=1, \\ &\tilde{w} = 0 \quad \text{at } y=0 \text{ and } y=\gamma. \end{aligned} \tag{6.24}$$

The eigenvalue problem in the y-direction is defined. The transform and inversion formulas are written as:

$$\text{Transform} \qquad \overline{\tilde{w}}(\mu_n, x) = \int_0^{\gamma} \frac{\psi_n(\mu_n, y)}{N_n^{1/2}} \tilde{w}(x, y)\, dy, \tag{6.25}$$

$$\text{Inversion:} \qquad \tilde{w}(x, y) = \sum_{n=1}^{\infty} \frac{\psi_n(\mu_n, y)}{N_n^{1/2}} \overline{\tilde{w}}(\mu_n, x). \tag{6.26}$$

The transformation process starts by applying $\int_0^{\gamma} \psi_n\, dy$ to every term in the governing equation

$$\underbrace{\int_0^{\gamma} P\psi_n\, dy}_{I} - \underbrace{\int_0^{\gamma} w_y \psi_n\, dy}_{II} = \underbrace{\int_0^{\gamma} \frac{\partial^2 \tilde{w}}{\partial x^2} \psi_n\, dy}_{III} + \underbrace{\int_0^{\gamma} \frac{\partial^2 \tilde{w}}{\partial y^2} \psi_n\, dy}_{IV}. \tag{6.27}$$

The inversion and transform formulas, the eigenvalue problem and integration by part technique are employed to evaluate the integrals in (6.27). As a result, (6.27) is given as

$$\frac{d^2 \overline{\tilde{w}}}{dx^2} - \mu_n^2 \overline{\tilde{w}} = \frac{\gamma\left(1-(-1)^n\right)}{n\pi\, N_n^{1/2}} P - \frac{n\pi\gamma\left(1-(-1)^n\right)}{\left(\gamma^2 + n^2\pi^2\right) N_n^{1/2}} \beta_s. \tag{6.28}$$

Transformation of boundary condition yields

$$\overline{\tilde{w}} = \frac{\left(1-(-1)^n\right)}{N_n^{1/2}} \left(\frac{\gamma}{n\pi} - \frac{n\pi\, y}{\gamma^2 + n^2\pi^2} \right) \beta_s \qquad \text{at } x=0 \text{ and } x=1. \tag{6.29}$$

The non-homogeneous ordinary differential equation (6.28) is solved analytically and after some arrangements can be given as

$$\overline{\tilde{w}} = K_1(\mu_n, x) P + K_2(\mu_n, x) \beta_s, \tag{6.30}$$

where

$$K_1 = \frac{B_n e^{x\mu_n} + B_n e^{(1-x)\mu_n}}{1 + e^{\mu_n}} - B_n,$$

$$K_2 = \frac{A_n e^{x\mu_n} + A_n e^{(1-x)\mu_n}}{1 + e^{\mu_n}} + C_n,$$

$$A_n = \frac{\left(1-(-1)^n\right)}{N_n^{1/2}} \left(\frac{\gamma}{n\pi} - \frac{n\pi\, y}{\gamma^2 + n^2\pi^2} - \frac{n\pi\, y}{\mu_n^2(\gamma^2 + n^2\pi^2)} \right),$$

$$B_n = \frac{\gamma\left(1-(-1)^n\right)}{\mu_n^2 n\pi N_n^{1/2}},$$

$$C_n = \frac{n\pi\gamma\left(1-(-1)^n\right)}{\left(\gamma^2+n^2\pi^2\right)\mu_n^2 N_n^{1/2}}.$$

$\tilde{w}$ is given by applying the inversion formula as

$$\tilde{w}(x,y) = \sum_n \frac{\left[K_1(\mu_n,x)P + K_2(\mu_n,x)\beta_s\right]\sin\left((n\pi/\gamma)y\right)}{N_n^{1/2}}. \tag{6.31}$$

The final form of velocity profile is given by summing (6.22) and (6.31) as

$$w(x,y) = \frac{e^y + e^{\gamma-y}}{1+e^\gamma}\beta_s + \sum_n \frac{\left[K_1(\mu_n,x)P + K_2(\mu_n,x)\beta_s\right]\sin\left((n\pi/\gamma)y\right)}{N_n^{1/2}}. \tag{6.32}$$

The value of P is obtained by implementing the definition of mean velocity

$$w_m = \frac{1}{WH}\int_0^H\int_0^W w(x,y)dx\,dy. \tag{6.33}$$

Once (6.32) are substituted into (6.33), P is given as follows:

$$P = \frac{1-\left(I_2+I_3\right)\beta_s}{I_1}, \tag{6.34}$$

where

$$I_1 = \frac{1}{\pi N_n^{1/2}}\sum_n \frac{\left(1-(-1)^n\right)}{n}\int_0^1 K_1(\mu_n,x)\,dx,$$

$$I_2 = \frac{1}{\pi N_n^{1/2}}\sum_n \frac{\left(1-(-1)^n\right)}{n}\int_0^1 K_2(\mu_n,x)\,dx,$$

$$I_3 = \frac{2\left(e^\gamma-1\right)}{\gamma\left(e^\gamma+1\right)}.$$

Then the average value of β_s can be calculated by integrating over the length as

$$\beta_s = \int_0^1 \left\{ \left\{ \frac{\pi Kn}{I_1 N_n^{1/2}} \sum_{n=1} n K_1 \right\} \Big/ \left\{ \begin{array}{l} \gamma - \dfrac{\gamma Kn\left(1-e^{\gamma}\right)}{\left(1+e^{\gamma}\right)} + \\ \dfrac{\pi Kn}{N_n^{1/2}} \sum_{n=1} \left(\dfrac{n K_1 \left(I_2 + I_3\right)}{I_1} - n K_2 \right) \end{array} \right\} \right\} dx. \tag{6.35}$$

The equations are solved with MATLAB program. A comparison of the numerical results with the analytical calculation results shows excellent agreements. Three dimensional axial velocity and two dimensional axial velocity are presented in Fig. 6.3 and Fig. 6.4, respectively. Furthermore, two comparisons between the results of the analytical calculation and the numerical simulation at Re=0.1, Kn=0.05, Kn=0.1 and γ=1 are depicted in Fig. 6.5 and Fig. 6.6.

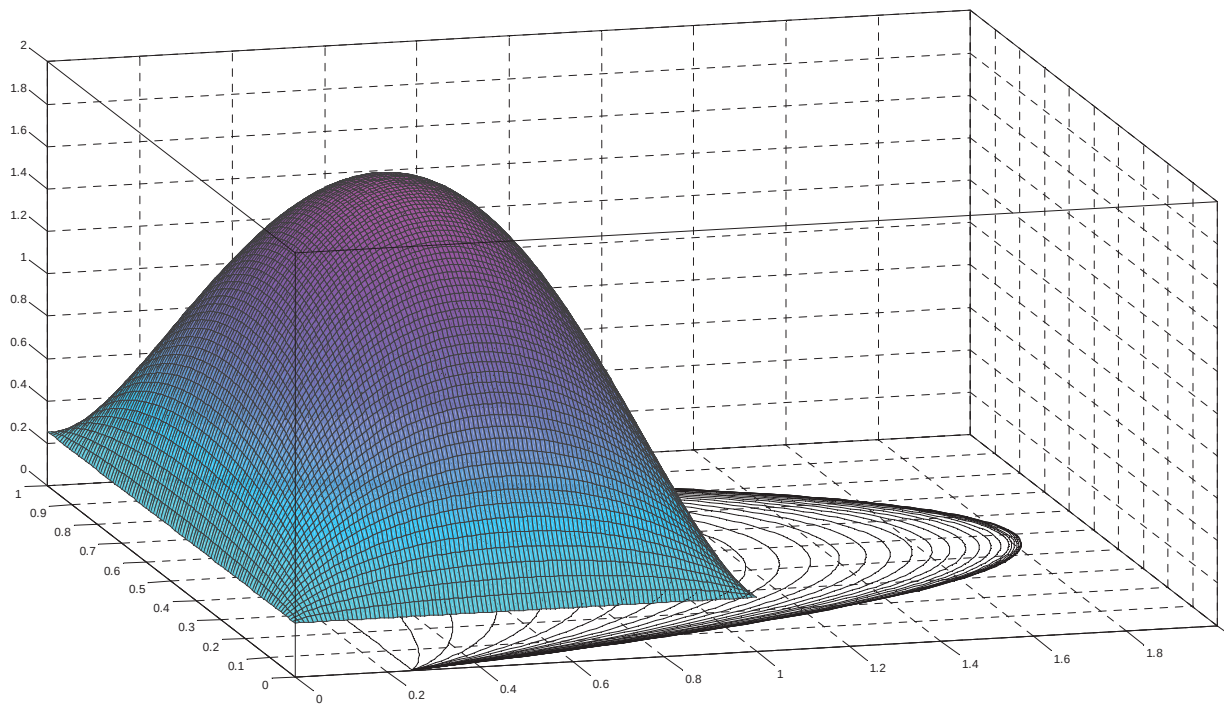

Fig. 6.3 Three and two dimensional axial velocity profile at Kn=0.1, $\gamma = \dfrac{H}{W} = 1$.

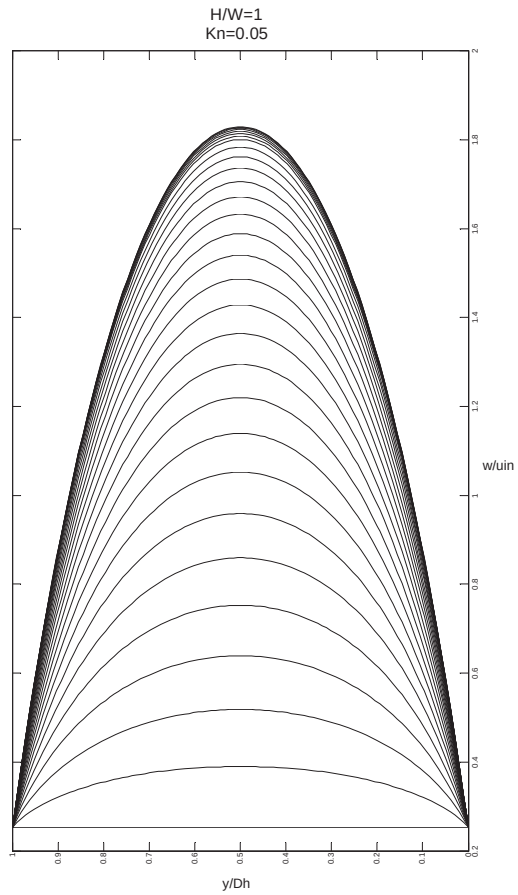

Fig. 6.4 Two dimensional axial velocity profile at Kn=0.05, $\gamma = \dfrac{H}{W} = 1$

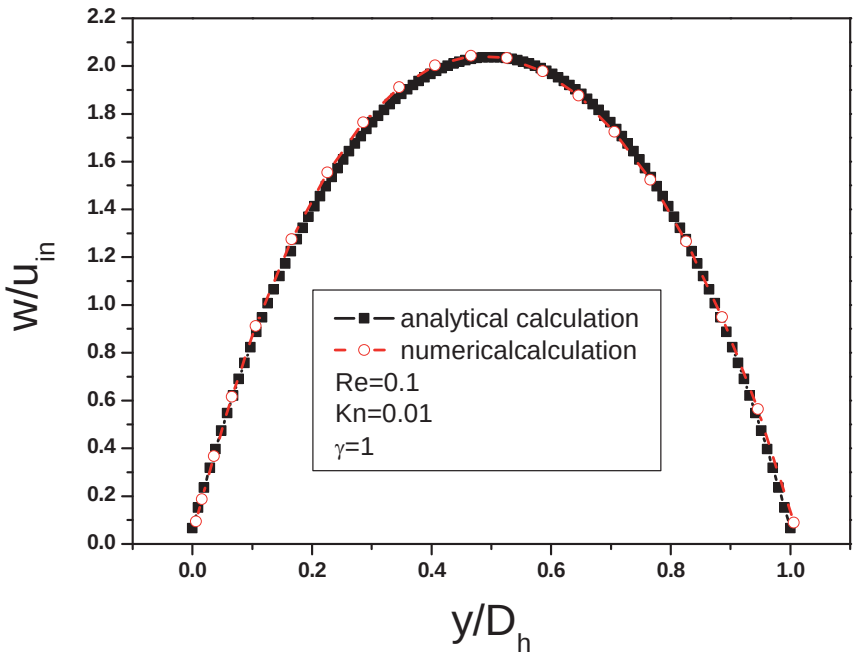

Fig. 6.5 Comparison of the analytical calculation and the numerical calculation results at Kn=0.01, $\gamma = \frac{H}{W} = 1$ and Re=0.1.

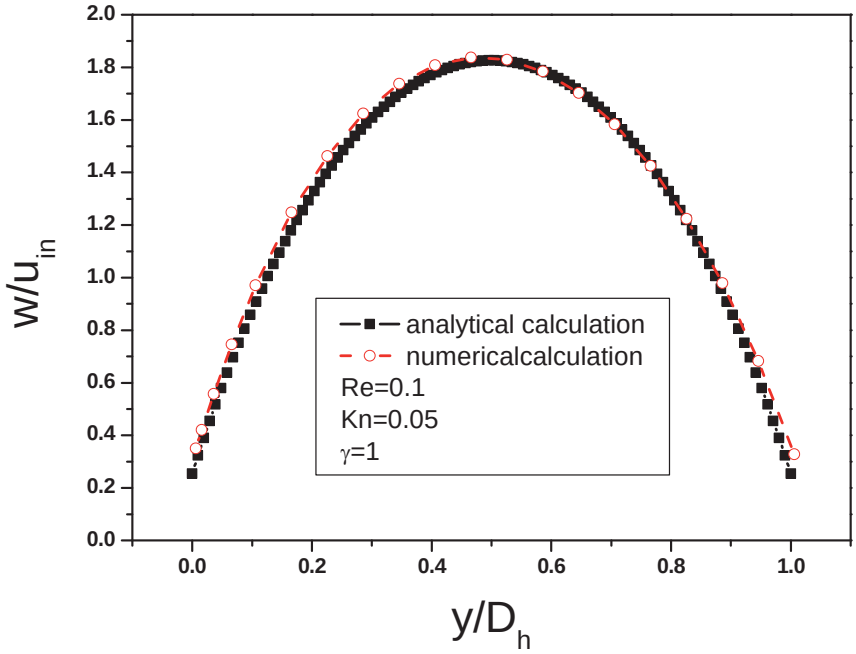

Fig. 6.6 Comparison of the analytical calculation and the numerical calculation results at Kn=0.05, $\gamma = \frac{H}{W} = 1$ and Re=0.1.

Chapter 7

Nanofluid in Microchannels

Cooling of electronic chips is one of the application of microchannels. Heat transfer enhancement is very important and essential in the micro cooler. Employing nanofluids as cooling fluids is one of the best and practical methods for increasing heat transfer in microchannels. In this chapter, thermal and hydraulic behaviors of nanofluid flow in microchannels with consideration of the slip velocity and the jump temperature conditions are investigated and discussed.

Forced convection nanofluid flow in microchannels is simulated to study effects of rarefaction and Al_2O_3 nanoparticles concentration on the slip flow regimes. Navier-Stokes and energy equations with slip velocity and jump temperature boundary conditions are discretized using Finite Volume technique. The Brownian motions of nanoparticles are considered to determine the thermal conductivity of nanofluids. The calculated results show good agreement with the previous numerical and analytical data.

7.1 Introduction

In this chapter, nanofluid flow, which is a new kind of heat transfer fluid, is studied in microchannels.

Up to now, low thermal conductivity base fluids such as air or water have been employed to study the fluid flow in microchannels. The heat transfer of fluid flow is limited based on the thermal properties of the individual fluids. Demand for increasing the heat transfer in microchannels leads to the need for improvement of thermal properties of base fluids. One of the presented solutions for this problem is adding solid nanoparticles with high thermal conductivity such as Al_2O_3, Cu or CuO to the base fluid. These fluids are called nanofluids.

During the past two decades, scientists and researchers have been attempting to develop nanofluids, which can offer better heating performance for a variety of thermal systems compared to traditional heat transfer fluids. It has been found by numerous numerical and experimental studies that nanofluids have high thermal conductivities and abilities to increase the heat transfer in tubes ([PAK98], [XUA03], [BEH06], [AKB07], [AKB08], [AKB09], [SHA11], [MOK11]). Many researchers have investigated the effective thermal conductivity of nanofluids and the effective dynamic viscosity in order to propose some expression for predicting the thermal conductivity and dynamic viscosity of nanofluids [MUR08].

Recently, nanofluids utilization in microchannels has received great interest amongst researchers. Koo and Kleinstreuer [KOO05], Jang and Choi [JAN06] and Chein and Huang [CHE05] experimentally studied the improvement of thermal performance of nanofluid flow in microchannels with different nanofluids, such as CuO-water or Al_2O_3-water. The thermal performance of microchannels using nanofluids based on different models for effective thermal conductivity also has been investigated numerically by Abbassi and Aghanajafi [ABB06], Tsai and Chein [TSA07], Li and Kleinstreuer [LI08], Chein and Chuang [CHE07], Jung et al. [JUN09], Ho et al. [HO10]. They evaluated the impacts of parameters such as microchannel geometry, Reynolds number and nanoparticles volume fraction on the thermal performance of nanofluid flow in microchannels. They reported higher heat transfer performance of nanofluids

flow compare with the base fluids in microchannels. However, all of them used the non-slip flow regimes in their numerical research works.

Numerical studies on nanofluid flow and heat transfer in microchannels have employed the non-slip flow regimes which have caused a significant overestimate of heat transfer coefficient. The objective of the present chapter is to describe the effects of particles concentration and rarefaction on the hydrodynamic and thermal parameters of laminar forced convection slip flow of a nanofluid in a rectangular microchannel. The slip velocity and the jump temperature boundary conditions at the fluid-wall interface are applied. Simultaneous effects of the slip velocity, jump temperature and nanoparticles volume fraction in the base fluid on heat transfer augmentation are studied. The axial velocity, entrance length, pressure, Poiseuille number, temperature and Nusselt number profiles for different values of the particles concentrations, Reynolds number and Knudsen number are presented and discussed ([AKB11A], [AKB10A], [AKB11B]).

7.2 Mathematical Model

7.2.1 Governing equations

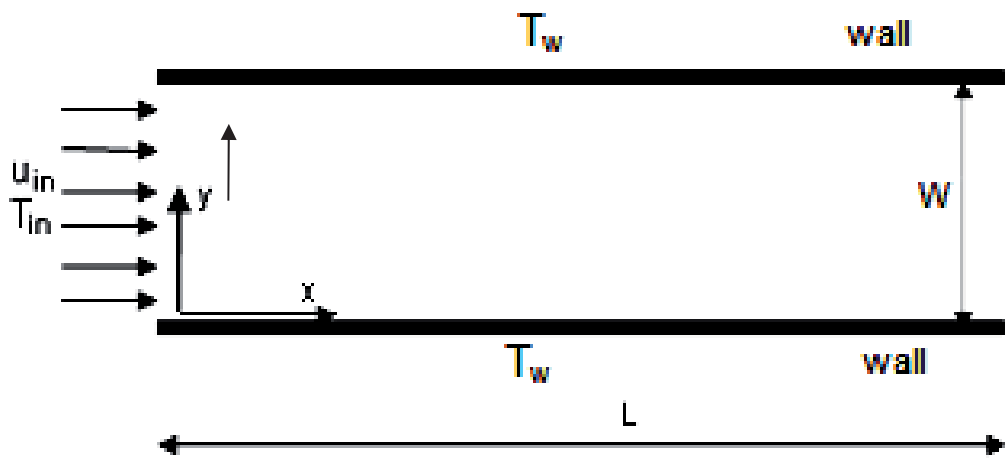

Fig. 7.1 Schematic diagram of two dimension rectangular microchannel.

The schematic of the channel and coordinate system are shown in Fig. 7.1. The flow is considered along the x-axis and the length of channel is set to a value greater than the estimated entrance length of the flow to ensure that fully developed conditions are achieved at the exit. The Al_2O_3-water nanofluid flow and the heat transfer in the rectangular microchannels have been considered. The nanofluid flow is laminar, steady state and incompressible with constant properties while dissipation, pressure work and body forces are neglected.

The used properties of base fluid (water) and solid nanoparticles (Al_2O_3) are presented in Table 7.1. The rarefaction effects set the slip velocity and the jump temperature at the fluid–wall interface. Therefore, the steady state governing equations describing the fluid flow and the heat transfer in the microchannel in the Cartesian coordinate and in the tensors form are as follows:

- continuity equation:

$$\frac{\partial u_j}{\partial x_j} = 0, \tag{7.1}$$

- momentum equations:

$$\rho_{nf} \frac{\partial}{\partial x_j}(u_i u_j) = \mu_{nf} \frac{\partial}{\partial x_j}\left((\frac{\partial u_i}{\partial x_j}) \right) - \frac{\partial p}{\partial x_i}, \tag{7.2}$$

- fluid energy equation:

$$(\rho C_p)_{nf} \frac{\partial}{\partial x_i}(u_i T) = k_{nf} \frac{\partial}{\partial x_i}\left(\frac{\partial T}{\partial x_i} \right), \tag{7.3}$$

where i=1, 2 and u_x and u_y are velocity components.

The continuity, momentum and energy equations are made non-dimensional using the following dimensionless parameters:

$$X_i = \frac{x_i}{D_h}\ ,\ U_i = \frac{u_i}{u_{in}}\ ,\ P = \frac{p}{\rho_{nf} u_{in}^2} \text{ and } \theta = \frac{T - T_{in}}{T_{wall} - T_{in}}, \tag{7.4}$$

where $D_h \approx 2W$.

Table 7.1. Thermo physical properties of nanoparticles and base fluid at 22^0C

Properties	Water	Nanoparticle(Al_2O_3)
Density $\boldsymbol{\rho}$(kg/m^3)	998.2	3890
Heat capacitance $\mathbf{C_p}$ (J/kg.K)	4240	880
Thermal conductivity **k** (W/mK)	0.608	35

Therefore, the non-dimensional governing equations become as follows:

- continuity equation:

$$\frac{\partial U_j}{\partial X_j} = 0, \tag{7.5}$$

- momentum equations:

$$\frac{\partial}{\partial X_j}(U_i U_j) = \frac{1}{\mathrm{Re}_{nf}}\left(\frac{\partial^2 U_i}{\partial X_j^2}\right) - \frac{\partial P}{\partial X_i}, \tag{7.6}$$

- fluid energy equation:

$$\frac{\partial}{\partial X_i}(U_i\theta) = \frac{1}{Pe_{nf}}\frac{\partial^2\theta}{\partial X_i}, \tag{7.7}$$

where $Pe_{nf} = \mathrm{Re}_{nf}\,\mathrm{Pr}_{nf}$, $\mathrm{Re}_{nf} = \dfrac{\rho_{nf}\,u_{in}\,D_h}{\mu_{nf}}$ and $\mathrm{Pr}_{nf} = \dfrac{\mu_{nf}(C_p)_{nf}}{k_{nf}}$ are the Peclet number, the Reynolds number and the Prandtl number, respectively (see appendix A for details about dimensionless numbers).

7.2.2 Nanofluid properties

The physical properties of nanofluid containing water-Al_2O_3 can be calculated as follows:

- density:

$$\rho_{nf} = (1-\phi)\rho_f + \phi\rho_s, \tag{7.8}$$

- heat capacitance:

$$(\rho C_p)_{nf} = (1-\phi)(\rho C_p)_f + \phi(\rho C_p)_s \ . \tag{7.9}$$

- The presented expression for dynamic viscosity by Maiga et al. [MAI04], which was determined based on available experimental results for water-Al_2O_3, is given as

$$\mu_{nf} = (123\,\phi^2 + 7.3\,\phi + 1)\,\mu_f \ . \tag{7.10}$$

- The thermal conductivity of water-Al_2O_3 nanofluid has been determined from Chon et al. [CHO05] correlation which considers the Brownian motion and mean diameter of the nanoparticles as

$$\frac{k_{nf}}{k_f} = 1 + 64.7\,\phi^{0.7460}\left(\frac{d_f}{d_s}\right)^{0.3690}\left(\frac{k_s}{k_f}\right)^{0.7476} \mathrm{Pr}_f^{\,0.9955}\,\mathrm{Re}_f^{\,1.2321}, \tag{7.11}$$

where Pr_f and Re_f in (7.11) are defined as:

$$\mathrm{Pr}_f = \frac{\mu}{\rho_f\,\alpha_f}, \tag{7.12}$$

$$\mathrm{Re}_f = \frac{\rho k_B T}{3\pi\eta^2\lambda_f}, \tag{7.13}$$

where λ_f is mean free path of water molecular (λ_f =0.17nm), k_B is Boltzmann constant (k_B=1.3807×10^{-23} J/K). η is calculated by

$$\eta = A\cdot 10^{\frac{B}{T-C}}\ ,\ \mathrm{A}=2.414\times10^{-5},\ \mathrm{B}=247.8,\ \mathrm{C}=140. \tag{7.14}$$

7.2.3 Slip velocity and jump temperature

The second order non-dimensional velocity slip condition is expressed as follows [GAD06]:

$$U = \left(\frac{2-\sigma_V}{\sigma_V}\right) Kn \left.\frac{\partial U}{\partial Y}\right|_{wall} + \frac{3}{2\pi}\frac{(\gamma-1)}{\gamma}\frac{Kn^2 \operatorname{Re}}{Ec}\left.\frac{\partial \theta}{\partial X}\right|_{wall} \tag{7.15}$$

here Ec is Eckert number ($Ec = \frac{U^2}{C_p \Delta T}$). The second term can be negligible if $\frac{\partial}{\partial Y} >> \frac{\partial}{\partial X}$ at the wall and also due to the fact that it is second order in the Knudsen number. Similar arguments can be applied to the jump temperature boundary condition, and the resulting from Taylor series leads in dimensionless form (([GAD06]):

$$\theta - \theta_{wall} = \left(\frac{2-\sigma_T}{\sigma_T}\right)\left(\frac{2\gamma}{\gamma+1}\right)\frac{1}{\Pr}\left[Kn\left(\left.\frac{\partial \theta}{\partial Y}\right|_{wall}\right) + \frac{Kn^2}{2!}\left(\left.\frac{\partial^2 \theta}{\partial Y^2}\right|_{wall}\right) + \ldots\right]. \tag{7.16}$$

Values of the thermal and momentum accommodation coefficients (σ_V, σ_T) are near unity for most engineering applications and they are taken as unity in the present study.

After simplifying, the non-dimensional forms of the slip flow velocity and jump temperature boundary conditions are given by:

$$U - U_{wall} = Kn \left.\frac{\partial U}{\partial Y}\right|_{wall}, \tag{7.17}$$

$$\theta - \theta_{wall} = \frac{Kn}{\beta}\left.\frac{\partial \theta}{\partial Y}\right|_{wall}, \tag{7.18}$$

where

$$\beta = \Pr\left(\frac{\gamma+1}{2\gamma}\right), \tag{7.19}$$

θ_{wall}=1 and U_{wall}=0.

7.2.4 Boundary conditions

These sets of nonlinear elliptical governing equations (7.1) to (7.3) are solved subject to following boundary conditions:

- At the channel inlet, the flow velocity and the temperature are assumed uniform and constant (X=0, 0≤Y≤0.5: U=1, θ=0),
- At the fluid-solid interface: The flow velocity in y direction is zero. The slip velocity of the nanofluid flow adjacent to the wall is proportional to the normal velocity gradient at the wall (7.17). The jump temperature of the nanofluid flow adjacent to the wall is proportional to temperature gradient at the fluid–wall interface (7.18). Furthermore, a constant temperature (θ_{wall}=1) at the wall is applied,
- At the channel outlet (*x*=L), the diffusion flux in the direction normal to the exit is assumed to be zero for velocity and temperature. A zero pressure is assigned at the flow exit. (X=10, 0≤Y≤0.5: $\frac{\partial U}{\partial X} = \frac{\partial \theta}{\partial X} = 0$, P=0).

7.3 Numerical Methods and Validations

The sets of coupled non-linear differential equations (7.1) to (7.3) are discretized using the Finite Volume technique. The Power Law scheme is used for the convective and diffusive terms while the *SIMPLER* procedure is introduced to couple the velocity-pressure as described by Patankar [PAT80].

With the following procedure, the slip velocity and the jump temperature boundary conditions are employed in the discretization equations. A control volume close to the wall boundary is shown in Fig. 2. Here, only the procedure for the slip velocity is considered that can be written similarly for the jump temperature. The slip velocity near the wall from Eq.(7.17) with the notation as used in Fig. 7.2 is given as

$$U_N - U_{wall} = Kn \left.\frac{\partial U}{\partial Y}\right|_{wall}, \tag{7.20}$$

where U_{wall} is equal to zero. By applying a first order approximation for the velocity gradient close to the wall we obtain:

$$\left.\frac{\partial U}{\partial Y}\right|_{wall} = \frac{U_P - U_N}{\Delta Y}. \tag{7.21}$$

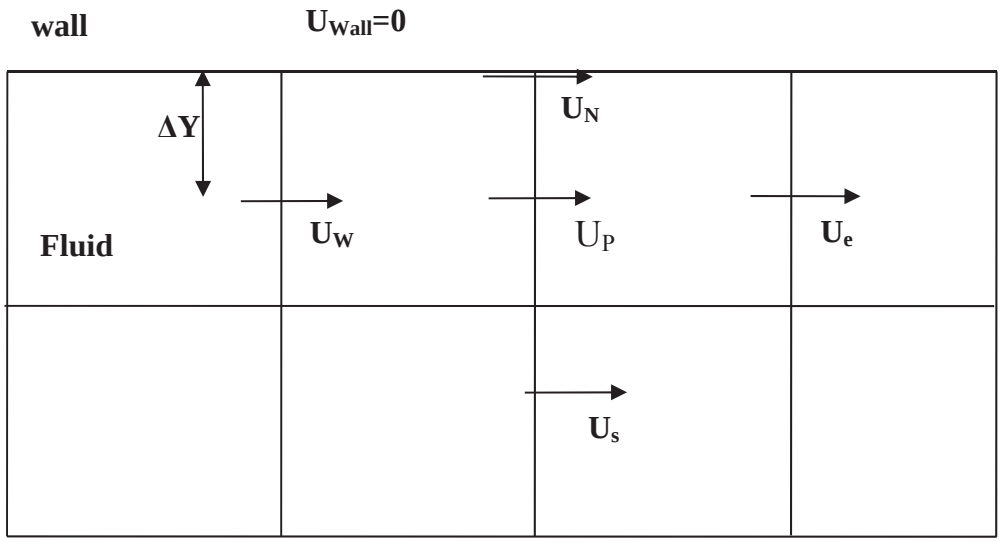

Fig. 7.2 a Control volume near the wall.

By inserting (7.21) into (7.20) we obtain

$$U_N - U_{wall} = Kn\frac{U_P - U_N}{\Delta Y} \tag{7.22}$$

and consequently,

$$U_N - U_P = \frac{(U_{wall} - U_P)}{\left(1 + \frac{Kn}{\Delta Y}\right)}. \tag{7.23}$$

The discretized momentum equation for a control volume adjacent to the wall from Patankar [PAT80] is given as:

$$a_N(U_N - U_p) + a_S(U_S - U_p) + a_E(U_E - U_p) + a_W(U_W - U_p) + b = 0. \tag{7.24}$$

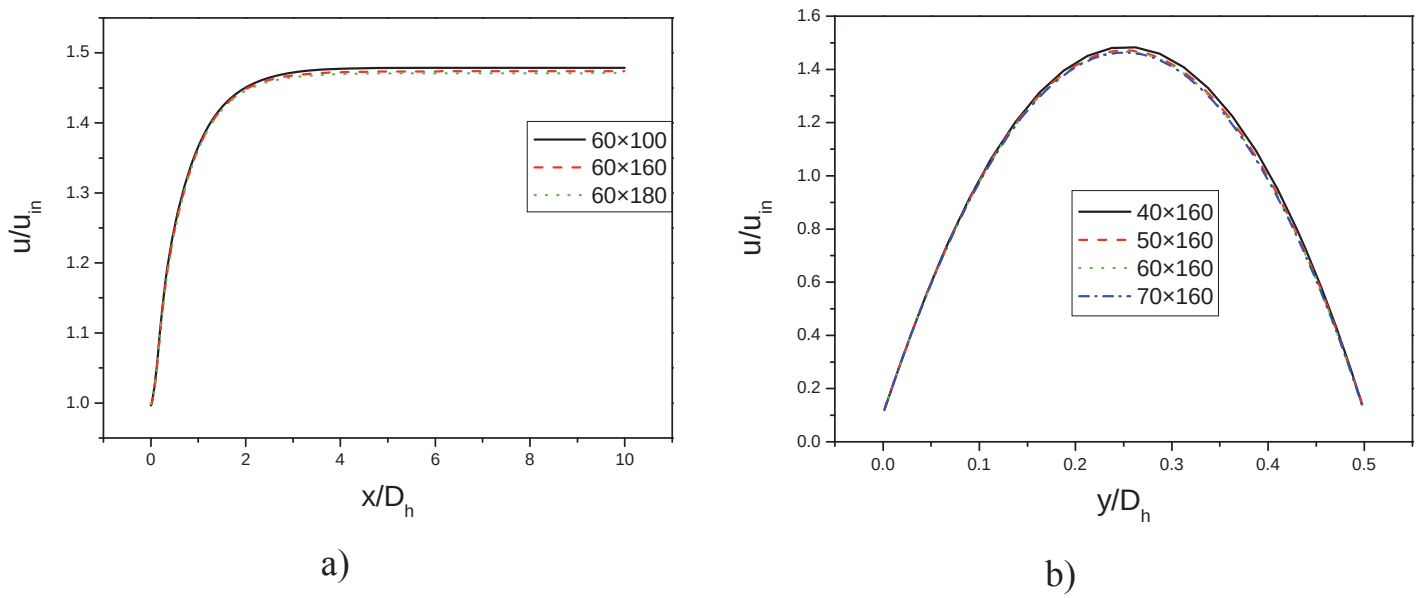

Fig. 7.3 Grid sensibility test a) in x direction b) in y direction.

After replacing the term (U_N-U_P) from (7.23) into (7.24), it is written as

$$\frac{(a_N)}{\left(1+\frac{Kn}{\Delta Y}\right)}(U_N-U_p)+a_S(U_S-U_p)+a_E(U_E-U_p)+a_W(U_W-U_p)+b=0. \tag{7.25}$$

A similar procedure for the jump temperature boundary condition in the discretized energy equation is given as

$$\frac{(b_N)}{\left(1+\frac{Kn}{\beta\Delta Y}\right)}(\theta_N-\theta_p)+b_S(\theta_S-\theta_p)+b_E(\theta_E-\theta_p)+b_W(\theta_W-\theta_p)+b_T=0. \tag{7.26}$$

A structured non uniform grid distribution is used for the computational domain. It is finer near the microchannel entrance and near the wall, where the velocity and the temperature gradients are high. The channel length are set to a value greater than the estimated entrance lengths of the flow to ensure that fully developed conditions are achieved at the exit. Several different grid distributions are tested to ensure the calculated results are grid independent. As it is shown in

Fig. 7.3, increasing the quantity of nodes more than 60 nodes in y direction and 160 nodes in x direction does not change the velocity significantly.

Therefore, the selected grid for the present calculations consists of 160×60 nodes in the x and y directions respectively. The solution is assumed converged when $\left|\frac{\left(\Phi^{n+1}-\Phi^{n}\right)}{\Phi^{n+1}}\right| \le 10^{-6}$ is satisfied for all independent variables.

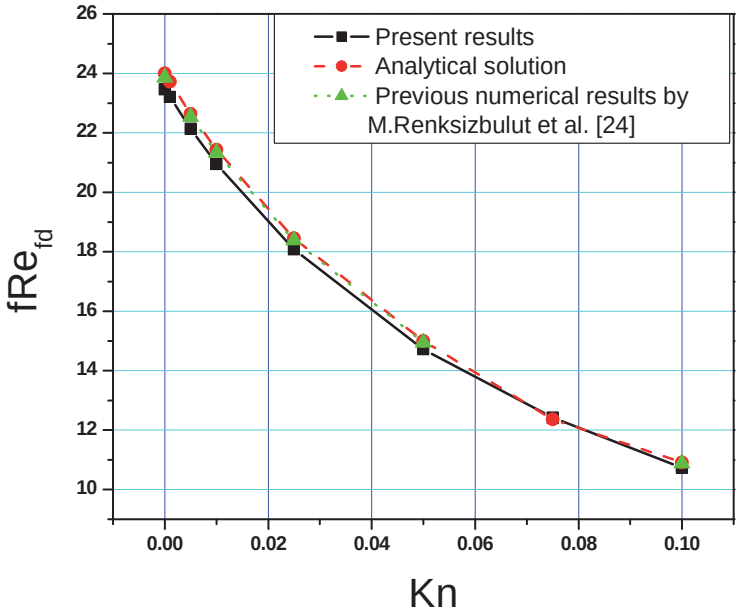

Fig. 7.4 Comparison of the local Poiseuille number with results of Renksizbulut et al. [REN06]

In order to demonstrate the validity and precision of the model assumptions and the numerical analysis, fully developed values of the Poiseuille numbers are compared with available numerical and analytical solutions at *Re*=100 for different Kn. The calculated Poiseuille number in Fig. 7.4 shows a good agreement with numerical results by Renksizbulut et al. [REN06] and analytical values, which vary with *Kn* according to $f\,\mathrm{Re}_{fd} = \frac{24}{(1+12Kn)}$.

The local Nusselt numbers are compared with the results of Yu and Ameel [YU01] for *Kn*=0.04, *β*=10 and infinity aspect ratio as presented in Fig. 7.5. As seen from this figure, a significant agreement between the calculated and numerical results are observed.

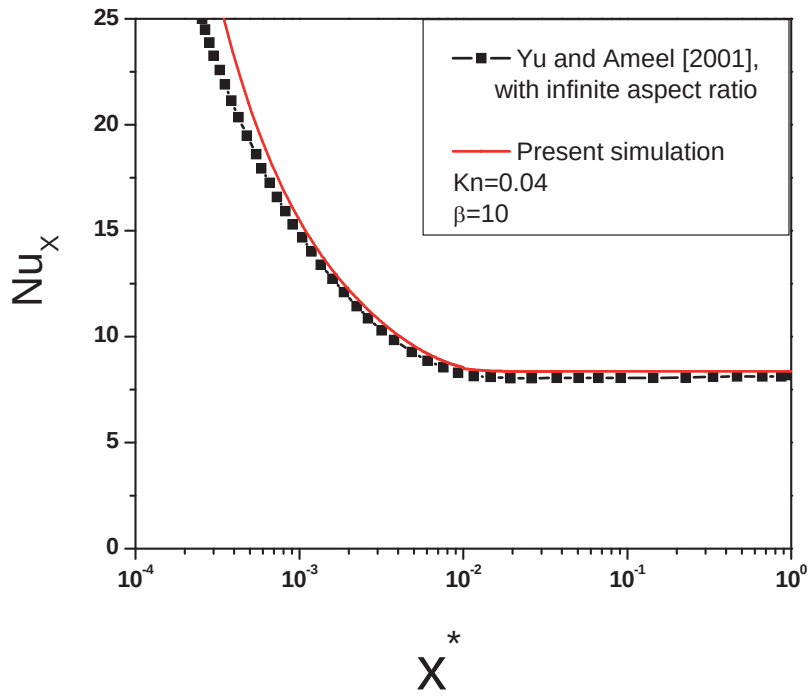

Fig. 7.5 Comparison of the local Nusselt number with results of Yu and Ameel [YU01].

7.4 Results and Discussion

Numerical simulations are done on a wide range of *Re* and *Kn* for four different values of particles concentrations. However, because of similar behaviors and also due to lack of space, the results presented here are almost for *Re* =0.1, 1, 10 and 100 also four different *Kn* with four different values of particles concentrations (0%, 1%, 3%, 5%).

7.4.1 Velocity field

The velocity profiles for different nanoparticles volume fraction (ϕ) at Re=10 and *Kn*=0.01 are shown in Fig. 7.6. The non-dimensional momentum equation (7.6) is only dependent on the Reynolds number parameter. Therefore, at a given *Re* the solid volume fraction does not have any effect on the non-dimensional velocity which is illustrated in Fig. 7.6a and Fig. 7.6b.

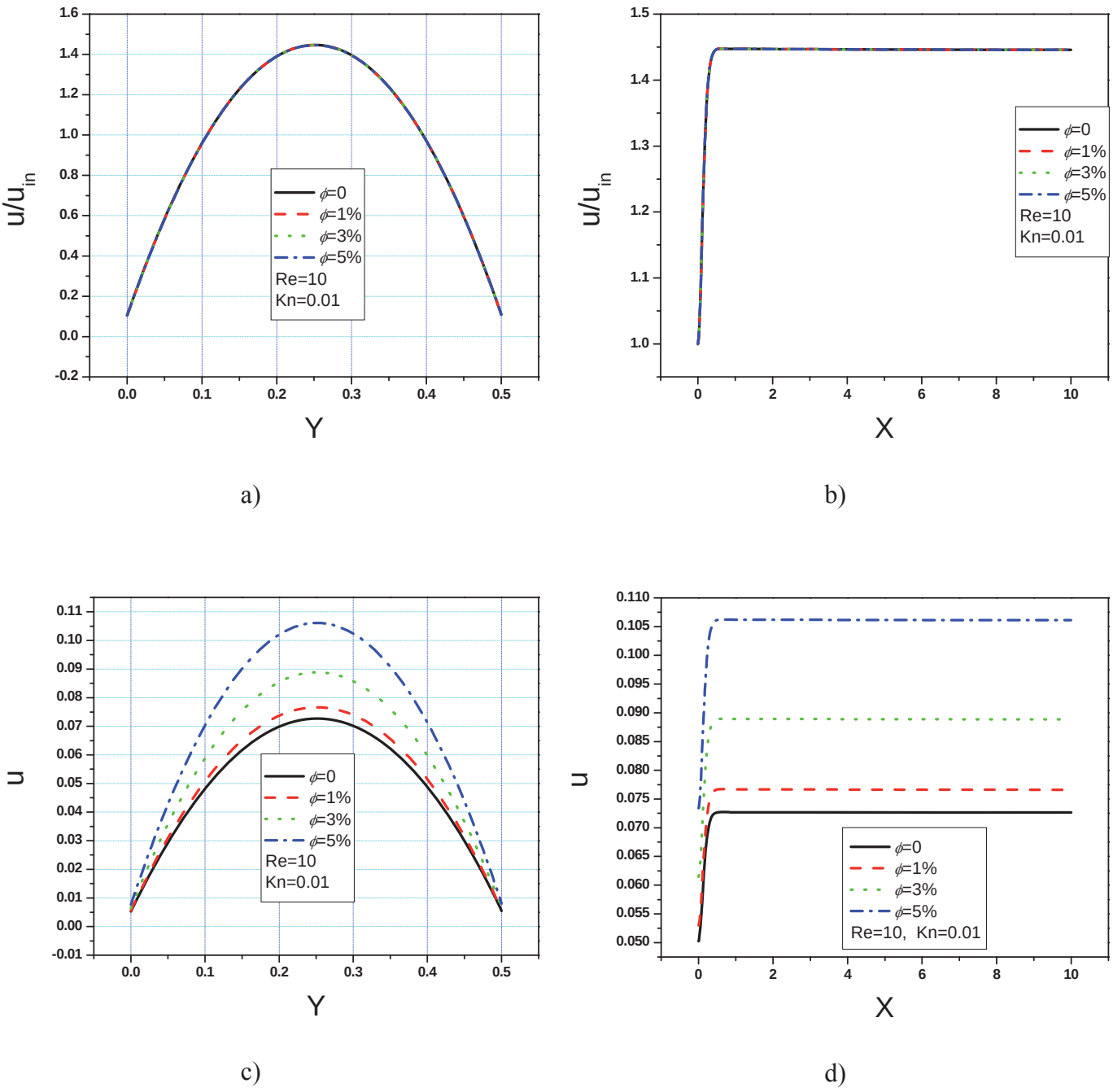

Fig. 7.6 Variation of the non-dimensional (a,b) and dimensional velocity profile (c,d) with nanoparticles concentration at Re=10 and *Kn*=0.01

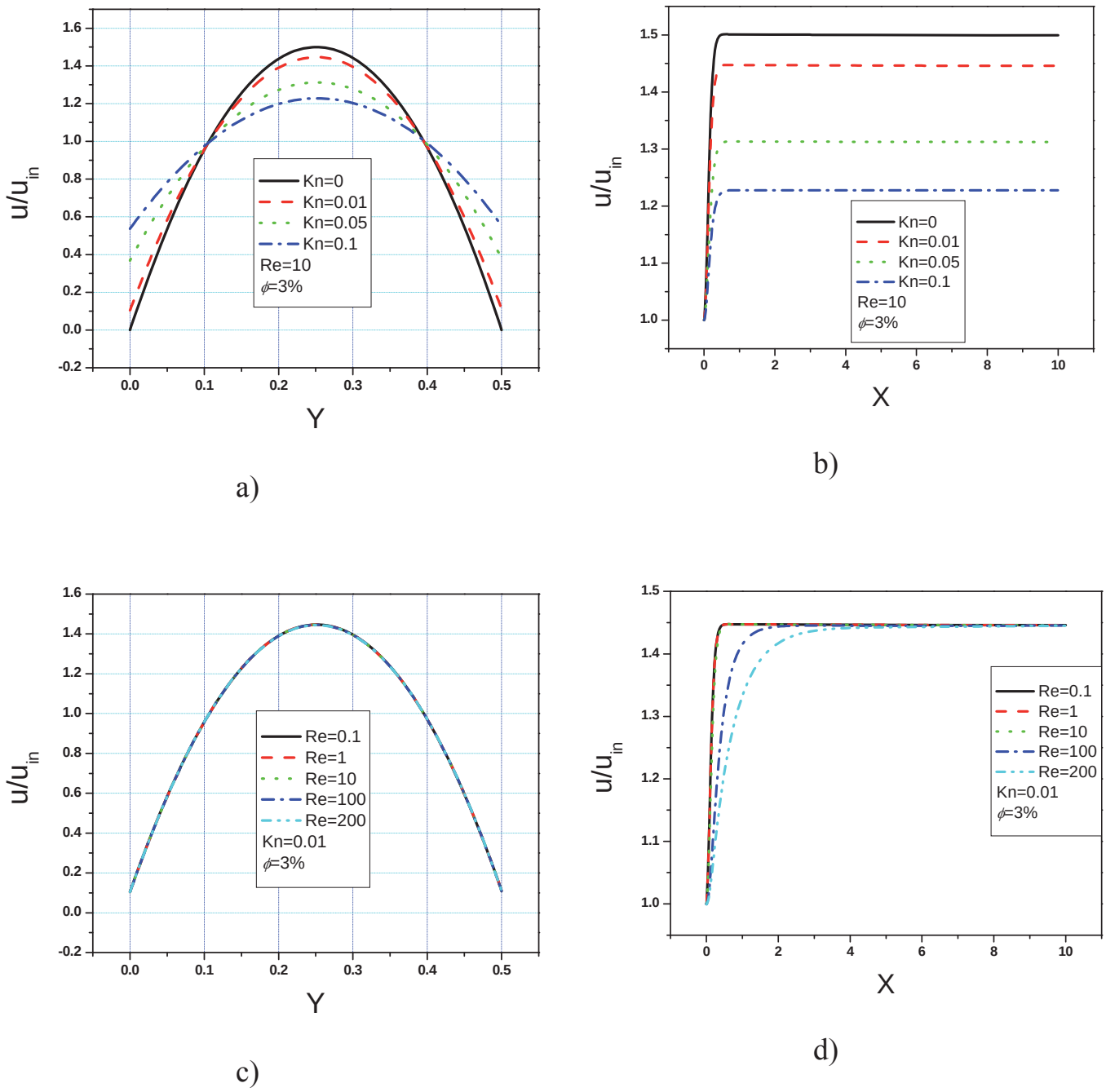

Fig. 7.7 Variation of the non-dimensional velocity with the slip velocity (a,b) and with the Reynolds number (c,d) at ϕ=0.03.

However at a given *Re*, the inlet velocity should be increased with increasing the solid volume fraction due to keep *Re* constant. Consequently, the velocity in any cross section increase which is presented in Fig. 7.6c and Fig. 7.6d.

Variation of velocity with the slip velocity and the Reynolds number is shown in Fig. 7.7. The slip velocity has an increasing effect on the velocity near the

walls while the maximum velocity decreases as a result of the mass continuity; as illustrated in Fig. 7.7a and Fig. 7.7b. It is notable, that the velocity profiles in the slip flow regimes are flattened compared to the non-slip flow regimes.

It is presented in Fig. 7.7c and Fig. 7.7d that the Reynolds number does not have any effect on the non-dimensional velocity, but it postpones the fully developing zone.

7.4.2 Pressure drop

Variation of the pressure drop with the nanoparticles volume fraction and the slip velocity at different *Re* is shown in Fig. 7.8. The slip velocity allows the fluid near the walls to flow. Therefore a smaller pressure drop take place in the channel. As a result, the pressure drop reduces with increasing slip velocity (*Kn*) at the wall.

Fig. 7.8a shows that increasing the solid nanoparticles volume fraction (ϕ) increases the pressure drop at any *Re*. At a given Re, the velocity should be increases with increasing ϕ (see Fig. 7.6c and Fig. 7.6d), consequently pressure drop increases.

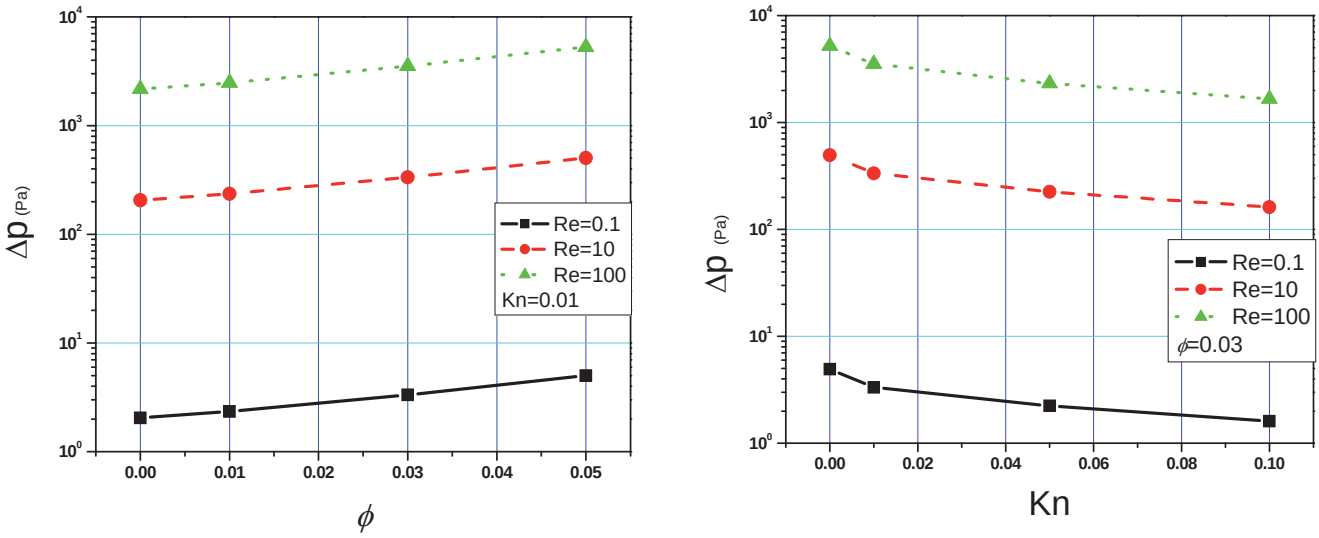

a) b)

Fig. 7.8 Variation of the pressure drop in microchannel with a) the solid volume fraction at Kn=0.01 and with b) the Knudsen number at ϕ=0.03

7.4.3 Skin friction factor

The local Poiseuille number at different ϕ, *Kn* and *Re* is presented in Fig. 7.9. The nanoparticle volume fraction does not change the non-dimensional velocity at a given *Re* (see Fig. 7.6a and Fig. 7.6b). Consequently, it does not have any effect on the Poiseuille number in the micro or macro (*Kn*=0) scale, which is depicted in Fig. 7.9a and Fig. 7.9b, respectively. The Fig. 7.9c shows that in the entrance region, the slip velocity results in a large reduction of the friction coefficient. For the non-slip flow, $X = 0$ is a singularity plane resulting in an infinitely large wall shear. For the slip flows the friction coefficient value at the channel inlet is finite as seen in Fig. 7.9c, which can be easily shown that the friction coefficient profiles start with value nearly $\frac{2}{Kn}$ for the case of the slip flow while its value is infinite for the non-slip flow (*Kn*=0).

In the slip flow, the layer of fluid close to the wall can flow. The changes in the stream-wise velocity profile to reach its final fully developed profile require much less momentum in compared to the non-slip flow regimes.

The slip velocity reduces the velocity gradient at the wall (see Fig. 7.7a). Consequently, increasing *Kn* reduces the Poiseuille number of the slip flow regimes in microchannels.

It is interesting that in the case of high *Kn* (Kn=0.1), the local friction coefficient values do not change significantly from the inlet to the outlet (see Fig. 7.9c). Increasing *Re* increases the Poiseuille number, but it does not have any significant effect on the entrance and fully developed values of *fRe*.

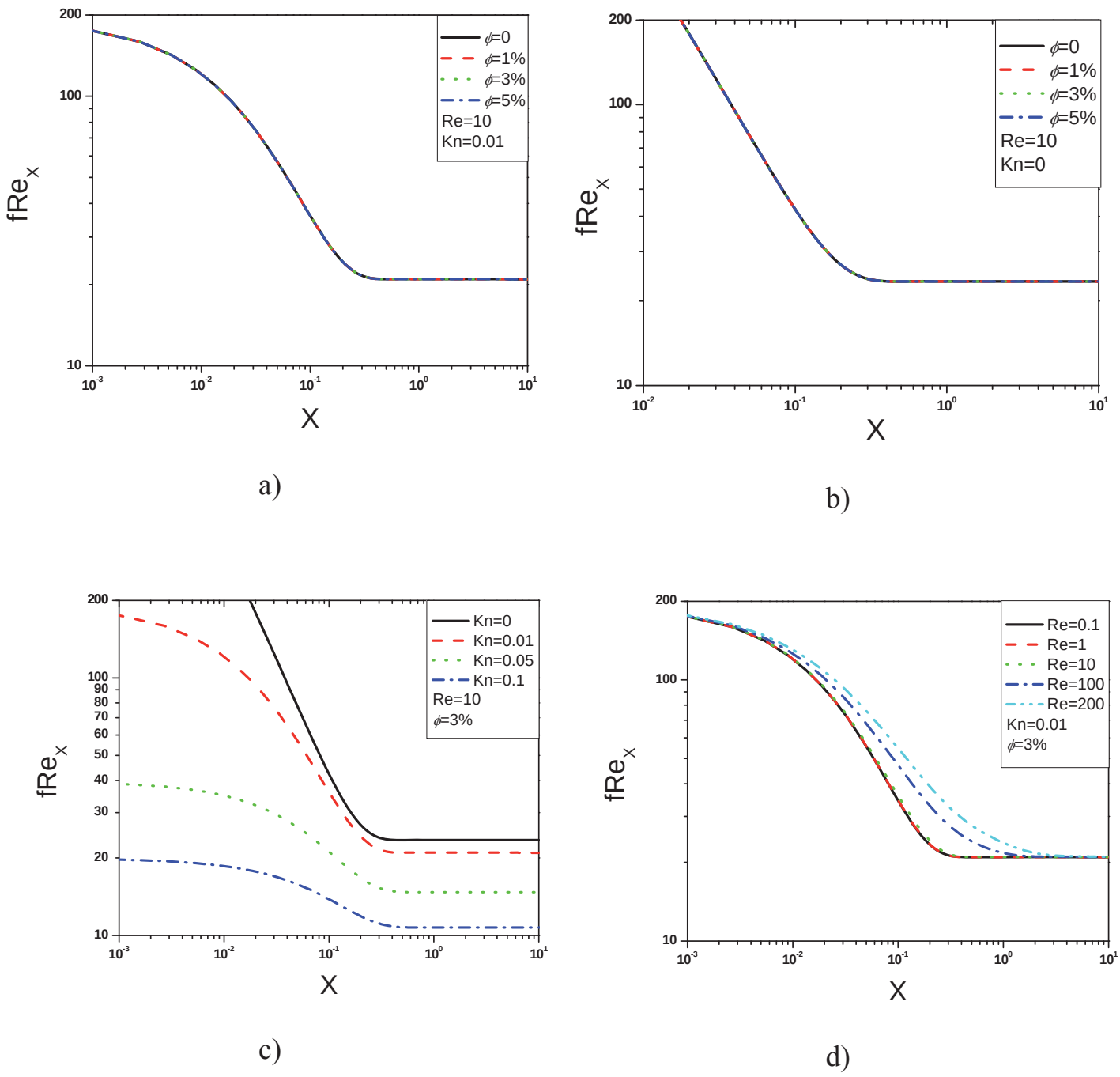

Fig. 7.9 The Poiseuille number profile at a) Re=10 and Kn=0.01 with different ϕ, b)Re=10 and Kn=0 with different ϕ, c) Re=10 and ϕ=0.03 with different Kn, d) *Kn*=0.01 and ϕ=0.03 with different *Re*

7.4.4 Entrance length

The effects of the slip velocity and *Re* on the variations of the entrance length in the microchannels are presented in Fig. 7.10. The dimensionless entrance length, X_{en} , is defined as the distance where the maximum velocity reaches 99% times the corresponding fully developed value over hydraulic diameter. The nanoparticles volume fraction does not have any effect on the non-dimensional velocity (see Fig. 7.6a and Fig. 7.6b), therefore it does not affect the entrance length. It is presented in Fig. 7.10, that the slip velocity has an increasing effect on the entrance length as well as the Reynolds number, but effect of *Re* is more significant.

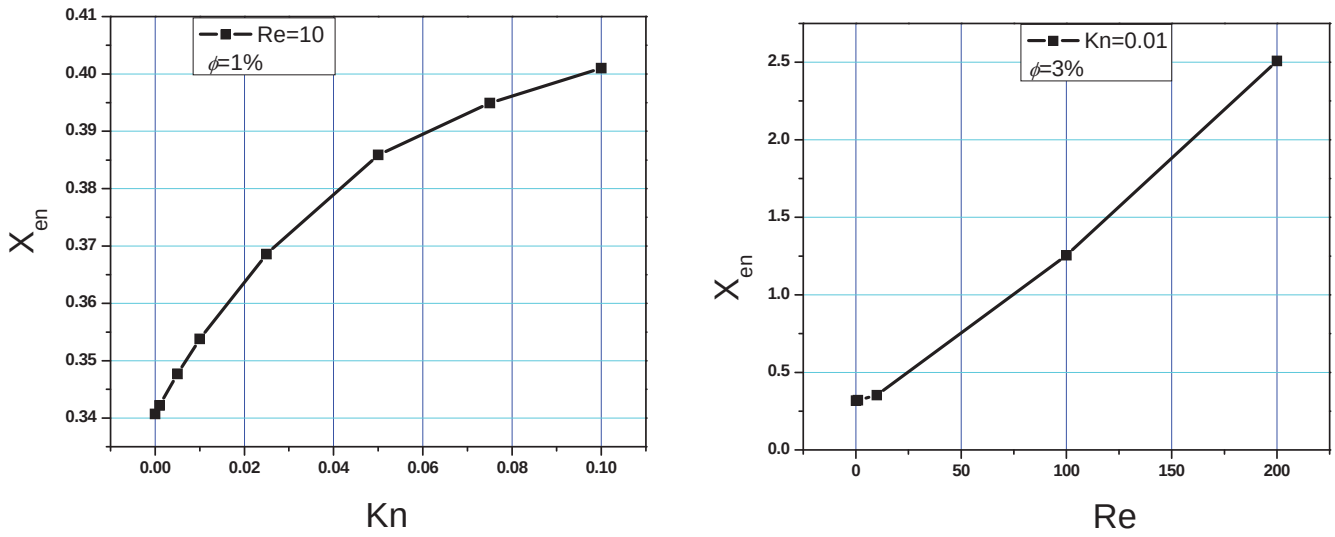

a) b)

Fig. 7.10 The entrance length at a) *Re*=10 , ϕ=0.01 and b) *Kn*=0.01 and ϕ=0.03

7.4.5 Temperature field

Variation of the non-dimensional temperature and bulk temperature with the nanoparticle volume fraction (ϕ) and the slip velocity (*Kn*) are presented in Fig. 7.11. Increasing ϕ decreases the bulk temperature. Increasing *Kn* increases the temperature at any cross section. Both *Kn* and ϕ cause the temperature gradient at the wall to increase. Consequently, both the slip velocity and the solid volume fraction could increase the heat transfer in the microchannel.

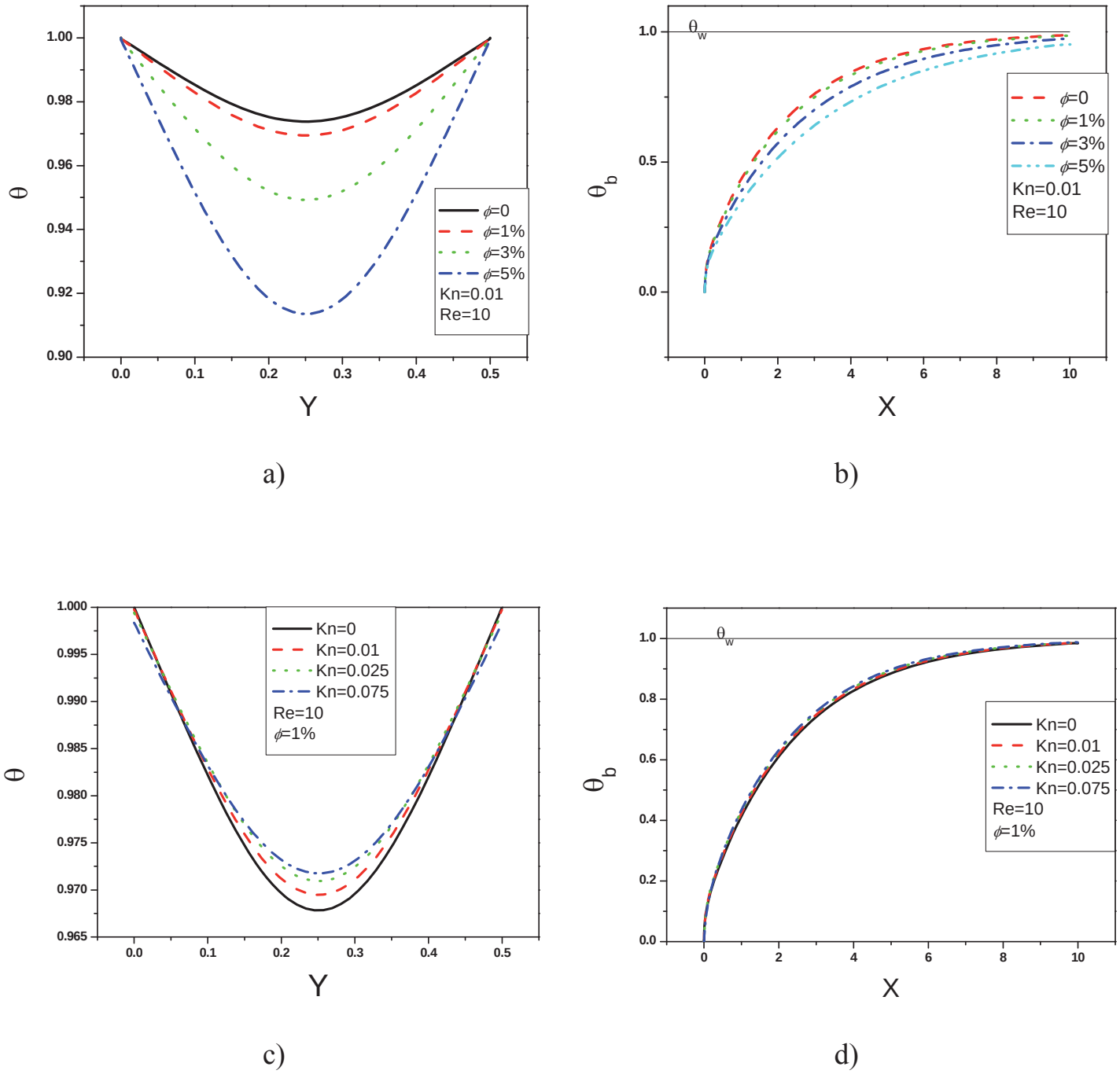

Fig. 7.11 Effects of ϕ at *Re*=10 and *Kn*=0.01 on a) the non-dimensional temperature at the outlet, b) the non-dimensional bulk temperature along the channel. Effect of *Kn* at *Re*=10 and ϕ=0.01 on c) and d) non-dimensional temperature profile at outlet and bulk temperature, respectively.

7.4.6 Nusselt number

Variation of the local Nusselt number profile with the nanoparticles volume fraction, the slip velocity and the Reynolds number are presented in Fig. 7.12. Increasing ϕ has a positive effect on the local Nusselt number. It causes an increase in the local Nusselt number in the slip flow (Kn=0.01) and non-slip flow (Kn=0) regimes.

In the slip flow, presence of the slip velocity and the jump temperature significantly affect the local Nusselt number. The slip velocity increases the advection near the wall, consequently the heat transfer increases. The jump temperature increases the thermal resistance at wall-fluid interface causing a decrease in the heat transfer. The combined effect of the slip velocity and the jump temperature can increase or decrease the heat transfer depending on their relative magnitude.

It is illustrated in Fig. 7.12c that increasing the slip velocity and jump temperature (increasing Kn) in nanofluid flow ($7 \leq \beta = Pr \leq 10$) reduces the local Nusselt number in the beginning part of the microchannel. It increases the local Nusselt number after passing the beginning.

It is notable that similar to the skin friction factor, for the non-slip flow $X^+ = 0$ is a singularity plane for the Nusselt number, but it has a finite value for the slip flow regime which can be obtained as $\frac{\beta}{Kn}$. As it is expected, increasing Re increases the local Nusselt number which is illustrated in Fig. 7.12d.

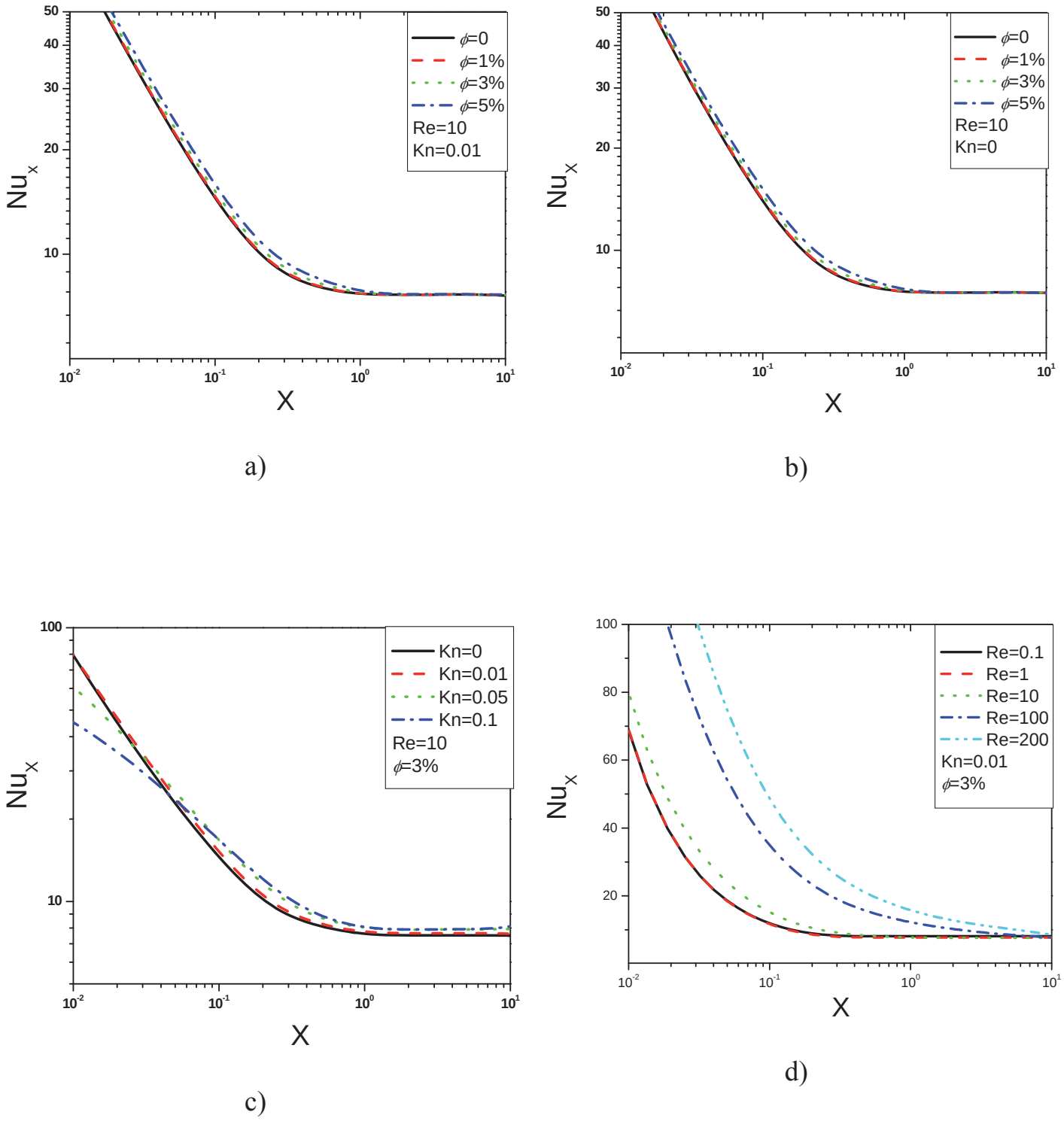

Fig. 7.12 Variation of the Nusselt number with a) the nanoparticles volume fraction at Re=10 and Kn0.01, b)the nanoparticles volume fraction at Re=10 and Kn0, c) the slip velocity at Re=10 and ϕ=0.03, and d) the Reynolds number at Kn=0.01 and ϕ=0.03

7.5 Conclusions

Forced convection nanofluid flow in microchannels is simulated to study effects of rarefaction and Al_2O_3 nanoparticles concentration on the slip flow regimes. The Brownian motions of nanoparticles are considered to determine the thermal conductivity of nanofluids.

The results show that the non-dimensional velocity profiles in the slip flow are flattened compared to the non-slip flow regimes while they are not affected by the nanoparticle concentration. The pressure drop reduces with an increase in the slip velocity. It increases with an increase in nanoparticles volume fraction.

The slip velocity has an increasing effect on the entrance length. The entrance length is not affected by nanoparticle concentration. At a given Reynolds number, the nanoparticle concentration does not have any effect on the Poiseuille number. But the friction factor decreases extremely when the Knudsen number increases.

Increasing nanoparticle volume fraction decreases the bulk temperature. The slip velocity causes to increase temperature at any cross section. Both Kn and ϕ cause the temperature gradient at the wall to increase.

At a given Re, the nanoparticle concentration increases the Nusselt number in both the slip and non-slip flow regimes. The combined effect of slip velocity and jump temperature can increase or decrease heat transfer depending on their relative magnitude. In Microsystems, employing nanofluids with high Pr (high β) and a microchannel with high slip velocity (high Kn) increases heat transfer and therefore has great advantages.

Chapter 8

Summary and Future Works

In this chapter, the most important results and conclusions are summarized. Based on the results, indications for future work are given.

8.1 Summary

With the development of science and technology, microsystems implementations in all kind of technology have been raised numerously. Although microsystems are used widely in the technology, but there is not a complete knowledge about components behaviors. One of the most important microsystems is the microfluidic system, which requires further investigation.

This work focuses on liquid or gas slip flow in Microfluidic systems. A large microfluidic system can be separated into straight and curved microchannels. After investigation of the straight and curved microchannels, results are interpreted for the complete microfluidic system. Usually the Knudsen number is less than 0.1. In this case, the Navier-Stokes equations including slip velocity and jump temperature boundary conditions can be used.

Effects of rarefaction on forced convection heat transfer of laminar, steady and incompressible fluid flows in straight and curved microchannels are investigated. The Navier-Stokes and energy equations are discretized using the

Finite Volume technique and SIMPLER algorithm. The numerical simulation results are as follows:

The results show that the velocity distribution in the slip flow regimes is flattened compared to the non-slip flow regimes. Increasing the Knudsen number decreases the maximum flow velocity while the flow velocity near to the wall increases. Pressure reduces with an increase in the slip velocity. Pressure decreases linearly along the microchannels. The slip velocity has a decreasing effect by more than 50% on the pressure drop for the case of Kn=0.1. The Knudsen number has an increasing effect on the entrance length but this effect is more significant at high Re.

The local friction coefficient reduces with an increase in slip velocity. In slip flow, the Poiseuille number and the Nusselt number have finite values at the entrance of channel which can be calculated with $f\,\mathrm{Re} = \frac{2}{Kn}$ and $Nu = \frac{\beta}{Kn}$. The combined effect of the slip velocity and the jump temperature might increase or decrease the Nusselt number based on their relative magnitude. But the increasing effect of slip velocity on heat transfer is dominant for low jump temperature (high value of β). The decreasing effect of jump temperature on heat transfer is more dominant for the high slip velocity values.

Based on the results of the numerical calculations, it is shown that analytical solutions can be employed to calculate fluid flow in large microfluidic systems, when the Reynolds number is less than 100. A significant agreement between the calculated analytical results and numerical calculation results are observed.

Heat transfer enhancement is very important and essential in cooling application of microfluidic systems. Therefore, thermal and hydraulic behaviors of nanofluid flow in microchannels with considering the slip velocity and the jump temperature conditions are simulated and discussed. Forced convection nanofluid flow in microchannels is simulated to study effects of rarefaction and Al_2O_3 nanoparticles concentration on the slip flow regimes. The Brownian motions of nanoparticles are considered to determine the thermal conductivity of nanofluids.

It is presented that the non-dimensional velocity profiles in the Nanofluid slip flow are flattened compared to the non-slip flow regimes. Flow velocity is not

affected by the nanoparticle concentration. The pressure drop decreases with an increase in the slip velocity while it increases with increasing nanoparticles volume fraction.

The slip velocity has an increasing effect on the entrance length. The entrance length is not affected by nanoparticles concentration. At a given Reynolds number, the nanoparticles concentration does not have any effect on the Poiseuille number. But the Poiseuille number reduces extremely with the increase of the Knudsen number.

Increasing nanoparticle volume fraction decreases the flow temperature. But the slip velocity increases the temperature at any cross section. Both the Knudsen number and the nanoparticles concentration result in an increase of the temperature gradient at the wall. The nanoparticles concentration increases the Nusselt number in both the slip and non-slip flow regimes. The combined effect of the slip velocity and the jump temperature might increase or decrease heat transfer depending on their relative magnitude. Employing nanofluids with the high Prandtl number (high β) and a microchannel with high slip velocity (high Knudsen number) increases heat transfer and has great advantages.

8.2 Future Works

Although microfluidic systems are investigated in this work, there are still many aspects in this field that might be studied further.

At first, due to the lack of experimental work in this field, we had to use some assumption, which might be neglected for further works. The fluid flow might be considered as a compressible flow, which is important for gas flow. The unsteady fluid flow in microchannels should be studied. The surface roughness can be considered. The flow properties are assumed constant in this work, which might be considered variable with some flow characters such as temperature and pressure.

References

[ABB06] Abbassi, H. and Aghanajafi, C., 2006. Evaluation of heat transfer augmentation in a nanofluid-cooled microchannel heat sink. Journal of Fusion Energy. 25 (3-4), 187-196.

[AKB08] Akbarinia, A., 2008. Impacts of nanofluid flow on skin friction factor and Nusselt number in curved tubes with constant mass flow. Int. J. Heat Fluid Flow. 29 (1), 229-241.

[AKB11A] Akbarinia, A., Abdolzadeh, M., Laur, R., 2011. Critical investigation of heat transfer enhancement using nanofluids in microchannels with slip and non-slip flow regimes. Applied Thermal Engineering. 31, 556-565.

[AKB10A] Akbarinia, A., G. Amirian, Laur, R., 2010. Uncertainly in heat transfer enhancement with nanofluids slip flow in microchannels. 3th International Congress on Nanoscience and Nanotechnology, November 9-11, Shiraz, Iran

[AKB07] Akbarinia, A. and Behzadmehr, A., 2007. Numerical study of laminar mixed convection of a nanofluid in horizontal curved tubes. Applied Thermal Eng. 27 (8-9), 1327-1337.

[AKB09] Akbarinia, A. and Laur, R., 2009. Investigation the diameter of solid particles effects on a laminar nanofluid flow in a curved tube using a two phase approach. Int. J. Heat fluid flow. 30 (4), 706-714.

[AKB10B] Akbarinia, A., Laur, R., 2010. Two dimensional forced convection nanofluids flow in microchannel using slip velocity and jump boundary conditions. 28th UIT Heat Transfer Congress (UIT 2010), June 21 -23, ISBN: 978-88-89252-14-7, Pages 281-286, Brescia, Italy.

[AKB09A] Akbarinia, A., Laur, R., Bunse-Gerstner, A., 2009. Developing of laminar fluid flow in rectangular microchannels. 2nd WSEAS International Conference on Engineering Mechanics, Structures and Engineering Geology (EMESEG '09), July 22-24, 2009, ISSN: 1790-2769, Pages 126-132, Rodos Island, Greece

[AKB09B] Akbarinia, A., Laur, R., Bunse-Gerstner, A., 2009. Thermal developing and heat transfer in a forced convection laminar fluid flow in a rectangular microchannel. International Conference on Fluid and Thermal Energy Conversion (FTEC 2009), December 7-10, 2009, ISSN: 1976-278X, Pages 245-255, Tongyeong, South Korea

[AKB10C] Akbarinia, A., Laur, R., Bunse-Gerstner, A., 2010. Prediction of slip flow and heat transfer in a two dimensional rectangular micro/nanochannel with uniform heat flux. 8th Euromech Fluid Mechanics Conference, September 13-16, Technische Universität München, Bad Reichenhall, Germany

[AKB10D] Akbarinia, A., Laur, R., Bunse-Gerstner, A., 2010. Modeling of laminar fluid flows in two-dimensional curved rectangular microchannels with slip velocity boundary condition. 2th European Conference on Microfluidics (μFlu'10), December 8-10, Toulouse, France.

[AKB11B] Akbarinia, A., Shariat, M., Laur, R., 2011. Laminar mixed convection nanofluids flow in elliptic ducts using two phase approach. 8th ASME-JSME Thermal Engineering Joint Conference (AJTEC2011). March 13-17, Honolulu, Hawaii, USA

[ALB06] Al-Bakhit, H., Fakheri, A., 2006. Numerical simulation of heat transfer in simultaneously developing flows in parallel rectangular ducts. Applied Thermal Engineering. 26, 596–603.

[ALF05] Alfadhel, K. A. and Kothare, M. V., 2005. Microfluidic modeling and simulation of flowin membrane microreactors. Chemical Engineering Science. 60, 2911 – 2926.

[AVC08] Avci, M., Aydin, O., 2008. Laminar forced convection slip-flow in a micro-annulus between two concentric cylinders. Int. J. Heat Mass Transfer. 51, 3460–3467.

[BAR07] Barkhordari, M., Etemad, S.Gh., 2007. Numerical study of slip flow heat transfer of non-Newtonian fluids in circular microchannels. Int. J. Heat Fluid Flow. 28, 1027–1033.

[BAR99] Barrat, J.L., Bocquet, L., 1999. Large slip effect at a nonwetting fluid-solid interface. Phys. Rev. Lett. 82 (23), 4671-4674.

[BAR97] Barron, R.F., Wang, X., Ameel, T.A., Warrington, R.O., 1997. The Graetz problem extended to slip-flow. Int. J. Heat Mass Transfer. 40 (8), 1817–1823.

[BEH06] Behzadmehr, A., Akbarinia, A., 2006. Nanofluid mixed convection in a curved tube. 13th International Heat Transfer Conference, IHTC-13, August 13-18, Sydney, Australia

[BES94] Beskok, A., Karniadakis, G.E., 1994. Simulation of heat and momentum transfer in complex micro-geometries. J. Thermophys. Heat Transfer. 8 (4), 355-370.

[BES96] Beskok, A., Karniadakis, G. E. and Trimmer, W., 1996. Rarefaction and compressibility effects in gas microflows. Transactions of the ASME. Vol. 118 (3), 448 (9 pages).

[BIS07] Biswal, L., Som, S.K., Chakraborty, S., 2007. Effects of entrance region transport processes on free convection slip flow in vertical microchannels with isothermally heated walls. Int. J. Heat Mass Transf. 50 (7–8), 1248–1254.

[CHE10] Che, Z., Wong, T. N., and Nguyen, N. T., 2010. An analytical model for a liquid plug moving in curved microchannels. International Journal of Heat and Mass Transfer. 53, 1977–1985.

[CHE05] Chein, R. and Huang, G., 2005. Analysis of microchannel heat sink performance using nanofluids. Applied Thermal Engineering. 25 (17-18), 3104-3114.

[CHE07] Chein, R. and Chuang, J., 2007. Experimental microchannel heat sink performance studies using nanofluids. International Journal of Thermal Sciences. 46 (1), 57-66.

[CHO03] Choi, H., Lee, D. and Maeng, J.-S., 2003.Computation of slip flow in microchannels using Langmuir slip condition. Numerical Heat Transfer Part A. 44, 59–71.

[CHO05] Chon, C.H., Kihm, K.D., Lee, S.P. and . Choi, S.U.S, 2005. Empirical correlation finding the role of temperature and particle size for nanofluid (Al_2O_3) thermal conductivity enhancement. Appl. Phys. Lett. 87, 1–3.

[DON07] Dongari, N., Agrawal, A. and Agrawal, A., 2007. Analytical solution of gaseous slip flow in long microchannels. International Journal of Heat and Mass Transfer. 50, 3411–3421.

[DUA07] Duan, Z.P., Muzychka, Y.S., 2007. Slip flow in elliptic microchannels. Int. J. Therm. Sci. 46, 1104–1111.

[ELG09] El-Genk, M. S. and Yang, I.-H., 2009. Numerical analysis of laminar flow in micro-tubes with a slip boundary. Energy Conversion and Management. 50, 1481–1490.

[FED00] Fedorov, A. G. and Viskanta, R., 2000. Three-dimensional conjugate heat transfer in the microchannel heat sink for electronic packaging. International Journal of Heat and Mass Transfer. 43, 399-415.

[GAD99] Gad-el-Hak, M., 1999. The fluid mechanics of microdevices: The Freeman Scholar Lecture. J. Fluids Eng. 121, 5–33.

[GAD06] Gad-el-Hak, Mohamed, 2006. The MEMS Handbook, MEMS: Introduction and Fundamentals. Second Edition. Taylor & Francis Group.

[GJE97] Gjesdal, T. and Lossius, M.E.H., 1997. Comparison of pressure correction smoothers for multigrid solution of incompressible flow. Int. J. Numer. Methods Fluids. 25, 393-405.

[HAR99] Harms, T. M., Kazmierczak, M. J. and Gerner, F. M., 1999. Developing convective heat transfer in deep rectangular microchannels. International Journal of Heat and Fluid Flow. 20, 149-157.

[HET08] Hettiarachchi, H.D. M., Golubovic, M., Worek, W. M. and Minkowycz, W.J., 2008. Three-dimensional laminar slip-flow and heat transfer in a rectangular microchannel with constant wall temperature. Int. J. Heat Mass Transf. 51, 5088–5096.

[HO10] Ho, C.J., Wei, L.C. and Li, Z.W., 2010. An experimental investigation of forced convective cooling performance of a microchannel heat sink with Al_2O_3-water nanofluid. Applied Thermal Engineering. 30 (2-3), 96-103.

[HO98] Ho,C.-M. and Tai, Y.-C., 1998. Micro-electro-mechanical systems (MEMS) and fluid flow. Annu. Rev. Fluid Mech. 30, 579–612.

[HOL03] Holden, M. A., Kumar, S., Castellana, E. T., Beskok, A. and Cremer, P. S., 2003. Generating fixed concentration arrays in a microfluidic device. Sensors and Actuators B. 92, 199–207.

[HRN07] Hrnjak, P. and Tu, X., 2007. Single phase pressure drop in microchannels. International Journal of Heat and Fluid Flow. 28, 2–14.

[HU07] Hu, G. and Li, D., 2007. Multiscale phenomena in microfluidics and nanofluidics. Chemical Engineering Science. 62, 3443 – 3454.

[HUS08] Husain, A. and Kim, K.-Y., 2008. Optimization of a microchannel heat sink with temperature dependent fluid properties. Applied Thermal Engineering. 28. 1101–1107.

[ISS85] Issa, R.I., 1985. Solution of implicitly discretized fluid flow equation by operator-splitting. J. Comput. Physics. 62, 40-65.

[JAN06] Jang, S.P. and Choi, S.U.S., 2006. Cooling performance of a microchannel heat sink with nanofluids. Applied Thermal Engineering. 26 (17-18), 2457-2463.

[JUD02] Judy, J., Maynes, D. and Webb, B.W., 2002. Characterization of frictional pressure drop for liquid flows through microchannels. International Journal of Heat and Mass Transfer. 45, 3477–3489.

[JUN09] Jung, J.Y., Oh, H.S. and Kwak, H.Y., 2009. Forced convective heat transfer of nanofluids in microchannels. International Journal of Heat and Mass Transfer. 52 (1-2), 466-472.

[KHA09] Khadem, M.H., Shams, M., Hossainpour, S., 2009. Numerical simulation of roughness effects on flow and heat transfer in microchannels at slip flow regime. Int Communications in Heat and Mass Transfer. 36, 69–77.

[KOO05] Koo, J. and Kleinstreuer, C., 2005. Laminar nanofluid flow in microheat-sinks, International Journal of Heat and Mass Transfer. 48 (13), 2652-2661.

[KRA09] Kraly, J. R., Holcomb, R. E., Guan, Q. and Henry, C. S., 2009. Review: Microfluidic applications in metabolomics and metabolic profiling. Analytica Chimica Acta. 653, 23–35.

[LAR00] Larrodé, F.E., Housiadas, C., Drossinos, Y., 2000. Slip-flow heat transfer in circular tubes. Int. J. Heat Mass Transf. 43, 2669–2680.

[LEE06] Lee, P., Garimella, S. V., 2006. Thermally developing flow and heat transfer in rectangular microchannels of different aspect ratios. Int. J. Heat Mass Transfer. 49, 3060–3067.

[LI08] Li, J. and Kleinstreuer, C., 2008. Thermal performance of nanofluid flow in microchannels. Int. Journal of Heat and Fluid Flow. 29 (4), 1221-1232.

[LI06] Li, H. and Olsen, M. G., 2006. MicroPIV measurements of turbulent flow in square microchannels with hydraulic diameters from 200 μm to 640 μm. International Journal of Heat and Fluid Flow. 27, 123–134.

[MAI04] Maiga, S.E.B., Nguyen, C.T., Galanis, N. and Roy, G., 2004. Heat transfer behaviors of nanofluids in a uniformly heated tube. Superlatt. Microstruct**. 35**, pp. 543–557.

[MAL99] Mala, Gh. M. and Li, D., 1999. Flow characteristics of water in microtubes. International Journal of Heat and Fluid Flow. 20, 142-148.

[MOK11] Mokhtari Moghari, R., Akbarinia, A., Shariat, M., Talebi, F., Laur, R., 2011. Two phase mixed convection Al_2O_3-Water nanofluid flow in an annulus. International Journal of Multiphase Flow. 37 (6), 585-595.

[MOR04] Morini, G. L., 2004. Single-phase convective heat transfer in microchannels: a review of experimental results. International Journal of Thermal Sciences. 43, 631–651.

[MUR08] Murshed, S.M.S., Leong , K.C. and Yang, C., 2008. Thermophysical and electrokinetic properties of nanofluids – A critical review. Applied Thermal Engineering, 28, 2109–2125.

[NGO07] Ngoma, G. D. and Erchiqui, F., 2007. Heat flux and slip effects on liquid flow in a microchannel. International Journal of Thermal Sciences. 46, 1076–1083.

[NIA08] Niazmand, H., Renksizbulut, M. and Saeedi, E., 2008. Developing slip-flow and heat transfer in trapezoidal microchannels. International Journal of Heat and Mass Transfer. 51(25-26), 6126-6135.

[PAK98] Pak, B.C. and Cho, Y.I., 1998. Hydrodynamic and heat transfer study of dispersed fluids with submicron metallic oxide particles. Exp. Heat Transfer. 11, pp. 151–170.

[PAT72] Patankar, S.V. and Spalding, D.B., 1972. A calculation procedure for heat mass and momentum transfer in three dimensional parabolic flows. Int. J. Heat Mass Transfer. 15, p. 1787.

[PAT80] Patankar, S. V., 1980. Numerical heat transfer and fluid flow. McGraw Hill, New York,USA.

[RAI88] Raithby, G.D. and Schneider, G.E., 1988. Elliptic system: finite difference method II. in Minkowycz, W.J., Sparrow, E.M., Pletcher, R.H. and Schneider, G.E. (Eds), Handbook of Numerical Heat Transfer, Wiley, New York, NY, pp. 241-89.

[RED01] Reddy B.D., and Mitchell G.P., 2001. Finite element analysis of fibre suspension flows. Computer Methods in Applied Mechanics and Engineering. 190, 2349-2367.

[REN06] Renksizbulut, M., Niazmand, H., Tercan, G., 2006. Slip-flow and heat transfer in rectangular microchannels with constant wall temperature. Int. J. Therm. Sci. 45 (9), 870–881.

[REY83] Reynolds, Osborne,1883. An experimental investigation of the circumstances which determine whether the motion of water shall be direct or sinuous, and of the law of resistance in parallel channels, Philosophical Transactions of the Royal Society, 174, 935–982.

[ROS09] Rosa, P., Karayiannis, T.G. and Collins, M.W., 2009. Single-phase heat transfer in microchannels: The importance of scaling effects. Applied Thermal Engineering. 29, 3447–3468.

[SCH58] Schaaf, S. A., and Chambre, P. L, 1958. Flow of rarefied gases, in Fundamental of Gasdynamics, Vol. III, H. W. Emmons, ed., Princeton University Press, Princeton, pp. 687-739.

[SEN04] Senn, S.M. and Poulikakos, D., 2004. Laminar mixing, heat transfer and pressure drop in tree-like microchannel nets and their application for thermal management in polymer electrolyte fuel cells. Journal of Power Sources. 130, 178–191.

[SHA09] Shao, N., Gavriilidis, A. and Angeli, P., 2009. Flow regimes for adiabatic gas–liquid flow in microchannels. Chemical Engineering Science. 64, 2749- 2761.

[SHA11] Shariat, Mohammad, Akbarinia, Alireza, Hossein Nezhad, Alireza, Laur, Rainer, 2011. Numerical study of two phase laminar mixed convection nanofluid in elliptic ducts. Applied Thermal Engineering. 31 (14-15), 2348-2359.

[SIL08] Silva, G., Leal, N. and Semiao, V., 2008. Micro-PIV and CFD characterization of flows in a microchannel: Velocity profiles, surface roughness and Poiseuille numbers. International Journal of Heat and Fluid Flow. 29, 1211–1220.

[SQU05] Squires,T. M. and Quake, S. R., 2005. Microfluidics: Fluid physics at the nanoliter scale. Reviews of modern Physics. 77(3), 977–1026

[STE06] Steinke, M. E. and Kandlikar, S. G., 2006. Single-phase liquid friction factors in microchannels. International Journal of Thermal Sciences. 45, 1073–1083

[STO04] Stone, H.A., Stroock, A.D. and Ajdari, A., 2004. Engineering flows in small devices: Microfluidics Toward a Lab-on-a-Chip. Annu. Rev. Fluid Mech. 36, 381–411.

[STO51] Stokes, George, 1851. On the Effect of the Internal Friction of Fluids on the Motion of Pendulums, Transactions of the Cambridge Philosophical Society, 9, 8–106.

[STR73] Strang, G. and George, F., 1973. An analysis of the finite element method, Englewood Cliffs:Prentice-Hall.

[SUN07] Sun, W., Kakac, S., Yazicioglu, A.G., 2007. A numerical study of single-phase convective heat transfer in microtubes for slip flow. Int. J. Therm. Sci. 46, 1084–1094.

[TRE02] Tretheway, D.C., Meinhart, C. D., 2002. Apparent fluid slip at hydrophobic microchannel walls. Phys. Fluids. 14 (3), L9- L12.

[TSA07] Tsai, T.H. and Chein, R., 2007. Performance analysis of nanofluid-cooled microchannel heat sinks. International Journal of Heat and Fluid Flow. 28 (5), 1013-1026.

[TUC81] Tuckerman D.B., Pease F.W., 1981. High-performance heat sinking for VLSI. IEEE Electron Device Lett. EDL-2, 126-129.

[TUN02] Tunc, G. and Bayazitoglu, Y., 2002. Heat transfer in rectangular microchannels. International Journal of Heat and Mass Transfer. 45, 765-773.

[VAN84] van Doormaal, J.P. and Raithby, G.D., 1984. Enhancement of SIMPLE method for predicting incompressible fluid flows. Numer. Heat Transfer. 7, 147-63.

[VAN85] van Doormaal, J.P. and Raithby, G.D., 1985. An evaluation of the segregated approach for predicting incompressible fluid flow. Paper 85-HT-9, ASME.

[WAN09] Wang, H. and Wang, Y., 2009. Measurement of water flow rate in microchannels based on the microfluidic particle image velocimetry. Measurement. 42, 119–126.

[WEN93] Wen, X. and Ingham, D.B., 1993. A new method for accelerating the rate of convergence of the SIMPLE-like algorithm. Int. J. Numer. Methods in Fluids. 17, 385-400.

[WHI06] White, F. M., 2006. Viscous Fluid Flow (3rd. ed.). New York: McGraw-Hill.

[WU03] Wu, H. Y. and Cheng, P., 2003. Friction factors in smooth trapezoidal silicon microchannels with different aspect ratios. International Journal of Heat and Mass Transfer. 46, 2519–2525.

[XIA09] Xiao, N., Elsnab, J. and Ameel, T., 2009. Microtube gas flows with second-order slip flow and temperature jump boundary conditions. International Journal of Thermal Sciences. 48, 243–251.

[XU00] Xu B., Ooi K.T., Wong N.T. and Choi W.K., 2000. Experimental investigation of flow friction for liquid flow in microchannels. Int. Comm. Heat Mass Transfer. Vol. 27(8), 1165-1176.

[XUA03] Xuan, Y.M. and Li, Q., 2003. Investigation on convective heat transfer and flow features of nanofluids. J. Heat Transfer. 125, pp. 151–155.

[YAN03] Yang, J., Kwok, D.Y., 2003. Effect of liquid slip in electrokinetics parallel plate microchannel flow. J. Colloid Interface Sci. 260, 225-233.

[YU01A] Yu, S. and Ameel, T. A., 2001. A universal entrance Nusselt number for internal slip flow. Int. Comm. Heat Mass Transfer. 28(7), 905-910.

[YU01B] Yu, S. and Ameel, T.A., 2001. Slip flow heat transfer in rectangular microchannels. Int. J. Heat Mass Transf. 44, 4225–4234.

[ZHU06] Zhu, X., Liao, Q., 2006. Heat transfer for laminar slip flow in a microchannel of arbitrary cross section with complex thermal boundary conditions. Applied Thermal Engineering. 26, 1246–1256.

Appendix A

Dimensionless Numbers

The Reynolds number

The Reynolds number (Re) is widely used in fluid flow and heat transfer. The Reynolds number is very important parameter in fluid mechanics. The Reynolds number is used to distinguish between different flow regimes such as laminar flow, transient flow and turbulence flow. It is defined as the ratio of inertial forces to viscous forces. The concept was introduced by George Gabriel Stokes [STO51] in 1851, but the Reynolds number is named after Osborne Reynolds [REY83], who popularized its use in 1883.

The Reynolds number is given as:

$$Re = \frac{\rho v\, D_h}{\mu},$$

where ρ, v, D_h, μ are density, mean flow velocity, hydraulic diameter and dynamic viscosity, respectively.

The Knudsen number

The Knudsen number (Kn) is used to distinguish between statistical flow or continuum flow. It is defined as the ratio of the molecular mean free path length

to a representative physical length scale. The number is named after Danish physicist Martin Knudsen (1871–1949).

The Knudsen number is given as:

$$Kn = \frac{\lambda}{D_h},$$

where λ is mean free path of gas molecular.

The Prandtl number

The Prandtl number (Pr) is the ratio of momentum diffusivity (kinematic viscosity) to thermal diffusivity. It is named after the German physicist Ludwig Prandtl [WHI06].

It is defined as:

$$Pr = \frac{\vartheta}{\alpha} = \frac{\mu C_p}{\lambda},$$

where υ, α and μ are kinematic viscosity, thermal diffusivity and dynamic viscosity, respectively. C_p and λ are specific heat and thermal conductivity.

The Peclet number

The Péclet number (Pe) is used in the study of transport phenomena in fluid flows. It is defined as the ratio of the rate of advection of a physical quantity by the flow to the rate of diffusion of the same quantity driven by an appropriate gradient. It is named after the French physicist Jean Claude Eugène Péclet [PAT80]. The Peclet number is equivalent to the product of the Reynolds number and the Prandtl number. The Peclet number shows the importance of convection in comparison with thermal conduction. When the Peclet number is smaller than one, the axial thermal conduction should be considered.

The Peclet number is defined as:

$$Pe = \frac{\rho\, \bar{u}\, C_p\, D_h}{\lambda} = Re\,\mathrm{Pr}\ ,$$

where $\bar{u}$ is average velocity.

The Nusselt number

The Nusselt number (Nu) is the ratio of convective to conductive heat transfer across (normal to) the boundary. It is named after Wilhelm Nusselt [WHI06]. A small Nusselt number around 3 and 4, namely convection and conduction of similar magnitude, is characteristic of laminar flow. A larger Nusselt number corresponds to more active convection, with turbulent flow typically more than 85.

The Nusselt number is defined as:

$$Nu = \frac{h\, D_h}{\lambda},$$

where h is heat transfer coefficient.

The Poiseuille number

The Poiseuille number (*f*Re) is a product of the friction factor (*f*) and the Reynolds number (Re).

Appendix B

Thermal and momentum accommodation coefficients

Gases exhibit non-continuum effects when the characteristic length scale of the system becomes comparable to the gas mean free path λ, defined as the average distance traveled by a molecule between collisions.

The definition of mean free path is given as follows:

$$\lambda = \frac{2\mu}{\rho\bar{c}} \tag{B1}$$

where μ and ρ are the gas viscosity and mass density, $\bar{c} = \left(\frac{8k_BT}{\pi m}\right)^{1/2}$ is the mean molecular speed, k_B is the Boltzmann constant, T is the local gas temperature, and m is the gas molecular mass.

Non-continuum effects become important either when system length scales become microscopically small or when gas pressures become low. The rise of non-continuum behaviour with decreasing pressure results from the inverse dependence of the mean free path on gas density, as given in (B1).

Rarefied gas flow is also observed in low-speed, low-pressure systems, such as semiconductor and MEMS manufacturing. One possibility for achieving high accommodation is to manufacture a surface with a high degree of microscopic roughness and/or porosity.

In rarefied gas dynamics, one of the major problems is to model the interaction of gas molecules with a solid surface. The parameter accounting for this phenomenon is the accommodation coefficient that represents the tendency of gas to accommodate the wall state or the Thermal Accommodation Coefficient (σ_T or α) is parameter which quantify the efficiency of thermal energy transfer across an interface. It can be given as follows:

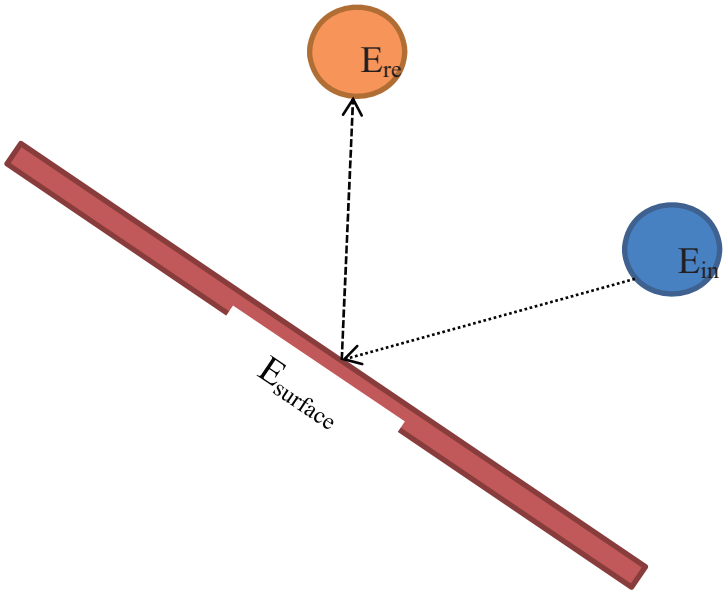

Fig. B1. Thermal accommodation coefficient

$$\alpha = \frac{E_{reflected} - E_{in}}{E_{surface} - E_{in}} \tag{B2}$$

or

$$\alpha = \frac{T_{reflected} - T_{bulk}}{T_{surface} - T_{bulk}} \tag{B3}$$

where E_{in} (T_{bulk}) denotes the energy flux (temperature) of the incident molecular stream, $E_{reflected}$ ($T_{reflected}$) denotes the energy (temperature) carried away by the reflected molecules, and $E_{surface}$ ($T_{surface}$) denotes the energy (temperature) that is carried away by the reflected molecules when the temperature of reflected molecular stream is assumed to be the same as the wall temperature $T_{surface}$, as shown in Fig. B1 [SCH58].

Physically, there exist two extreme conditions for the molecular reflection at wall. The first one is the perfectly specular reflection, in which the molecules elastically collide with wall so that the molecular velocity component normal to

the surface is reversed while that parallel to the surface remains unchanged. As a result, the impinging molecular stream exerts no shear stress on the surface except the normal direction to the wall. In this case, it becomes $E_{reflected}=E_{in}$ ($T_{reflected} = T_{bulk}$) so that α becomes zero. The other condition is the perfectly diffusive reflection, in which the incident molecules have their mean energy completely adjusted or ‘‘accommodated’’ to the surface for which it becomes $E_{reflected} = E_{surface}$ ($T_{reflected} = T_{surface}$) so that α is equal to unity.

Tangential Momentum accommodation coefficient σ_v (TMAC) is the fraction of the momentum normal to the wall that is transferred to the wall in terms of stress. This stress is more commonly known as pressure. By creating a pressure on the wall some of the vertical momentum is lost. If the particle had a perfect reflection and all of the normal momentum was maintained then that would be a TMAC of 0. If the particle lost all of its normal momentum that would be an TMAC of 1.

The surface roughness, weight of the particle, gas properties, solid surface material temperature, pressure and oxidation of the wall are big factors when determining the accommodation coefficients.

Appendix C

List of Publications

[1] A. Akbarinia, M. Abdolzadeh, R. Laur, “Critical Investigation of Heat Transfer Enhancement Using Nanofluids in Microchannels with Slip and Non-Slip Flow Regimes”, Applied Thermal Engineering, Volume 31, 2011, Pages 556-565

[2] R. Mokhtari Moghari, A. Akbarinia, M. Shariat, F. Talebi, R. Laur, “Two phase mixed convection Al_2O_3-Water nanofluid flow in an annulus” International Journal of Multiphase Flow, Volume 37, Issue 6, 2011, Pages 585-595

[3] Mohammad Shariat, Alireza Akbarinia, Alireza Hossein Nezhad, Rainer Laur, “Numerical study of two phase laminar mixed convection nanofluid in elliptic ducts”, Applied Thermal Engineering, Volume 31, Issues 14–15, 2011, Pages 2348-2359

[4] A. Akbarinia, R. Laur, "Investigation the Diameter of solid Particles effects on a Laminar Nanofluid Flow in a Curved Tube Using a Two Phase Approach", International Journal of Heat and fluid flow, Volume 30, Issue 4, 2009, Pages 706-714

[5] A. Akbarinia, M. Shariat, R. Laur, “Laminar mixed convection nanofluids flow in elliptic ducts using two phase approach”, Oral presentation at the

8th ASME-JSME Thermal Engineering Joint Conference(AJTEC2011), March 13-17, 2011, Honolulu, Hawaii, USA

[6] A. Akbarinia, R. Laur, A. Bunse-Gerstner, "Modeling of Laminar Fluid Flows in Two-dimensional Curved Rectangular Microchannels with Slip Velocity Boundary Condition", Oral presentation at 2th European Conference on Microfluidics (μFlu'10), December 8-10, 2010, Toulouse, France

[7] A. Akbarinia, G. Amirian, R. Laur, "Uncertainly in heat transfer enhancement with nanofluids slip flow in microchannels", Poster Presentation at 3th International Congress on Nanoscience and Nanotechnology, November 9-11, 2010, Shiraz, Iran

[8] A. Akbarinia, R. Laur, A. Bunse-Gerstner, "Prediction of slip flow and heat transfer in a two dimensional rectangular micro/nanochannel with uniform heat flux" Contributed talk at 8th Euromech Fluid Mechanics Conference, September 13-16, 2010, Technische Universität München, Bad Reichenhall, Germany

[9] A. Akbarinia, R. Laur, A. Bunse-Gerstner, "Uncertainty in heat transfer of nanofluids flow in microchannels with slip and non-slip flow regimes", Contributed talk at Engineering Conferences International, Nanofluids: Fundamentals and Applications II, August 15-19, 2010, Montreal, Canada

[10] A. Akbarinia, R. Laur, "Two dimensional forced convection nanofluids flow in microchannel using slip velocity and jump boundary conditions", Oral presentation at 28th UIT Heat Transfer Congress (UIT 2010), June 21 - 23, 2010, ISBN: 978-88-89252-14-7, Pages 281-286, Brescia, Italy

[11] G. Amirian, A. Akbarinia, "Heat transfer analysis in the welding process with moving heat source", Oral presentation at 18th Annual International Conference on Mechanical Engineering, (ISME2010), May 11-13, 2010, Tehran, Iran

[12] A. Akbarinia, R. Laur, A. Bunse-Gerstner, "Thermal developing and heat transfer in a forced convection laminar fluid flow in a rectangular microchannel", Oral presentation at International Conference on Fluid and

Thermal Energy Conversion (FTEC 2009), December 7-10, 2009, ISSN: 1976-278X, Pages 245-255, Tongyeong, South Korea

[13] A. Akbarinia, R. Laur, A. Bunse-Gerstner, "Developing of laminar fluid flow in rectangular microchannels", Oral presentation at 2nd WSEAS International Conference on Engineering Mechanics, Structures and Engineering Geology (EMESEG '09), July 22-24, 2009, ISSN: 1790-2769, Pages 126-132, Rodos Island, Greece